ATOMIC LEVEL THEORY OF THE GROWTH OF CRYSTALLINE OXIDE MATERIALS

A Dissertation

Presented to the Faculty of the Graduate School

of Cornell University

in Partial Fulfillment of the Requirements for the Degree of

Doctor of Philosophy

by

Daniel Ari Freedman

January 2009

ATOMIC LEVEL THEORY OF THE

GROWTH OF CRYSTALLINE OXIDE MATERIALS

Daniel Ari Freedman, Ph.D.

Cornell University 2009

This dissertation investigates a continuum of important processes — deposition of materials, formation of point vacancies, and creation of planar defects — in representative ceramic oxide compounds.

We begin with an investigation of cluster assimilation and collisional filtering on metal-oxide surfaces and present the first *ab initio* molecular dynamics study of collisions between metal-oxide clusters and surfaces. The resulting trajectories reveal that internal degrees of freedom of the cluster play a defining role in collision outcome. The phase space of incoming internal temperature and translational energy exhibits regions where the collision process itself ensures that clusters which do not rebound from the surface assimilate seamlessly onto it upon impact. This filtering may explain some aspects of recent observations of a "fast smoothing mechanism" during pulsed laser deposition.

We then present a study of the local strain effects associated with vacancy defects in strontium titanate and report the first calculations of elastic dipole tensors and chemical strains for point defects in perovskites. The combination of local and long-range results will enable determination of x-ray scattering signatures that can be compared with experiment. We find that the oxygen vacancy possesses a special property — a highly anisotropic elastic dipole tensor which almost vanishes upon averaging over all possible defect orientations. Moreover, through direct comparison with experimental measurements of chemical strain, we place constraints

on the possible defects present in oxygen-poor strontium titanate and introduce a conjecture regarding the nature of the predominant defect in strontium-poor stoichiometries.

Finally, we present the most detailed and extensive theoretical study to date of the structural configurations of Ruddlesden–Popper (RP) phases in antiferrodistortive (AFD) perovskites and formulate a program of study which can be pursued for RP phases of any AFD perovskite system. We systematically investigate the effects of oxygen octahedral rotations on the energies of RP phases in AFD perovskites ($A_{n+1}B_nO_{3n+1}$) for $n = 1 \ldots 30$, providing asymptotic results for $n \to \infty$ that give both the form of the interaction between stacking faults and the behavior of such stacking faults in isolation. We find an inverse-distance interaction between faults with a strength which varies by as much as a factor of two depending on the configuration of the octahedra. We find that the strength of this effect can be sufficient to (a) stabilize or destabilize the RP phase with respect to dissociation into the bulk perovskite and the bulk A-oxide and (b) affect the energy scales of the RP phase sufficiently to constrain the rotational states of the octahedra neighboring the stacking faults, even at temperatures where the octahedra in the bulk regions librate freely. Finally, we present evidence that the importance of the octahedral rotations can be understood in terms of changes in the distances between oxygen ions on opposing sides of the RP stacking faults.

BIOGRAPHICAL SKETCH

For much of my life, I aspired to combine research in physics with an academic study of philosophy. While my progression in the former discipline has always been relatively linear, if not monotonic, my pursuit of the latter was less clear. This dissertation represents both the journey and the culmination of my doctoral work in physics, almost a decade of my life — years spent acquiring (and, oh too often, misplacing) knowledge, assembling skills, cultivating intuition, and refining inquisitorial tendencies. My time here at Cornell University followed unique educational opportunities available to me as an undergraduate at MIT. Before that even, I benefited from the attention and studious nature of a wonderful family and a public school system in Northeastern Pennsylvania that allowed students to achieve appropriate success, as compelled by hard work. Along the way, sometime recently even, I discovered that my study of philosophy need not be confined to the granite walls and manicured quadrangles of a university, nor even to the metaphorical constraints of its adopted pedagogy. Rudyard Kipling wrote:

> Body and spirit I surrendered whole
> To hard instructors — and received a soul.

And, whatever philosophical considerations or expositions I may now decree as individually "me," have been similarly intertwined with the external clamor of far-flung arenas. My lessons were learned from a most memorable year as an enlisted airborne infantryman on a US Army long range surveillance team in Baghdad, Iraq. My educators were my fellow grunts, and our conversations, though at times droll, could inspire transcendence. Though my return to Cornell and resumption of my doctoral program at first proved disconcerting and unnerving, now and forevermore, I shall thus be able to temper the logic of the scientific discipline with the philosophical consciousness of an individual who managed to experience

an entirely separate life. For that, and for many more reasons, I remain humbly grateful to have been given the privilege to serve my nation. And, in some such introspective moments as these, I muse upon the visions given voice by Tennyson,

> So many worlds, so much to do,
> So little done, such things to be,

and recognize the destiny that we may yet define...

To S.H.Z., with love.

ACKNOWLEDGEMENTS

I am grateful for the individuals with whom I have shared my life thus far. I value the opportunity, through this dissertation, to acknowledge their roles and their importance.

I have known my advisor, Tomás Arias, since I was a freshman at MIT and he a first-year faculty member there, back in 1994–1995, well before my doctoral studies here at Cornell. He challenged all of us students during those years, compelling and energizing and intimidating us to work harder and produce more. Since then, I have been able to observe the manner by which his family life has more recently mellowed his demeanor, though it has not diminished his academic output. I am grateful for his guidance and his experience throughout. He taught me the importance of the scientific story with which I weave and contextualize my research. He instilled in me the necessity of clear and direct communication. He supported and defended the numerous constraints upon my time, and, for a period, on my focus, that my military service entailed. Finally, we shared good conversations on matters, worldly and unremarkable both.

I have benefited from research collaborations with Joel Brock, Aaron Fleet, Darren Dale, David Roundy, David Muller, Lena Fitting Kourkoutis, and JeeHye Lee, as well as support via the DoD National Defense Science and Engineering Graduate Fellowship and the Cornell Center for Materials Research. I have likewise appreciated the friendships and the camaraderie I developed with fellow Cornell graduate students over the past decade: Ivan Daykov, Hande Üstünel, Sahak Petrosyan, John Karcz, David Roundy, Sourish Basu, Grant Meyer, Johannes Lischner, Peijun Zhou, and JeeHye Lee. And my battlefield brothers, especially those closest, though nameless at times, are never far from my mind or my heart.

My greatest gratitude, love, and admiration belong always to my family. Their unfailing support, their constant love, and their sage advice has helped compel me towards this degree, across any difficulties with my research or my motivation. My parents, Nancy and Louis, understood the importance of initial conditions and boundary values — they inculcated morals and ethics within me during my upbringing. My grandparents, Es and Gerald ("Poppy", of blessed memory) and Janice and Saul, lived the lives of the Greatest Generation and impressed upon me the importance of education and community. My brother, Michael, introduced me to the excitement of computer science research and abided the occasional stern countenance of his older brother.

But, above all, my lovely wife, Diana, my soulmate and best friend, shares her life with mine, and for that I am most grateful.

TABLE OF CONTENTS

LIST OF FIGURES

LIST OF TABLES

CHAPTER 1

INTRODUCTION

1.1 Motivation for study of oxides

This dissertation investigates a continuum of important processes — deposition of materials, formation of point vacancies, and creation of planar defects — in representative ceramic oxide compounds. We first study deposition of a relatively simple binary ceramic oxide, magnesium oxide, considering the effect of internal degrees of freedom in the clusters upon their collision with the substrate surface. Next, we examine point defects in a more complex oxide, the canonical perovskite strontium titanate, and discover the predictive power of elastic effects of these vacancies. Finally, we catalogue and investigate the full combinatorial complexity of planar faults in an important class of these oxides, the antiferrodistortive perovskites, drawing both conclusions generic to all members of that class and others confined to certain specific perovskites.

1.1.1 Ceramics

Before we discuss binary oxide and perovskite materials, it is instructive to contextualize the much larger class of ceramic materials. Ceramic materials are not easily categorized nor compartmentalized due to their extended historical impact. They can be classified by various means — chemical composition, mechanical and physical properties, or application and utilization. The most encompassing and widely accepted definition of ceramics was proposed by Kingery in 1960: "nonmetallic, inorganic solids"[1]. The elemental constituents in ceramic compounds are generally

metals or metalloids and nonmetals, with a "mixed" bonding of a combination of covalent, ionic, and sometimes metallic nature[2]. More specifically, ceramics are most frequently oxide, nitride, and carbide compounds; diamond and graphite are also generally considered ceramic (they are literally "inorganic," not composed of living organisms). However, the most applicable classification of these materials is often not by composition or by property, but by bisection into *traditional* ceramics and *advanced* (technical or engineering) ceramics. Traditional ceramics derive from the firing of clays and silicas, while advanced ceramics encompass a much larger variety of compounds that fulfill modern industrial needs. Table 1.1 concisely compares the differences between these traditional and advanced ceramics[2, 3].

1.1.2 Binary oxides

The binary ceramic oxide we study in this work is magnesium oxide, or MgO, which adopts the halite, or rocksalt structure, comprised of two interpenetrating face-centered cubic crystal lattices, as seen in Figure 1.1. Although magnesium oxide is rarely found in pure form in nature, where it is known as the mineral periclase, it is abundant as a constituent in other compounds, such as magnesite ($MgCO_3$) and dolomite ($(Mg,Ca)CO_3$). Magnesium oxide is recognized for its high electrical insulation capability and high thermal conductivity, properties that contribute to its industrial applications in sheathed thermocouples and in resistive heating elements[3].

Table 1.1: Distinctions between traditional and advanced ceramics during successive stages of procurement[2].

Procurement Steps	Advanced Ceramics	Traditional Ceramics
Raw materials preparation	Powder chemistry: Precipitation Spray dry Freeze dry Vapor phase Sol-gel	Raw minerals Clay Silica
Forming	Slip casting Injection molding Sol-gel Hot pressing HIPing Rapid prototyping	Potters wheel Slip casting
High-temperature processing	Electric furnace Hot press Reaction sinter Vapor deposition Plasma spraying Microwave furnace	Flame kiln
Finishing process	Erosion Laser machining Plasma spraying Ion implantation Coating	Erosion Glazing
Characterization	Light microscopy X-ray diffraction Electron microscopy Scanned probe microscopy Neutron diffraction Surface analytical methods	Visible examination Light microscopy

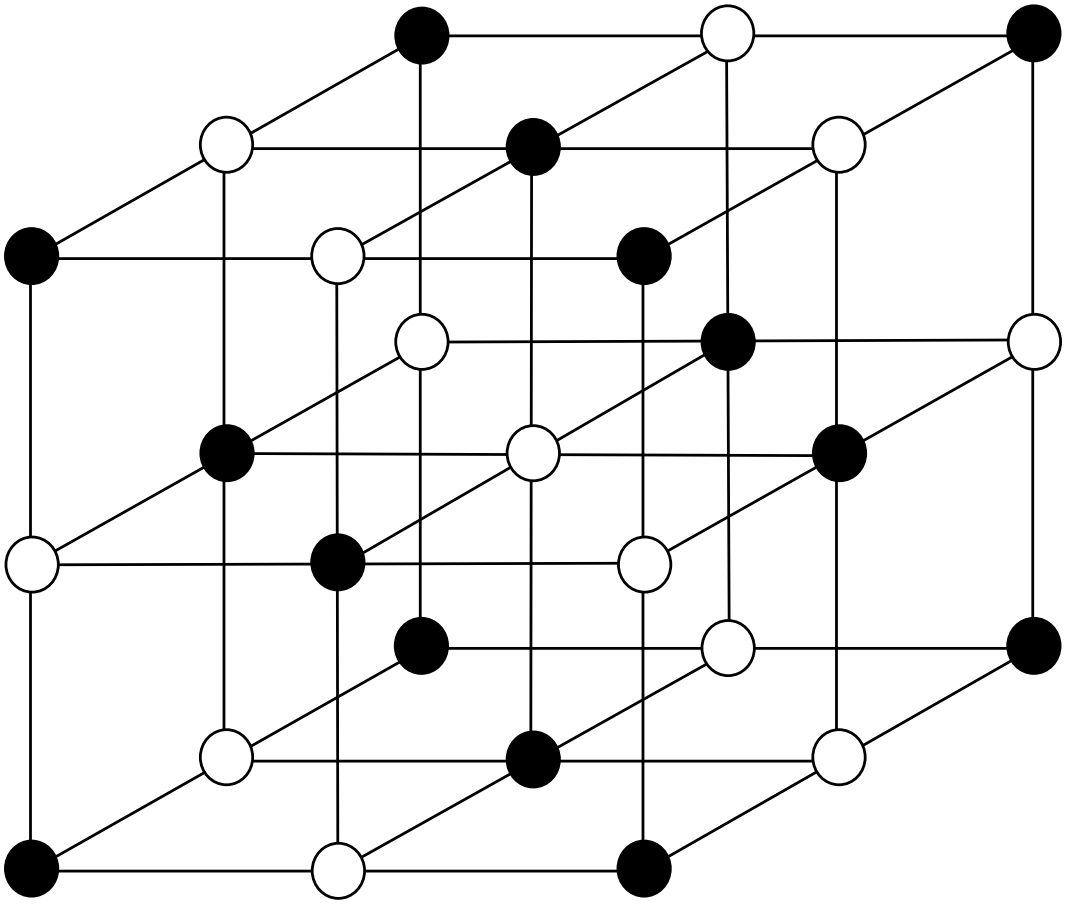

Figure 1.1: Atomic structure of halite: cations and oxygen ions situated on two interpenetrating face-centered cubic lattices.

1.1.3 Perovskites

The class of materials known as perovskites takes its name from the perovskite mineral, $CaTiO_3$, with a generic formula of ABO_3. The structural configuration is depicted in Figure 1.2, with a skeleton of oxygen octahedra around B-site cations at cube corners, and twelve-fold coordinated A-site cations at cube centers. The perovskites are important for their ferroelectric and piezoelectric properties as well as their high dielectric constants. Additional attention also stems from the role that perovskite structural elements hold in other material compounds, such as the high-temperature cuprate superconductors discovered in 1986 and the colossal magnetoresistive manganite materials identified in 1993. Finally, materials with perovskite structures maintain a central role in the geophysics of our Earth, as the predominant compound in the lower mantle is magnesium silicate[2, 4].

1.2 Growth of oxides

Oxides clearly demonstrate an amazing diversity of fundamental physics, associated properties, and critical applications. Yet, the realization of all of these possibilities, in terms of either samples to be explored or devices to be utilized, must be predicated upon the ability of scientists and engineers to grow such oxides. Although the growth of oxide materials, and the systematic and reproducible production of high-quality crystals, is by now a mature field, it remains yet an area of research that holds many tantalizing puzzles, especially regarding deposition and defect formation. As we shall discuss in Section 1.3, this dissertation seeks to address such questions and attempts to elucidate both certain experimental growth techniques, such as the pulsed laser deposition process depicted in Figure 1.3, as

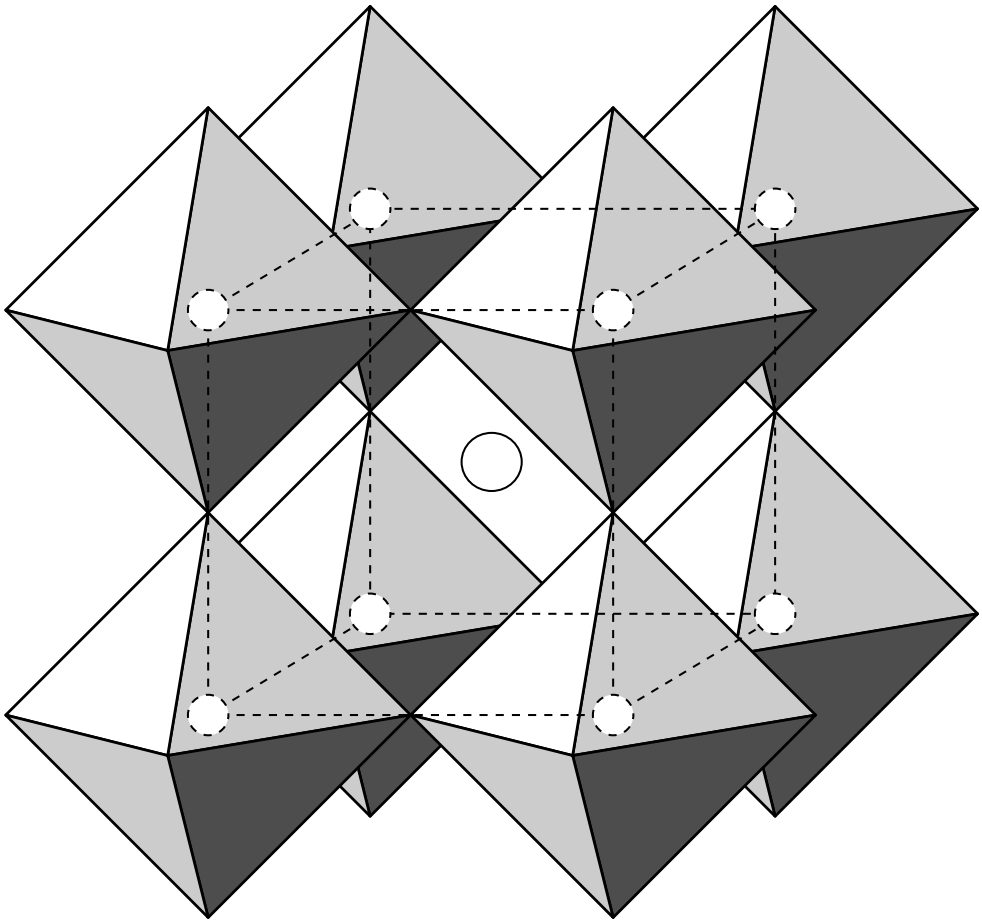

Figure 1.2: Atomic structure of cubic ABO_3 perovskite: oxygen octahedra surrounding B-site atoms, with A-site atoms outside the octahedra and equidistant from the B sites.

Figure 1.3: Crystal growth during pulsed laser deposition (photograph courtesy of Joel Brock, Cornell University).

well as the defects that accompany this growth. But first, we must review various experimental methods of crystal growth.

1.2.1 Early years

The history of crystal growth can be traced back to at least the mid-nineteenth century. In 1852, Groove invented ion-beam techniques to achieve non-thermal physical vapor deposition using glow discharge between electrodes. By 1857, Faraday had experimented with vacuum thermal physical vapor deposition, in which he deposited "burnt" metal wire upon a glass substrate in a neutral atmosphere[5]. By the 1880's, the field had gained sufficient prominence to generate review articles within an expanding body of literature[6].

Synthetic crystals were then grown commercially by the end of the nineteenth century. Known as the Geneva rubies, they were processed following the *flame-fusion* method invented by Verneuil, in which a powder source is melted by flame or plasma to create a film upon which the crystal can grow. Bridgman and Stockbarger pioneered more sophisticated *melt growth* techniques in 1925 and 1936, respectively; the Bridgman-Stockbarger method allowed for the growth of relatively complex oxides at reasonably rapid rates (for example, $Y_3Al_5O_{12}$ with a growth rate of 2 mm per hour and a melting point of $\sim$2250 K)[6].

While these methods proved instrumental in enabling rapid bulk crystalline growth at high temperatures within crucibles, other techniques were needed to explore the growth of crystals as thin films. Such thin film growth became known as *epitaxy*, or epitaxial growth, etymologically derived from the Greek "epi" and "taxis," meaning "attached to order"[7]. As such, epitaxial growth implies the

formation of an overgrowth on a substrate with a similar lattice arrangement. For situations in which these significantly smaller devices function appropriately, epitaxial thin film growth offers many advantages over melt growth, primarily in that higher quality crystal structures might be achieved due to associated lower growth temperatures[7].

The first systematic studies of epitaxial growth were conducted by Barker between 1906 and 1908, but it was the industrial need for solid-state devices that eventually propelled epitaxy from academic research to commercial focus. Until 1960, the semiconducting crystals, such as silicon and germanium, used in transistors were generated by melt growth and dopants were added by alloy processes[8]. Soon thereafter, the industry switched almost entirely to the creation of semiconducting devices by homoepitaxial growth, almost invariably employing chemical vapor deposition[8].

1.2.2 Classifications of growth

Scientists and inventors have discovered a great diversity of techniques for crystal growth over the past centuries, some of which are highlighted chronologically in Table 1.2. It is thus instructive to attempt to classify such disparate growth techniques into a series of major categories. The two most fundamental categorizations involve questions of physical versus chemical interactions and thermal versus non-thermal interactions. *Physical deposition* concerns physical interactions between the deposited material and the substrate and includes methods such as vacuum vapor evaporation, sputtering, and pulsed laser deposition. Alternatively, *chemical deposition* methods, such as electroplating or chemical vapor deposition, involve chemical reactions between the deposited material and the underlying substrate.

Table 1.2: Chronology of important development in crystal growth techniques[5].

Year	Inventor	Invention, discovery, or introduction of term
1643	E. Torricelli	Vacuum
1650	O. von Guericke	Vacuum pump
1834	M. Faraday	Ions†
1852	W. R. Groove	Diode sputtering
1857	M. Faraday	Thermal vapor deposition (exploding wire technique)
1887	R. Narwold	Thermal vacuum vapor deposition
1896	J. J. Thomson	Electrons
1898	W. Crookes	Ionization†
1907	F. Soddy	Reactive vapor deposition
1909	M. Knudsen	Distribution of emission of vapor deposited material
1909	J. Stark	Theory of sputtering
1910	A. Hull	Sputtering threshold energy
1928	I. Langmuir	Plasma†
1928	A. I. Shalnikov N. N. Syemyonov	Deposition from molecular beams
1932	J. K. Roberton C. W. Chapp	Deposition from high frequency plasma
1934	F. M. Penning	Magnetron
1937	B. Berghaus	Vapor deposition in vacuum with polarization of substrate
1950	M. von Ardenne	Deposition by ion beam
1951	L. Holland	Evaporation by ion beam
1958	W. Wroe	Evaporation by electric arc
1964	D. M. Mattox	Ion beam plating†
1968	J. R. Morely	Hollow cathode evaporation
1972	T. Takagi I. Yamada	Deposition from ionized clusters
1977	E. Moll	Deposition by thermo-ionic arc
1977	M. Sokolowski A. Sokolowski	Pulse-plasma deposition

† Discovery related to growth processes.

Thermal deposition implies relatively low and fairly uniform kinetic energies (generally of the order of 0.1 eV) of the particles in the deposited material and embodies the most conceptually basic method of thin film growth[9]. In contrast, in *non-thermal deposition*, the constituent atoms cannot be described as an ensemble with a Maxwell-Boltzmann distribution about a given temperature; such non-thermal distributions have excess energy selectively pumped (by laser light or electric field) into one or more degrees of freedom that are decoupled from the remainder of the ensemble. The benefit of this non-thermal distribution is that it potentially lowers the reaction activation barriers by controlling the electron energy distribution, which has negligible thermal mass, while the bulk of the thermal mass is carried by the remainder of the system. This allows for a thermally cool deposition chamber, even though the effective "temperature" of some electrons is quite high[9].

1.2.3 Vacuum thermal evaporation

Vacuum thermal evaporation is likely the most common thermal physical vapor deposition process. In this evaporation process, the material to be deposited is heated above its vapor pressure until it boils off and then subsequently condenses on a colder substrate. Vacuum thermal evaporation, as its name implies, requires low pressures (10^{-6}–10^{-5} torr) in the deposition chamber in order to prevent reactions between the material vapor and the ambient environment. During explicitly three-dimensional deposition, this method also suffers from *shadowing* or *step coverage* phenomena, in which subsequent thin-film layers are unable to achieve uniform coverage because existing deposits block further incoming trajectories. Additionally, the low thermal energy of the vapor atoms affects the morpholgy of thin films, often producing porous materials with adhesion issues. Vacuum thermal deposi-

tion was the first method ever used to achieve thin film growth, and, in fact, is still used today in the more refined form of molecular beam epitaxy[9].

1.2.4 Ion-beam techniques (sputtering)

Ion-beam techniques, such as *sputtering*, are among the most common non-thermal means of physical vapor deposition and are used extensively in semiconductor processing. These ion-beam techniques involve the mediation of the energy of an impinging flux of particles by an electric field. Specifically, in the sputtering process, positive ions are extracted from an electrical discharge and used to erode a target, ejecting particles of energies up to tens of eV; these target particles subsequently deposit onto a substrate and grow a crystal with the same stoichiometry as the original target. Control over the ambient background pressure can affect the particle impact parameter, preventing shadowing effects and allowing a range of collision types between direct bombardment (associated with lower ambient pressure) and thermal diffusion (higher pressure). These ion-beam methods also enable deposition for classes of materials that are unable to sustain their composition during the heating process of thermal vacuum evaporation. Unfortunately, sputtering suffers from the side effect that the sputtering plasma may erode the substrate surface[9].

1.2.5 Pulsed laser deposition

Pulsed laser deposition (PLD) is an important growth method, classified as non-thermal physical vapor deposition, with a number of advantages. It enables a great diversity of target materials, stringent control over thin film stoichiometries and

growth rates, and the creation of novel thin films with electronic states inaccessible to other vapor deposition methods that use only thermal energy scales. The PLD method utilizes photonic energy, from a pulsed laser incident upon a bulk target, to generate a plasma plume comprised of target particles with energies of tens of eV. Film growth is achieved as this plasma condenses upon a substrate, maintained in a vacuum chamber along with the target. The primary difficulties with PLD include the presence in the plasma plume of macroscopic particulates ejected during laser ablation of the target and the resulting defects and cratering of the thin film during growth[9].

1.2.6 Chemical vapor deposition

Chemical vapor deposition (CVD), the most common chemical deposition process for thin film growth, enables deposition through chemical decomposition or reaction of volatile gas-phase precursors of certain elements with a substrate surface. The resulting elements are then chemisorbed on the substrate while the fragments of reaction must be removed by gas flow in the reaction chamber, if they are not to disrupt growth. CVD thus allows for the control of dopant elements in a very precise manner with only modest vacuum requirements; additionally, it enables high growth rates while maintaining spatially uniform deposition. The resulting efficiency and cost effectiveness of CVD heavily favor it for industrial growth of semiconductor integrated circuits with micron length-scales[8, 9].

1.2.7 Molecular beam epitaxy

Molecular beam epitaxy (MBE), a successor to earlier vacuum thermal evaporation methods, is an unusual amalgamation of physico-chemical deposition processes. MBE combines constituent elements of the resulting thin film from separate sources, individual evaporation chambers that generate elemental atoms and molecules on thermal energy scales. The resulting vapors undergo very slow and quite controlled physical vapor deposition on the substrate. However, the component elements then chemically react, by chemabsorption, at the substrate surface. MBE thus enables the growth of extremely smooth thin films at low temperatures with impressive dimensional tolerance, stoichiometric control, and interfacial definition. As such, MBE is utilized within the research setting to explore the fundamental physics of semiconductor surfaces and thin films, while it is employed within the commercial environment to grow conventional and exotic microwave and optoelectronic structures. Additionaly, MBE has found particular relevance in the creation of periodic superlattice and quantum well structures, with exciting transport properties[10].

1.3 Overview of dissertation

The content of this dissertation can now better be understood within the context of the motivation for a study of oxides and a familiarity with the common means of growing such materials. This work is divided into the three following chapters, discussing deposition processes, point defects, and planar defects, respectively.

1.3.1 Deposition of magnesium oxide

In Chapter 2, we investigate cluster assimilation and collisional filtering on metal-oxide surfaces and present the first *ab initio* molecular dynamics study of collisions between metal-oxide clusters and surfaces. The resulting trajectories reveal that internal degrees of freedom of the cluster play a defining role in collision outcome. The phase space of incoming internal temperature and translational energy exhibits regions where the collision process itself ensures that clusters which do not rebound from the surface assimilate seamlessly onto it upon impact. This filtering may explain some aspects of recent observations of a "fast smoothing mechanism" during pulsed laser deposition.

1.3.2 Point defects in strontium titanate

While the above ultra-fast process displays fascinating physics on its relevant time scale, it does not necessarily capture all the effects of growth on a much longer time scale — the fact that growth processes do not always (and, in fact, only rarely) result in ideal development of perfect crystals. Deposition of material upon substrates almost always involves some deviation from perfect stoichiometry, with an associated generation of point defects, such as vacancies, which are then assimilated into the structure of the growing crystal. Therefore, in Chapter 3, we study point defects, specifically the elastic effects of vacancies in strontium titanate. We present a study of the local strain effects associated with vacancy defects in strontium titanate and report the first calculations of elastic dipole tensors and chemical strains for point defects in perovskites. The combination of local and long-range results will enable determination of x-ray scattering signatures that can be compared

with experiment. We find that the oxygen vacancy possesses a special property — a highly anisotropic elastic dipole tensor which almost vanishes upon averaging over all possible defect orientations. Moreover, through direct comparison with experimental measurements of chemical strain, we place constraints on the possible defects present in oxygen-poor strontium titanate and introduce a conjecture regarding the nature of the predominant defect in strontium-poor stoichiometries.

1.3.3 Planar faults in antiferrodistortive perovskites

Further study shows, however, that it is energetically favorable for point defects, such as TiO_2 vacancy complexes in the above strontium-titanate system, to gather into more ordered structures, such as stacking faults at planar interfaces — a process which we would expect to happen over yet longer time scales. Chapter 4 presents the most detailed and extensive theoretical study to date of the structural configurations of Ruddlesden–Popper (RP) phases in antiferrodistortive (AFD) perovskites and formulates a program of study which can be pursued for RP phases of any AFD perovskite system. We systematically investigate the effects of oxygen octahedral rotations on the energies of RP phases in AFD perovskites ($A_{n+1}B_nO_{3n+1}$) for $n = 1 \ldots 30$, providing asymptotic results for $n \to \infty$ that give both the form of the interaction between stacking faults and the behavior of such stacking faults in isolation. We find an inverse-distance interaction between faults with a strength which varies by as much as a factor of two depending on the configuration of the octahedra. We find that the strength of this effect can be sufficient to (a) stabilize or destabilize the RP phase with respect to dissociation into the bulk perovskite and the bulk A-oxide and (b) affect the energy scales of the RP phase sufficiently to constrain the rotational states of the octahedra neighboring

the stacking faults, even at temperatures where the octahedra in the bulk regions librate freely. Finally, we present evidence that the importance of the octahedral rotations can be understood in terms of changes in the distances between oxygen ions on opposing sides of the RP stacking faults.

1.4 Computational methods

This dissertation relies upon atomic level theories to perform the calculations summarized in Section 1.3. As such, it is instructive to discuss both the philosophy and derivation of such theories.

The atomistic philosophy traces its roots to the fifth century BCE and Democritus, an ancient Greek philosopher and the first of the so-called "atomists." Democritus proposed that all matter is comprised of such "indivisible" particles — immutable and indestructible and of infinite variety of size and shape — interspersed within a larger void. Supposedly, the rearrangement of positions of these atoms, and their interconnection through surface barbs and hooks, defined the macroscopic properties and nature of all objects[11]. Democritus expounded upon the central role of this atomistic picture, ascribing all conventional properties to these underlying particles: "by convention sweet and by convention bitter, by convention hot, by convention cold, by convention color; but in reality atoms and void"[12].

At first glance, Democritus's ancient outlook on natural philosophy might appear dated. Surely, physicists now recognize that atoms are not indivisible, but comprised of constituent electrons and nuclei, and condensed matter systems do not assemble by hook-and-latch connectors, but through the formalism of quantum

mechanics and electrostatics. Yet, for all of the myriad advances in understanding and application of physics over the intervening millenia, the importance of this central tenet still holds. Richard Feynman famously wrote in the beginning of his *Lectures on Physics*:

> If, in some cataclysm, all of scientific knowledge were to be destroyed, and only one sentence passed on to the next generation of creatures, what statement would contain the most information in the fewest words? I believe it is the atomic hypothesis (or the atomic fact, or whatever you wish to call it) that all things are made of atoms — little particles that move around in perpetual motion, attracting each other when they are a small distance apart, but repelling upon being squeezed into one another. In that one sentence, there is an enormous amount of information about the world, if just a little imagination and thinking are applied[13].

We thus recognize the benefits of perspective that both philosophies — early atomistic and modern electronic structure — present to enable us to study physical systems.

Regardless of their distinctions, these atomistic and electronic structure methods are both forms of microscopic descriptions, developed to reproduce all *relevant* microscopic degrees of freedom to capture the specific underlying behavior of a given system. They can be contrasted with phenomenological methods, such as continuum models, that treat a system in terms of displacement fields instead of atomic and electronic coordinates and attempt to portray the essense of the physics of a system while providing additional predictive power. Our preference is most definitely for the usage of microscopic models, although, in Chapter 3, we

will investigate the connections between microscopic (short-range) and continuum (long-range) descriptions of the same system.

The research comprising this dissertation leveraged both atomistic and electronic structure methods to calculate results. Atomistic modeling provided the speed and flexibility, compared to the more accurate electronic structure calculations, to enable us to survey the landscape of new systems and interactions and generate results in a timeframe that allowed for conjecture and refinement of theories. Alternatively, electronic structure calculations contained the rigor and exactitude that provided additional assurance our calculations and interpretations were not misguided. Thus, the course of this dissertation has compelled us to recognize the utility of combining these complementary approaches: atomistic simulations to survey the landscape of the problem, and, with sufficient computational time, electronic structure calculations to detail the solution.

1.4.1 Many-body Hamiltonian

We arrive at the power of both the atomistic and the electronic structure methods through a consideration of their assumptions and the relative simplifications they require of the full many-body quantum mechanical Hamiltonian. This Hamiltonian $\hat{H}$ is the Hermitian operator corresponding to the observable of total energy E in the many-body Schrödinger equation, taking the form,

$$\hat{H} \mid \Psi(\{\mathbf{R}_I, \mathbf{r}_i\}) \rangle = E \mid \Psi(\{\mathbf{R}_I, \mathbf{r}_i\}) \rangle , \tag{1.1}$$

where $\mathbf{R}_I$ represents nuclear degrees of freedom, and $\mathbf{r}_i$ electronic. This serves as the foundation for any method to develop a more tractable energy function. Explicitly denoting kinetic and interaction energy terms, this Hamiltonian takes

the form,

$$\hat{H} = -\frac{\hbar^2}{2m_e}\sum_i \nabla_i^2 - \sum_I \frac{\hbar^2}{2M_I}\nabla_I^2 + \tfrac{1}{2}\sum_{i\neq j}\frac{e^2}{|\mathbf{r}_i - \mathbf{r}_j|} + \tfrac{1}{2}\sum_{I\neq J}\frac{Z_I Z_J e^2}{|\mathbf{R}_I - \mathbf{R}_J|} - \sum_{i,I}\frac{Z_I e^2}{|\mathbf{r}_i - \mathbf{R}_I|}, \quad (1.2)$$

with terms representing the electronic kinetic energy, the nuclear kinetic energy, and the electron-electron, nucleus-nucleus, and electron-nucleus Coulomb interactions, respectively[14]. Motivated by the significant differences in mass of the nuclei and electrons, the Born-Oppenheimer approximation[15] simplifies this Hamiltonian, separating the timescales and the kinetics of the nuclei from those of the electrons. However, we are still left with a massively complicated Hamiltonian, one that both forms of microscopic methods, the atomistic and the electronic structure, seek to radically simplify[14].

Our two microscopic methods take different approaches to simplifying this Hamiltonian, although both seek to reduce the degrees of freedom and thus the difficulty in properly handling their interactions. The atomistic approach eliminates the electronic degrees of freedom completely, by replacing the exact energy with an approximation composed only of the degrees of freedom of the nuclei,

$$E_{\text{exact}}\left(\{\mathbf{R}_I, \mathbf{r}_i\}\right) \longrightarrow E_{\text{approx}}\left(\{\mathbf{R}_I\}\right). \quad (1.3)$$

This drastic simplification attempts to maintain the effect of the electronic degrees of freedom implicitly, even though only the nuclear degrees of freedom are expressed in the above energy approximation[16]. While atomistic approaches propose different parameterized functional relationships that incorporate these nuclear degrees of freedom, such methods are only able to achieve experimental agreement by fitting their respective parameters to existing empirical measurements. Thus, such atomistic methods are often known as *empirical potentials* and include traditional pair

potentials, pair functionals, angular force schemes, and cluster functionals, such as the Lennard-Jones potential[17], embedded-atom method[18, 19], Stillinger-Weber potential[20], and Tersoff cluster functional[21], respectively.

Similarly, the electronic structure approaches also seek to fold all the electronic degrees of freedom into a more agreeable form. However, these methods instead use a functional $\rho(\mathbf{r})$ to include the electronic contributions explicitly, rather than eliminating them completely,

$$\begin{aligned} E_{\text{exact}}(\{\mathbf{R}_I, \mathbf{r}_i\}) &\longrightarrow E_{\text{approx}}(\{\mathbf{R}_I, \mathbf{r}_i\}) \\ &\longrightarrow E_{\text{approx}}[\{\mathbf{R}_I\}, \rho(\mathbf{r})]. \end{aligned} \tag{1.4}$$

This form of simplification of the electronic degrees of freedom allows such *electronic structure calculations* to achieve a higher degree of accuracy than the empirical methods[16]. The reduced phase space of the approximation, due to the inclusion of $\rho(\mathbf{r})$, allows for the formulation of *ab initio* (literally, "from first principle") methods among the possible approaches to electronic structure calculations. Such *ab initio* methods require no parameterization of empirical inputs and thus reduce the possibility that the result of a given calculation is simply an outcome of the particular parameter fit. These improvements, however, demand greater, and at times *much* greater, computational resources than empirical methods. Tight-binding models[22, 23], density functional theories[24, 25], and molecular quantum chemistry approaches[26] demonstrate various popular techniques with which to perform electronic structure calculations.

1.4.2 Empirical potentials

Although many different empirical potentials have been developed, we largely concern ourselves here with only pair potentials and their extensions. Our rationale for this decision in our research is our view of empirical potentials and electronic structure calculations as two extremes along the continuum tradeoff of accuracy for computational cost and complexity. We have not thus far seen the need to develop or utilize empirical potentials of greater complexity without just resorting to a complete treatment of the system using the machinery of electronic structure calculations.

The pair potential introduces one of the most simple approximations suggested by (1.3), namely,

$$E_{\text{exact}}(\{\mathbf{R}_I, \mathbf{r}_i\}) \longrightarrow E_{\text{approx}}(\{\mathbf{R}_I\}) = \tfrac{1}{2}\sum_{i \neq j} V(R_{ij}), \tag{1.5}$$

where $V(R_{ij})$ is the pair potential and R_{ij} is the distance between the nuclei for atoms i and j. This type of pair potential reflects the outlook that the energy of the system can be considered in terms of the decomposition of the binding of different atoms into individual contributions that can be superimposed to provide the total energy. Then, only the form of $V(R_{ij})$ need be specified to develop a given pair potential and its parameterization[16]. We shall see, in Chapters 2, 3, and 4, the benefits of using different pair potentials to model systems of increasing complexity, as well as an extension of pair potentials to accommodate polarizability.

1.4.3 Density functional theory

Many computations benefit from greater accuracy than can generally be expected from empirical potentials and thus utilize some form of electronic structure calculations, often the density functional theory (DFT) methods. Not only does DFT provide this additional accuracy, but it also enables increased confidence in the resulting accuracy — especially for calculations that have not already been extensively explored using empirical potentials — due to its *ab initio* formulation, free from any fitting bias due to parameterization to a specific measurement. Further, since DFT explicitly includes the electronic degrees of freedom in (1.4), it generally enables a more transferable depiction of atoms and electronic bonding than that presented by the implicit treatment of electrons in empirical potentials. This transferability is important in ensuring that these computational methods can suitably model a diversity of physical systems without incorporating an intrinsic link to the specific systems on which they were developed or fit[14, 16].

DFT differs from earlier treatments of, and approximations to, the full many-body Hamiltonian in (1.2), with all of its electronic correlations and vast complexity. Rather than using the quantum-mechanical wavefunctions $\Psi(\{\mathbf{R}_I, \mathbf{r}_i\})$, DFT takes the ground-state electron density $n_0(\{\mathbf{r}_i\})$ as the fundamental variable of the system. In a seminal work in 1964, Hohenberg and Kohn proved both the existence of a universal functional for the energy in terms of the density, and the unique mapping between this ground-state electron density and the ground-state wavefunctions $\Psi_0(\{\mathbf{R}_I, \mathbf{r}_i\})$ of a many-body system[24]. They thus demonstrated that the ground-state density could be used to generate any property of a quantum many-body system in a completely exact manner. Hohenberg and Kohn also proved that the ground-state electron density minimized the total electronic

energy, as expressed by a functional of the density, of this many-body system. However, the Hohenberg-Kohn theorems served only as a proof of existence and not a prescription to generate the density functional[14].

The following year, Kohn and Sham introduced an *ansatz* to suggest meaningful approximations that enabled useful calculations[27]. Their *ansatz* stipulated that the many-body system may be replaced by an auxiliary *non-interacting* system that is assumed to contain the same ground-state density as the original interacting system. The associated Kohn-Sham equations are written in the form of single-particle Schrödinger equations,

$$\left[-\tfrac{\hbar^2}{2m_e}\nabla^2 + V_{\mathrm{KS}}(\mathbf{r}_i)\right]\psi_i(\mathbf{r}_i) = \epsilon_{\mathrm{i}}\,\psi_i(\mathbf{r}_i), \tag{1.6}$$

providing wavefunctions $\psi_i(\mathbf{r}_i)$ as solutions within this auxiliary non-interacting system with effective potential $V_{\mathrm{KS}}(\mathbf{r}_i)$[14, 16].

With a careful definition of this effective potential, Kohn and Sham were able to prove that the density functional $n_{\mathrm{KS}}(\mathbf{r}_i)$ of this non-interacting system minimizes not only its corresponding Hamiltonian, but also the Hamiltonian of the original many-body system. This process thus provides a solution for the many-body ground-state density functional in terms of the single-particle wavefunctions,

$$n_0(\{\mathbf{r}_i\}) \equiv n_{\mathrm{KS}}(\mathbf{r}_i) = \sum_i \left|\psi_i(\mathbf{r}_i)\right|^2. \tag{1.7}$$

In this manner, the final solution to the many-body system has been simplified, with no loss of accuracy in principle, to the solution of single-particle wavefunctions in the Kohn-Sham effective potential, where

$$V_{\mathrm{KS}} = V_{\mathrm{ext}} + V_{\mathrm{Hartree}} + V_{\mathrm{XC}}, \tag{1.8}$$

with terms representing the external potential, the electron-electron Coulomb repulsion, and the exchange-correlation effect, respectively. Exchange-correlation

(XC) encapsulates all the remainder of the many-body effects; while the Kohn-Sham solution is exact in principle, no exact expression for V_{XC} is yet known. In practice, approximations to the exchange-correlation term are used with great success: the Local Density Approximation (LDA) substitutes the density of a homogeneous electron gas for that of the true system[14, 16].

1.5 Cluster compute architecture

By now, we have well justified our need for modern computational tools to accomplish our program of investigation of the physics of deposition and defect formation in ceramic oxides. Such computational tools include not only a fast and modular software architecture, but also a robust and capable hardware architecture. The largest component of the former, our `DFT++` code for electronic structure calculations[28], has evolved and matured over the past ten years, nurtured by many successive graduate students. The latter served as an early project of mine, one that both enabled me to "get my hands dirty" and reinforced and impressed certain central tenets in assembling such resources.

Initially, in 2001, I proposed, architected, assembled, installed, and maintained our first-generation supercomputing cluster, comprised of approximately fifty dual-socket AMD Athlon nodes, each with two gigabytes of memory. Then, in 2007, I managed the engineering and infrastructure specifications for a dedicated two-hundred square-foot data center, with sophisticated and custom closed-loop air handling, to hold our current and future compute clusters and associated server and networking facilities. Finally, in 2008, I oversaw and directed the replacement of our first-generation cluster with an updated one comprised of more than

thirty dual-socket, quad-core, sixteen-gigabyte Intel Core2 nodes, as pictured in Figure 1.4 in an unquestionably aesthetically-disheveled state.

The primary lessons learned from this process relate to the incredible flexibility obtainable by completely controlling both the software and hardware infrastructure. This not only allows for selection of optimized instruction architecture, memory bandwidth, and network topology for the expected workloads, but also the provision of a vast, varied, and up-to-date collection of software applications and libraries in default logical system locations to increase productivity of software developers. The non-monetary cost of such power is felt most strenuously in the ongoing maintenance of such a system. I architected our clusters as diskless compute nodes — essentially, nothing more than power supplies, motherboards, CPU's, and memory in a node — that obtained their kernel, root filesystem, user directories, and everything else necessary for operation via a network bootstrap process. By ensuring that the compute nodes were thus relatively stateless, I was able to better modularize our system to allow for central provisioning of additional or replacement nodes by the addition of just a few keywords to a configuration file on a central server. Regardless of such attempts to minimize the drain on our time due to cluster maintenance, thermal issues proved the most vexing and taught the importance of due consideration to air flow and expected fan lifetime.

In reflecting upon the commitments inherent in such custom clusters, it is worthwhile to expound further upon the most recent advances in shared compute environments, even those not designed for high-performance scientific computing. These are exemplified by the Amazon Web Services[29], specifically the Elastic Compute Cloud (EC2), Elastic Block Store (EBS), and Simple Queue Service (SQS), and the competing Sun Grid Compute Utility[30], with utilization costs

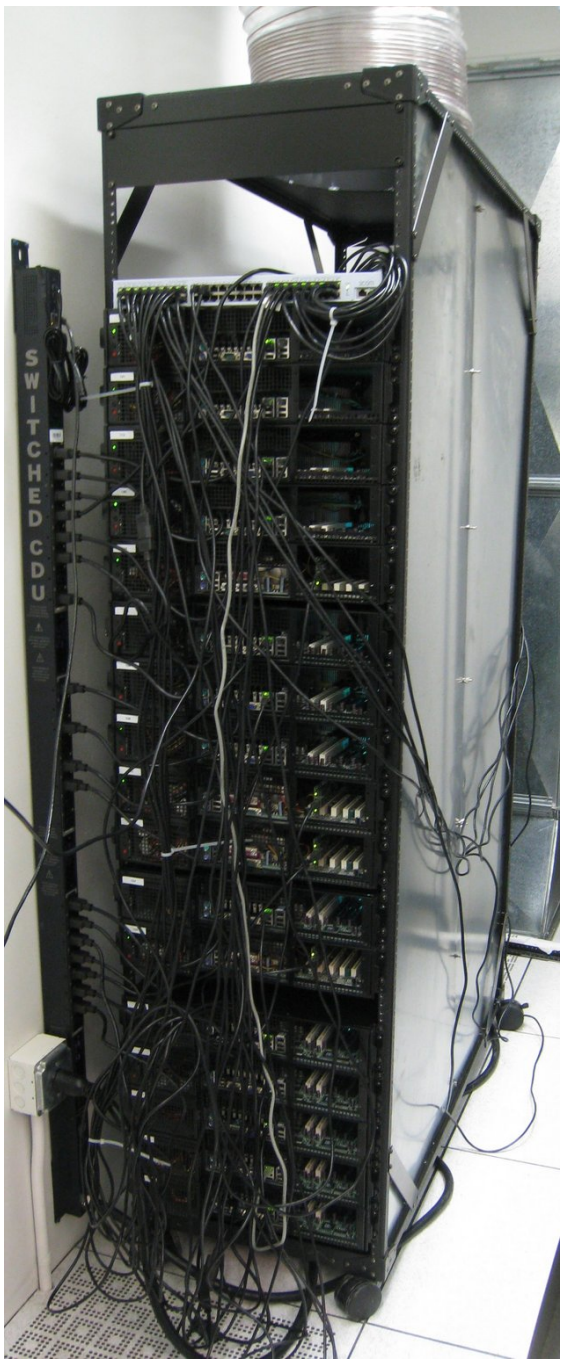

Figure 1.4: Photograph of second generation private computational supercomputing cluster showing sixteen of thirty-two diskless nodes located in custom data center in sub-basement of Clark Hall on Cornell University campus.

that scale linearly with cycles and storage. These services are unique in the commercial sector, at this time, in their virtualization of raw compute cycles, native block storage, and immediate fulfillment. Their primary advantage over massive dedicated scientific supercomputing centers is their low overhead to access. (No grants to write!) Potentially huge commercial utilization would likely lead to even further commoditization, with significant complementary downward cost pressure (much the same way the philosophy behind commodity Beowulf clusters[31] displaced reliance upon custom parallel supercomputers).

These types of facilities would allow scientists to remotely instantiate virtualized operating systems (say, our preferred Debian GNU/Linux distribution) and thus completely control the software infrastructure even while operating within a shared hardware infrastructure environment — but one that now requires no ongoing hardware maintenance. The tradeoffs that must be considered, however, primarily revolve around the loss of control of that hardware infrastructure, so that initial capital provisioning decisions cannot better align the hardware with any specific needs of a given scientific workload. Moreover, a much larger potential difficulty arises from the inability to control or necessarily even quantify the topology of virtual machine instances (either intra-node or inter-node). This might introduce possibly disastrous delays in execution as multiple virtual machines vie for contention of the memory bandwidth of a given node, or await the completion of a calculation by a slower member of a group engaged in message-passing for parallel computations. Thus, these compute environments might prove most useful for the class of calculations commonly termed "trivially parallelizable."

Irrespective of the varied choices in computational tools now available to physicists, our private compute cluster assuredly helped enable our research into depo-

sition and defects of ceramic oxides, which we now present in this dissertation. Furthermore, it encouraged proficiency with a central tool or instrument of computational physicists.

BIBLIOGRAPHY

[1] W. D. Kingery, H. K. Bowen, and D. R. Uhlmann. *Introduction to Ceramics*. John Wiley & Sons, New York, NY, USA, second edition, 1976. 1

[2] C. Barry Carter and M. Grant Norton. *Ceramic Materials: Science and Engineering*. Springer Science+Business Media, New York, NY, USA, 2007. 2, 3, 5

[3] W. Martienssen and H. Warlimont, editors. *Springer Handbook of Condensed Matter and Materials Data*. Springer Berlin Heidelberg, Berlin, DE, 2005. 2

[4] Francis S. Galasso. *Structure, Properties and Preparation of Perovskite-Type Compounds*. Pergamon Press, Oxford, UK, 1969. 5

[5] Tadeusz Burakowski and Wierzchoń Burakowski. *Surface engineering of metals: principles, equipment, technologies*. CRC Press, Boca Raton, FL, USA, 1999. 8, 10

[6] J. C. Brice. The growth of insulating crystals. *Rep. Prog. Phys.*, 40(5):567–602, 1977. 8

[7] G. B. Stringfellow. Epitaxy. *Rep. Prog. Phys.*, 45(5):469–525, 1982. 8, 9

[8] B. A. Joyce. The growth and structure of semiconducting thin films. *Rep. Prog. Phys.*, 37(3):363–420, 1974. 9, 13

[9] P. R. Willmott and J. R. Huber. Pulsed laser vaporization and deposition. *Rev. Mod. Phys.*, 72(1):315–328, 2000. 11, 12, 13

[10] B. A. Joyce. Molecular beam epitaxy. *Rep. Prog. Phys.*, 48(12):1637–1697, 1985. 14

[11] Sylvia Berryman. Democritus. In Edward N. Zalta, editor, *The Stanford Encyclopedia of Philosophy*. Fall 2008. 17

[12] Hermann Diels and Walther Kranz. *Die Fragmente der Vorsokratiker*, page 68B9. Weidmannsche Verlagbuchhandlung, Berlin-Grunewald, DE, sixth edition, 1951. 17

[13] Richard P. Feynman, Robert B. Leighton, and Matthew Sands. *The Feynman Lectures on Physics: Mainly Mechanics, Radiation, and Heat*, volume I of *The Feynman Lectures on Physics*. Addison-Wesley, Reading, MA, USA, 1963. 18

[14] Richard M. Martin. *Electronic Structure: Basic Theory and Practical Methods*. Cambridge University Press, Cambridge, UK, 2004. 20, 23, 24, 25

[15] M. Born and R. Oppenheimer. Zur Quantentheorie der Molekeln. *Ann. Phys.*, 389(20):457–484, 1927. 20

[16] Rob Phillips. *Crystals, Defects and Microstructures: Modeling Across Scales*. Cambridge University Press, Cambridge, UK, 2001. 20, 21, 22, 23, 24, 25

[17] J. E. Lennard-Jones. Cohesion. *Proc. Phys. Soc.*, 43(5):461–482, 1931. 21

[18] Murray S. Daw and M. I. Baskes. Semiempirical, Quantum Mechanical Calculation of Hydrogen Embrittlement in Metals. *Phys. Rev. Lett.*, 50(17):1285–1288, 1983. 21

[19] Murray S. Daw and M. I. Baskes. Embedded-atom method: Derivation and application to impurities, surfaces, and other defects in metals. *Phys. Rev. B*, 29(12):6443–6453, 1984. 21

[20] Frank H. Stillinger and Thomas A. Weber. Computer simulation of local order in condensed phases of silicon. *Phys. Rev. B*, 31(8):5262–5271, 1985. 21

[21] J. Tersoff. New Empirical Model for the Structural Properties of Silicon. *Phys. Rev. Lett.*, 56(6):632–635, 1986. 21

[22] J. C. Slater and G. F. Koster. Simplified LCAO Method for the Periodic Potential Problem. *Phys. Rev.*, 94(6):1498–1524, 1954. 21

[23] C. M. Goringe, D. R. Bowler, and E. Hernández. Tight-binding modelling of materials. *Rep. Prog. Phys.*, 60(12):1447–1512, 1997. 21

[24] P. Hohenberg and W. Kohn. Inhomogeneous Electron Gas. *Phys. Rev.*, 136(3B):B864–B871, 1964. 21, 23

[25] Robert G. Parr and Weitao Yang. *Density-Functional Theory of Atoms and Molecules*. Oxford University Press, New York, NY, USA, 1989. 21

[26] Attila Szabo and Neil S. Ostlund. *Modern Quantum Chemistry*. McGraw-Hill Publishing, New York, NY, USA, first revised edition, 1989. 21

[27] W. Kohn and L. J. Sham. Self-Consistent Equations Including Exchange and Correlation Effects. *Phys. Rev.*, 140(4A):A1133–A1138, 1965. 24

[28] Sohrab Ismail-Beigi and T. A. Arias. New algebraic formulation of density functional calculation. *Comput. Phys. Commun.*, 128(1–2):1–45, 2000. 25

[29] Amazon Web Services. `http://aws.amazon.com/`, 2008. 26

[30] Sun Grid Compute Utility Developer Resources. `http://developers.sun.com/sungrid/`, 2009. 26

[31] Beowulf.org: The Beowulf Cluster Site. `http://www.beowulf.org/`, 2009. 28

CHAPTER 2

CLUSTER ASSIMILATION AND COLLISIONAL FILTERING ON METAL-OXIDE SURFACES

The success of pulsed laser deposition of complex oxide films raises the fundamental question of how a disordered distribution of incoming clusters incorporates seamlessly into highly ordered crystals with complex unit cells. In pulsed laser deposition, a laser pulse impinges upon a target and ejects hot material into a plasma plume which then condenses upon a growing substrate[1]. With empirical tuning of parameters such as laser wavelength and energy density, laser pulse width and separation, partial pressure of the ambient gas, and substrate temperature, the resulting film can be made to grow smoothly and nearly defect free[2]. Little is known about what underlying fundamental processes these external parameters control. In recent years, sub-second time-resolved *in situ* x-ray measurements of growth by this process have become possible[3, 4]. These experiments suggest that incoming clusters from the plume are incorporated into the substrate on sub-millisecond time scales in a "fast smoothing mechanism" which occurs too quickly to be explained by traditional diffusional smoothing[4, 5]. The present work addresses the question of whether smoothing mechanisms exist over the time scale of the actual *collisions* between the clusters and the surface.

To address the existence of such collisional mechanisms, atomistic, as opposed to continuum, descriptions of growth are most appropriate. Current atomistic studies of crystal growth employ a number of methods, such as kinetic Monte Carlo[6–8], molecular dynamics based on classical interatomic potentials[9–11], combinations of the two[12, 13], accelerated molecular dynamics[14], and *ab initio* calculations of already deposited material[15–17]. However, kinetic Monte Carlo

methods, by their nature, handle only diffusive events, not actual deposition dynamics. Although classical molecular dynamics can address collisions, the use of interatomic potentials raises the issue of accuracy, particularly in oxides, which generally have a number of different atomic species and complex physical chemistry. While *ab initio* studies of already deposited material give insights into metastable structures and transition states, they do not do so for the kinetic mechanisms active during collisions. To study such mechanisms, this work presents the first *ab initio* molecular dynamics calculations of collisions between metal-oxide clusters and surfaces, with magnesium oxide selected as a simple model system.

2.1 Methods

All density functional theory[18] calculations below employ the local density approximation[19] and use the total-energy plane-wave pseudopotential technique[20] with a 20 hartree (20 H) cutoff. The pseudopotentials include non-local corrections of the Kleinman-Bylander form[21] for the p and d channels.

We represent the MgO (001) surface with a 3×3 periodic supercell and three layers of atoms. The surface slabs are separated by 12.10 Å or 18.15 Å of vacuum for cold and hot incoming clusters, respectively. The in-plane lattice constant of the supercell (8.55 Å) corresponds to that of the relaxed bulk crystal. Finally, we integrate over the Brillouin zone for this wide band-gap insulator using a single k-point at the zone center.

For molecular dynamics, we employ the Verlet algorithm[22] using a time step of 2.04 fs. We maintain the electrons within 0.1 mH of the Born-Oppenheimer surface using preconditioned conjugate-gradients within the analytically continued functional approach[23]. These parameters conserve total energy to within 3 mH

(0.3% of the collision energy) throughout. The initial condition of the slab is taken to be its fully relaxed vacuum configuration at zero temperature, with the bottom layer fixed at bulk locations, a constraint also maintained during the molecular dynamics.

To study incorporation of clusters beyond the size of simple molecular units, we study collisions with the eight-atom ($N_{\rm cl} \equiv 8$) cubic "magic cluster"[24]. To explore the role of internal degrees of freedom, we consider otherwise identical collisions with both "cold" and "hot" incoming clusters. We prepare the cold cluster by full relaxation in vacuum and the hot cluster by adiabatic heating (with no net momentum or angular momentum) to an internal kinetic energy of $K_{\rm int} = 0.057$ H. This energy corresponds to an internal temperature of $T = K_{\rm int}/(3N_{\rm cl}k_B/2) \sim$ 1500 K, well below the bulk melting temperature, both *ab initio* (3110 K[25]) and experimental (3250 K[26]). Finally, we give the incoming clusters a translational kinetic energy representative of the range ($\sim$10 to $\sim$100 eV) which yields smooth growth in energetic deposition[1, 27]. In particular, we choose 1 H ($\approx$ 27.21 eV), near the geometric mean of this range.

2.2 Results

Figure 2.1 presents snapshots of our raw results at representative times. The central result for the cold cluster (top row) is that it rebounds and does not bind to the surface. Initially ($t = 0.05$ ps), the cold cluster approaches the surface. After contact of the electron clouds, the cluster compresses while pushing atoms on the surface into the slab ($t = 0.20$ ps). The cluster then rebounds into the environment ($t = 0.35$ ps) and does not contribute to growth of the surface.

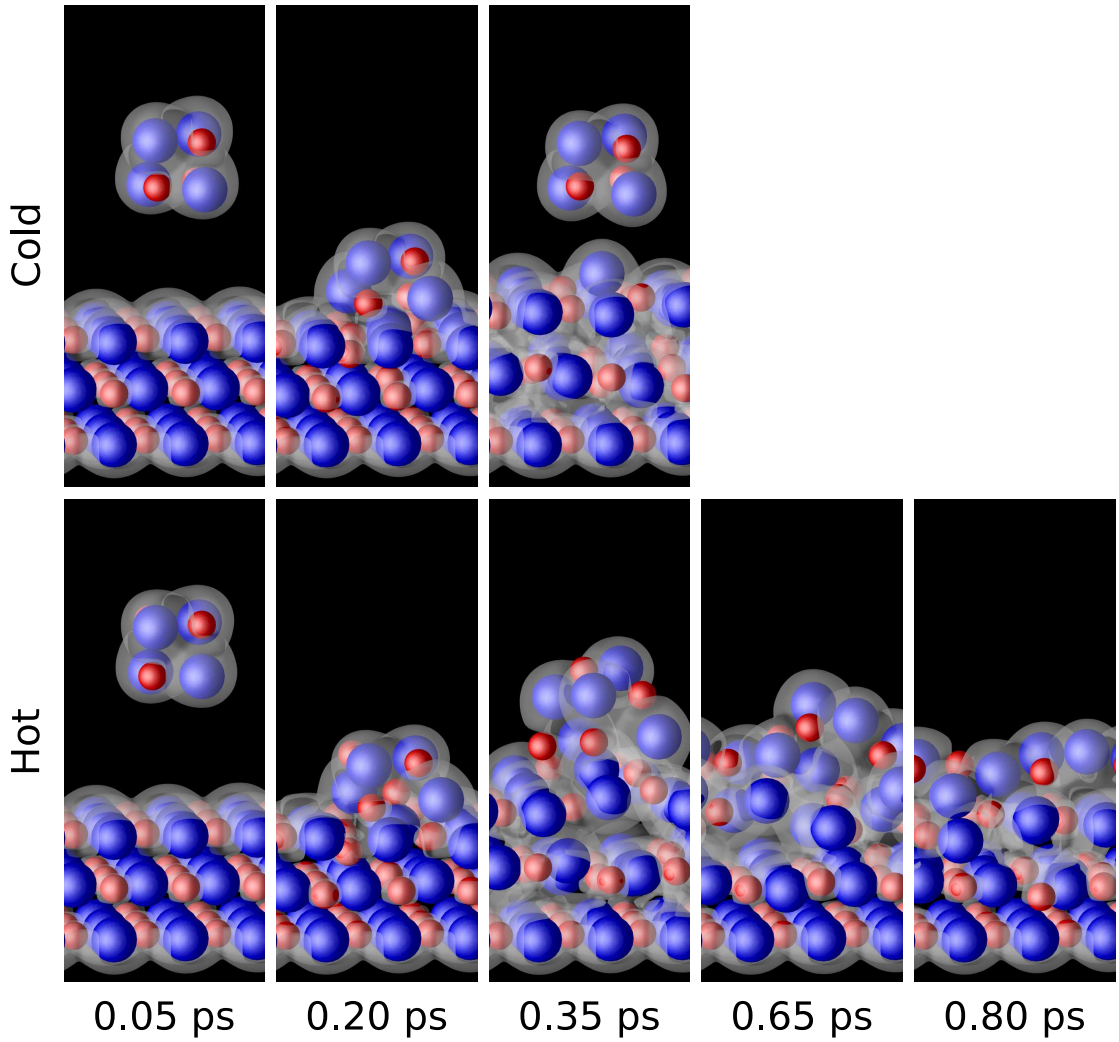

Figure 2.1: *Ab initio* molecular dynamics snapshots of hot and cold clusters in collision with magnesium-oxide surface: Mg cores (red), O cores (blue), electron-density isosurfaces (white), coordinate axes (upper right panel).

In marked contrast, the hot cluster binds to the surface. Initially ($t = 0.05$ ps), it approaches the surface with ∼1500 K of internal kinetic energy and the same impact parameters and velocity as the cold cluster. After contact, this cluster also compresses while pushing atoms on the surface into the slab ($t = 0.20$ ps) in a configuration quite similar to that of the cold cluster. This collision dissipates sufficient translational kinetic energy for the cluster to bind to the surface ($t = 0.35$ ps). Bound, the cluster equilibrates with the surface until it assumes a rock-salt configuration conforming to the underlying crystal ($t = 0.65$ ps). Thereafter, the cluster cools until thermal vibration accounts for the remaining distortions ($t = 0.80$ ps), at which point the cluster has assimilated seamlessly onto the underlying surface.

To aid interpretation of the snapshots of the hot cluster, Figure 2.2 presents the internal kinetic energy (expressed as a temperature) of the hot cluster and the slab as a function of time. To reduce the appearance of fluctuations associated with the small numbers of atoms, we convolve the data with a Gaussian of width 0.05 ps. Impact occurs in the first interval indicated in the figure ($t < 0.20$ ps), during which the temperature of the slab and cluster both rise. In the following two intervals (0.20 ps $< t <$ 0.50 ps; 0.50 ps $< t$), the temperature of the slab rises consistently. In contrast, the temperature of the cluster oscillates during the second interval (0.20 ps $< t <$ 0.50 ps) and then drops consistently toward that of the slab during the final interval (0.50 ps $< t$). Finally, we note that a similar analysis shows that the temperature of the cold cluster also rises during the collision, but only to approximately 2000 K, well below the bulk melting point of $\sim$ 3100 K.

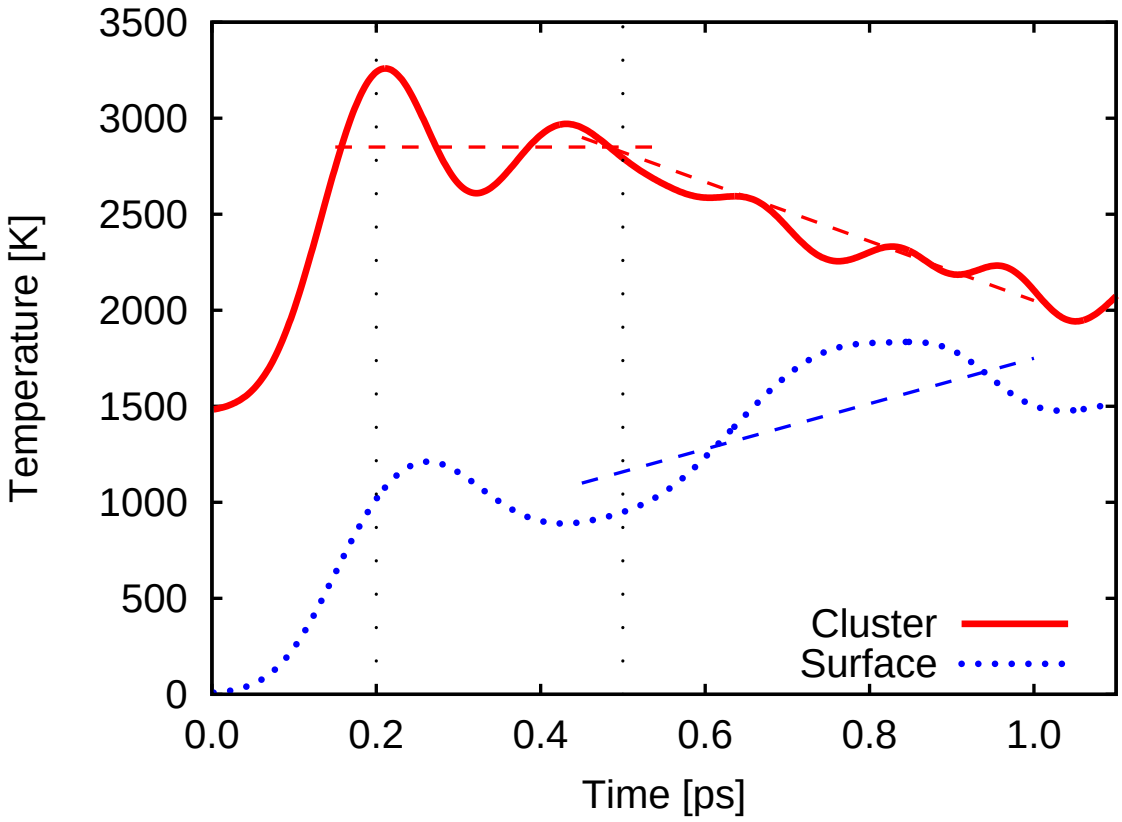

Figure 2.2: Cluster (solid red curve) and surface (dotted blue curve) temperature versus time: impacting, freezing, cooling intervals (left to right, demarked by dashed vertical lines). Dashed horizontal and diagonal lines are guides to the eye.

2.3 Discussion

During its collision, the cold cluster never reaches the melting point and, recovering its initial form, is able to convert enough of the energy stored during the impact back into translational motion to escape the surface. In contrast, the hot cluster approaches the melting point on impact and loses its original structure. Thereafter, it cannot convert sufficient energy from the impact into translational motion to escape the surface.

Despite the small number of atoms in the cluster, thermodynamic concepts provide a useful framework for these observations. If we describe the disordering of the hot cluster as "melting," then the translational energy which the hot cluster is unable to recover is analogous to the latent heat of fusion. We then expect the melted cluster to equilibrate with the underlying surface — first by maintaining a constant temperature while releasing the heat of fusion into the surface, and then by cooling until its temperature matches that of the surface.

The internal temperature of the hot cluster (Figure 2.2) arguably shows just this behavior. During the impact in the first interval ($t < 0.20$ ps), the internal energy of the hot cluster rises to approach the bulk melting point (3100 K). In the second, "freezing," interval (0.20 ps $< t <$ 0.50 ps), the temperature shows fluctuations around a relatively constant value (horizontal dashed line in Figure 2.2). Consistent with this, the snapshot from the center of this interval ($t = 0.35$ ps) shows a cluster in the midst of changing its topology to conform to the underlying surface. In the third interval (0.50 ps $< t$), the cluster cools while the surface heats as the two equilibrate to a common temperature. Snapshots from this interval ($t = 0.65$ ps and $t = 0.80$ ps) show the cluster assimilated into the surface, with only thermal vibrational motion remaining.

Within the preceding framework, we make the following predictions. First, the temperature of a cluster which ensures melting upon impact should decrease with increasing incoming translational energy. There thus should be a *melting curve* in the phase space of incoming cluster temperature versus incoming translational energy, above which the cluster melts upon impact. This curve has a horizontal asymptote at the melting temperature of the cluster for low translational energies, with a horizontal intercept where the translational energy alone is sufficient to melt the cluster. Second, the cluster temperature which ensures binding after impact should increase with increasing translational energy because internal temperature promotes absorption of mechanical energy. There thus should be a *binding curve* in the phase space above which the cluster binds. This curve has a horizontal intercept at the incoming energy below which the attraction between cluster and surface always suffices to bind the cluster, followed by a vertical asymptote at the translational energy above which the cluster never absorbs sufficient energy to allow binding. Due to the ratio of bulk to surface bonds in the cluster, the translational energy above which the cluster always melts should be greater than the energy below which it always binds, so that, in general, the melting and binding curves cross. Finally, we expect that collisions will begin to disrupt the topology of the surface for translational energies somewhere near the point where there is enough energy to melt cold clusters upon impact, thus defining a *disruption curve*.

Figure 2.3 shows this phase space. In particular, Figure 2.3(a) illustrates a *melting curve*, *binding curve* and *disruption curve*, and indicates points corresponding to the above *ab initio* molecular dynamics calculations. (The specific placement of the curves and background coloring derive from classical molecular dynamics simulations described below.) The melting and binding curves define four regions in the phase space: *assimilation*, *reflection*, *tumultuation*, and *sedimentation*. In

the region above both curves, clusters bind and melt and subsequently deform and *assimilate* seamlessly onto the surface upon impact. In the region below both curves, clusters neither bind nor melt and thus *reflect* intact from the surface. In the region above the melting but below the binding curve, clusters melt but do not bind and thus *tumult* from the surface in a deformed state. In the region above the binding but below the melting curve, clusters bind but do not melt and thus *sediment* intact on the surface. Finally, the *disruption* curve defines the region where the surface topology is disrupted. The *ab initio* results conform to this demarcation of phase space, with the translational energy of 1 H such that the cold cluster (lower purple star in Figure 2.3(a)) reflects and the hot cluster (upper purple star in Figure 2.3(a)) assimilates.

To test whether these conclusions are general and insensitive to details of the underlying interactions, we construct a simple interatomic potential model of a generic divalent ionic crystal in the form of a Coulomb interaction and a pairwise short-range repulsion,

$$U = \tfrac{1}{2} \sum_{i \neq j} \left[\frac{q_i q_j}{r_{ij}} \left(1 - \operatorname{erfc} \tfrac{r_{ij}}{a_{ij}} \right) + A_0 \, e^{-(r_{ij}/a_{ij})^2} \right],$$

where we work in atomic units, U is the total energy of the crystal, $q_i = \pm 2$ are the ionic charges, r_{ij} is the distance between atoms i and j, $A_0 = 7$ H (fit to compromise between the lattice constant and bulk modulus of MgO) measures the strength of the repulsion between ionic cores, and a_{ij} is a range parameter defined as the mean ionic radius of atoms i and j ($R_{\mathrm{Mg}} = 0.66$ Å, $R_{\mathrm{O}} = 1.32$ Å). The "erfc" term is part of the short-range repulsion between ionic cores and serves to remove the Coulomb singularity when the ionic cores overlap. This simple model material prefers rock-salt over the cesium-chloride structure, as does magnesium oxide, and has a lattice constant and bulk modulus of 5.0 Å and 240 GPa, both significantly

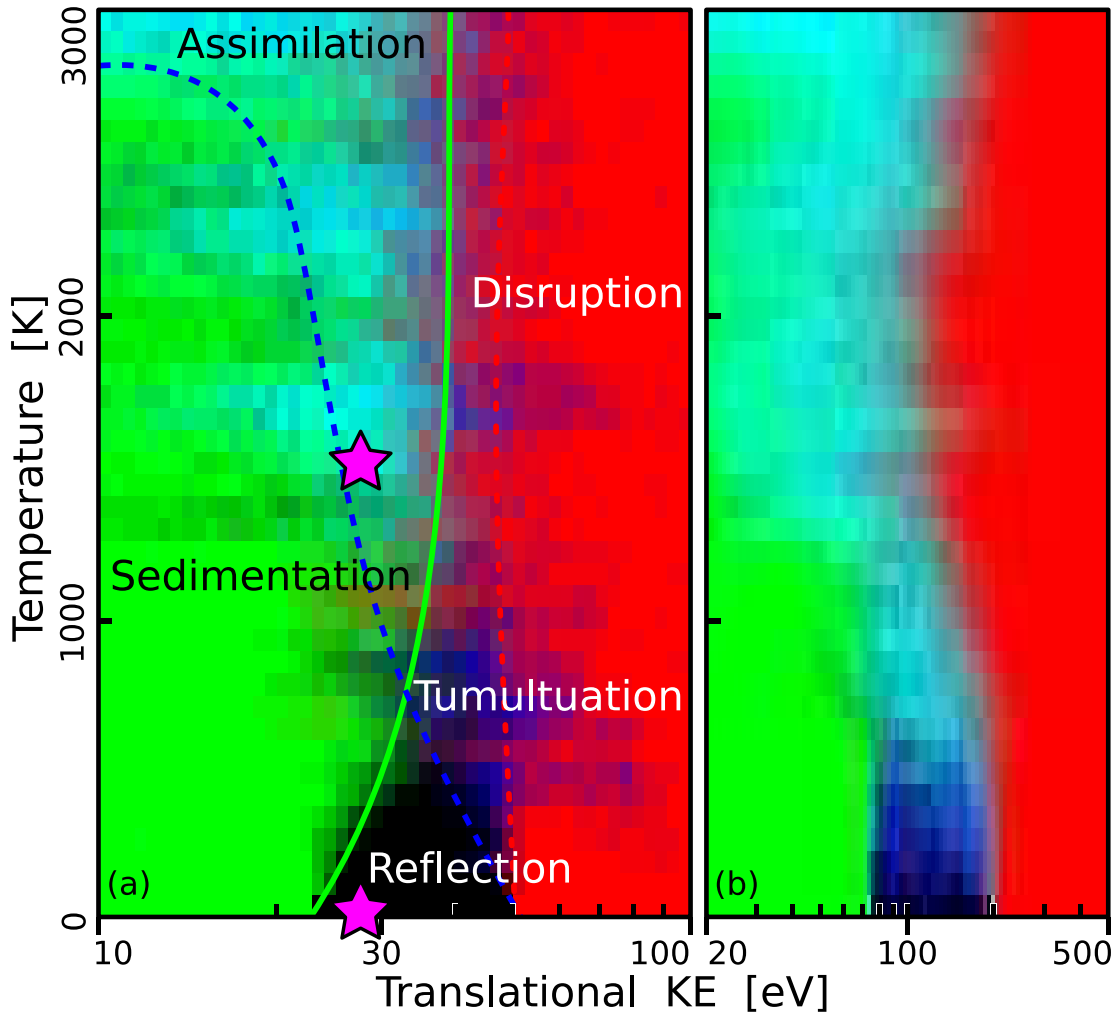

Figure 2.3: Phase space of incoming temperature versus translational energy for (a) small and (b) large supercells: *ab initio* results (purple stars); proposed *melting curve* (dashed blue), *binding curve* (solid green) and *disruption curve* (dotted red) overlaid on regions of *assimilation* (cyan), *reflection* (black), *tumultuation* (blue), *sedimentation* (green), and *disruption* (red), from classical molecular dynamics simulation.

larger (20% and 50%, respectively) than the corresponding experimental quantities for magnesium oxide.

Using the above model, we repeat the procedure of the *ab initio* molecular dynamics calculations in the same three-layer 3×3 supercell, but now map the phase space in detail: on a grid of 40 values of incoming temperature and 50 values of translational energy, sampling 25 collisions at each phase-space point, for a total of 50 000 trajectories. To explore convergence with system size, we also study a five-layer 6×6 supercell using 100 000 trajectories. Figures 2.3(a,b) summarize these results. The blue intensity of each pixel encodes the probability of melting; the green encodes that of binding; and the red channel encodes disruption, overriding blue and green regardless of cluster behavior. Points where clusters disrupt the surface thus appear red, whereas points where clusters assimilate appear cyan, reflect appear black, tumult appear blue, and sediment appear green. The pixelization of the figure reflects the discreteness of the sampling and the fluctuations reflect Poisson statistics ($\pm 20\%$).

Remarkably, the data in both Figures 2.3(a,b) correspond precisely to the expectations of the physical picture developed above. In particular, we find the expected five regions of behavior separated by the anticipated curves. Even *quantitatively*, within the corresponding supercell, the *ab initio* results fall correctly into the assimilation and reflection regions, despite the relatively small area of these regions and the quantitative differences between the *ab initio* and model materials. The larger supercell results show the same overall behavior, with quantitative correspondence for the internal temperatures and some rescaling of the translational energy. The latter effect, we believe, results from a deeper surface providing a more "cushioned" impact.

2.4 Conclusion

We present the first direct Born-Oppenheimer *ab initio* molecular dynamics calculations to demonstrate that metal-oxide clusters can assimilate seamlessly onto metal-oxide surfaces during the collisional time scale ($\sim$1 ps) — far shorter than diffusional time scales. These calculations, along with extensive classical molecular dynamics simulations and general physical considerations, support the novel picture that the internal degrees of freedom of the incoming clusters play an important role in deposition. The phase space of incoming temperature and translational energy summarizes important features of collision outcome, distinguishing regions of melting and binding in terms of curves whose behavior is easily understood.

The resulting phase diagram leads to new insights into pulsed laser deposition. Each laser pulse produces an ensemble of clusters scattered across the phase space. For translational energies typical of experimental conditions for smooth growth, the arrangement of regions in the phase diagram indicates that the collision process itself provides an effective filter to ensure assimilation of clusters onto the surface *upon impact*. For translational energies above the crossing of the melting and binding curves, incoming clusters which manage to bind also melt, and thus assimilate rather than sediment. We believe that this result may relate to observations of a "fast smoothing mechanism" in growth by pulsed laser deposition[4, 5].

BIBLIOGRAPHY

[1] P. R. Willmott and J. R. Huber. Pulsed laser vaporization and deposition. *Rev. Mod. Phys.*, 72(1):315–328, 2000. 33, 35

[2] Douglas B. Chrisey and Graham K. Hubler. *Pulsed Laser Deposition of Thin Films*. John Wiley, New York, NY, USA, 1994. 33

[3] G. Eres, J. Z. Tischler, M. Yoon, B. C. Larson, C. M. Rouleau, D. H. Lowndes, and P. Zschack. Time-resolved study of $SrTiO_3$ homoepitaxial pulsed-laser deposition using surface x-ray diffraction. *Appl. Phys. Lett.*, 80(18):3379, 2002. 33

[4] Aaron Fleet, Darren Dale, Y. Suzuki, and J. D. Brock. Observed Effects of a Changing Step-Edge Density on Thin-Film Growth Dynamics. *Phys. Rev. Lett.*, 94(3):036102, 2005. 33, 44

[5] P. R. Willmott, R. Herger, C. M. Schlepütz, D. Martoccia, and B. D. Patterson. Energetic Surface Smoothing of Complex Metal-Oxide Thin Films. *Phys. Rev. Lett.*, 96(17):176102, 2006. 33, 44

[6] E. A. Kotomin, V. N. Kuzovkov, G. Zvejnieks, Yu. Zhukovskii, D. Fuks, S. Dorfman, and A. M. Stoneham. The kinetic MC modelling of reversible pattern formation in initial stages of thin metallic film growth on crystalline substrates. *Solid State Commun.*, 125(9):463–467, 2003. 33

[7] Pui-Man Lam, S. J. Liu, and C. H. Woo. Monte Carlo simulation of pulsed laser deposition. *Phys. Rev. B*, 66(4):045408, 2002.

[8] O. Malis, J. D. Brock, R. L. Headrick, Min-Su Yi, and J. M. Pomeroy. Ion-

induced pattern formation on Co surfaces: An x-ray scattering and kinetic Monte Carlo study. *Phys. Rev. B*, 66(3):035408, 2002. 33

[9] X. W. Zhou, D. A. Murdick, B. Gillespie, and H. N. G. Wadley. Atomic assembly during GaN film growth: Molecular dynamics simulations. *Phys. Rev. B*, 73(4):045337, 2006. 33

[10] Andrés Aguado and Paul A. Madden. Fully transferable interatomic potentials for large-scale computer simulations of simple metal oxides: Application to MgO. *Phys. Rev. B*, 70(24):245103, 2004.

[11] Momoji Kubo, Yasunori Oumi, Ryuji Miura, Adil Fahmi, Andras Stirling, Akira Miyamoto, Masashi Kawasaki, Mamoru Yoshimoto, and Hideomi Koinuma. Layer-by-layer homoepitaxial growth process of MgO (001) as investigated by molecular dynamics, density functional theory, and computer graphics. *J. Chem. Phys.*, 107(11):4416–4422, 1997. 33

[12] Joachim Jacobsen, B. H. Cooper, and James P. Sethna. Simulations of energetic beam deposition: From picoseconds to seconds. *Phys. Rev. B*, 58(23): 15847–15865, 1998. 33

[13] Joshua M. Pomeroy, Joachim Jacobsen, Colin C. Hill, Barbara H. Cooper, and James P. Sethna. Kinetic Monte Carlo–molecular dynamics investigations of hyperthermal copper deposition on Cu(111). *Phys. Rev. B*, 66(23):235412, 2002. 33

[14] Arthur F. Voter, Francesco Montalenti, and Timothy C. Germann. Extending the time scale in atomistic simulation of materials. *Annu. Rev. Mater. Sci.*, 32:321–346, 2002. 33

[15] Jean-Yves Raty, François Gygi, and Giulia Galli. Growth of Carbon Nanotubes on Metal Nanoparticles: A Microscopic Mechanism from *Ab Initio* Molecular Dynamics Simulations. *Phys. Rev. Lett.*, 95(9):096103, 2005. 33

[16] V. Musolino, A. Selloni, and R. Car. Structure and Dynamics of Small Metallic Clusters on an Insulating Metal-Oxide Surface: Copper on MgO(100). *Phys. Rev. Lett.*, 83(16):3242–3245, 1999.

[17] G. Barcaro, A. Fortunelli, F. Nita, and R. Ferrando. Diffusion of Palladium Clusters on Magnesium Oxide. *Phys. Rev. Lett.*, 95(3):246103, 2005. 33

[18] P. Hohenberg and W. Kohn. Inhomogeneous Electron Gas. *Phys. Rev.*, 136 (3B):B864–B871, 1964. 34

[19] W. Kohn and L. J. Sham. Self-Consistent Equations Including Exchange and Correlation Effects. *Phys. Rev.*, 140(4A):A1133–A1138, 1965. 34

[20] M. C. Payne, M. P. Teter, D. C. Allan, T. A. Arias, and J. D. Joannopoulos. Iterative minimization techniques for ab initio total-energy calculations: molecular dynamics and conjugate gradients. *Rev. Mod. Phys.*, 64(4):1045–1097, 1992. 34

[21] Leonard Kleinman and D. M. Bylander. Efficacious Form for Model Pseudopotentials. *Phys. Rev. Lett.*, 48(20):1425–1428, 1982. 34

[22] Loup Verlet. Computer "Experiments" on Classical Fluids. I. Thermodynamical Properties of Lennard-Jones Molecules. *Phys. Rev.*, 159(1):98–103, 1967. 34

[23] T. A. Arias, M. C. Payne, and J. D. Joannopoulos. *Ab Initio* molecular dynamics: Analytically continued energy functionals and insights into iterative solutions. *Phys. Rev. Lett.*, 69(7):1077–1080, 1992. 34

[24] E. de la Puente, A. Aguado, A. Ayuela, and J. M. López. Structural and electronic properties of small neutral $(MgO)_n$ clusters. *Phys. Rev. B*, 56(12): 7607–7614, 1997. 35

[25] Dario Alfè. Melting Curve of MgO from First-Principles Simulations. *Phys. Rev. Lett.*, 94(23):235701, 2005. 35

[26] Claudio Ronchi and Mikhail Sheindlin. Melting point of MgO. *J. Appl. Phys.*, 90(7):3325–3331, 2001. 35

[27] Douglas H. Lowndes, D. B. Geohegan, A. A. Puretzky, D. P. Norton, and C. M. Rouleau. Synthesis of Novel Thin-Film Materials by Pulsed Laser Deosition. *Science*, 273(5277):898–903, 1996. 35

CHAPTER 3

ELASTIC EFFECTS OF VACANCIES IN STRONTIUM TITANATE: SHORT- AND LONG-RANGE STRAIN FIELDS, ELASTIC DIPOLE TENSORS, AND CHEMICAL STRAIN

3.1 Introduction

Perovskites in general, and strontium titanate in particular, are some of the most frequently and exhaustively studied materials in solid-state physics and chemistry. This attention has largely derived from their diverse and interesting properties: high piezoelectricity[1], quantum paraelectricity[2, 3], ferroelectricity[4–7], uniaxial stress[8], and colossal magnetoresistance[9, 10]. Further, the cubic perovskites manifest intriguing effects of underlying quantum fluctuations, since, although they are comprised of relatively heavy atomic constituents, a number of competing structures are energetically and structurally similar[11]. Characterization of the low-temperature order parameters of these materials remains an open and engaging question[12].

Strontium titanate is a model perovskite — commonly available and reflective of many of the above properties of that material family. Specifically, while strontium titanate is a wide band-gap insulator at room temperature, it exhibits semiconductivity at elevated temperatures through doping or non-stoichiometric composition[13, 14] and superconductivity at low temperatures through reduction via addition of oxygen[15, 16]. The structural phase diagram of strontium titanate comprises a high-temperature cubic phase and a low-temperature tetragonal phase, with a transition temperature near 105 K[17–19]. The cubic perovskite structure is particularly interesting due to the richness of its phase diagram (nonpolar anti-

ferrodistortive to ferroelectric to antiferroelectric phases)[20, 21], to the capacity of these phases to emerge from miniscule deviations from the cubic lattice and its skeleton of octahedral oxygens (often through rigid rotations of such), and to open questions regarding the types (displacive or order-disorder) of the transitions among these phases[11].

Defects and vacancies play a particularly important role in the chemistry of perovskites and deserve continued study in strontium titanate due to the electronic and superconducting effects of doping as well as their role in the interface region of heterostructures[22]. In the dilute limit, the mechanics of defects are fully determined by an examination of stress-strain effects, in particular the elastic dipole tensor, which motivates this work's emphasis on such a quantity. Our presentation of both short-range displacements around a point defect as well as long-range effects (characterized by the elastic dipole tensor) allows for the calculation of x-ray scattering signatures. These quantities also enable the prediction of defect mechanics, such as the behavior of defects within an externally imposed strain gradient (as present in heterostructures), as well as the ratio of chemical strain to stoichiometric deviation (a direct experimental observable). Finally, through comparison of our predictions of chemical strain with experimental results, we draw a number of important conclusions regarding the nature of point defects in non-stoichiometric strontium titanate.

3.2 Background

Point defects introduce lattice distortions on both local and long-range scales. While the short-range distortions must be described by a potentially large set of

atomic displacements, the long-range *elastic* distortions may be completely described by a single tensor, the elastic dipole tensor[23].

The elastic dipole tensor and its relation to elastic effects may be understood by the following simple considerations. Consider to quadratic order the most general expansion of the free energy per unit volume of a crystal in terms of the strain ϵ_{ij} (i and j refer to coordinate axes) and the number of defects per unit volume n_d,

$$f\left(\epsilon_{ij}, n_d\right) = f_0 + n_d\, E_d + \tfrac{1}{2}\, n_d^2\, E_{dd} + \tfrac{1}{2} \sum_{ijkl} C_{ijkl}\, \epsilon_{ij}\, \epsilon_{kl} - n_d \sum_{ij} \epsilon_{ij}\, G_{ij}. \tag{3.1}$$

The Taylor expansion coefficients E_d, E_{dd}, C_{ijkl}, and G_{ij} are, respectively, the defect formation energy, an average inter-defect interaction energy, the components of the *elastic stiffness tensor* of the material, and the components of the *elastic dipole tensor* of the defects. The negative derivative of the free energy, (3.1), with respect to strain then gives the stress,

$$-\frac{\partial f}{\partial \epsilon_{ij}} \equiv \sigma_{ij} = -\sum_{kl} C_{ijkl}\, \epsilon_{kl} + n_d\, G_{ij}. \tag{3.2}$$

To isolate the elastic dipole tensor, we can consider the rate of change of the stress in the crystal per unit concentration of defects, while holding *strain fixed*, that is, under *strain control*. Although challenging experimentally, strain control is quite convenient computationally since it corresponds to performing calculations with fixed lattice vectors. This derivative thus gives the elastic dipole tensor $\mathbf{G}$ directly,

$$\left.\frac{\partial\, \sigma_{ij}}{\partial\, n_d}\right|_{\boldsymbol{\epsilon}} = G_{ij}, \tag{3.3}$$

so that *positive* diagonal components of $\mathbf{G}$ indicate that the presence of defects tends to *expand* the crystal along the corresponding directions.

Alternatively, we can also consider the derivative of the strain in the crystal per unit concentration of defects under *stress* or *load control* (holding stress fixed).

While stress control is computationally more complicated than strain control, it is the most common experimental situation. Under experimental conditions, the crystalline lattice vectors relax such that there is essentially zero stress (under normal laboratory conditions, atmospheric pressure corresponds to a negligible stress). This criteria allows the relation of strain to a newly defined quantity, $\mathbf{\Lambda}$,

$$\left.\frac{\partial\,\epsilon_{ij}}{\partial\,n_d}\right|_{\boldsymbol{\sigma}} = \sum_{kl} S_{ijkl}\,G_{kl} \;\equiv\; \Lambda_{ij}, \tag{3.4}$$

where $\mathbf{S}$, the *elastic compliance tensor*, is the inverse of the elastic stiffness tensor $\mathbf{C}$, and $\mathbf{\Lambda}$ is defined as the *defect-strain tensor*, which is the strain per unit defect concentration induced in a crystal at fixed stress.

Relying upon the above derivations, the numerical calculation of the elastic dipole tensor $\mathbf{G}$ is straightforward. We compute the stress induced with the introduction of a single defect in a supercell (maintaining fixed lattice vectors, but allowing relaxation of the atomic coordinates). From (3.3), this yields

$$\begin{aligned} G_{ij} &= \tfrac{1}{n_d}\left(\sigma_{ij}^{d} - \sigma_{ij}\right) \\ &= V_\circ\,\Delta\,\sigma_{ij}, \end{aligned} \tag{3.5}$$

where $\sigma^{\,d}$ and σ are the stress with and without the defect in the cell, respectively, and $V_\circ$ is the supercell volume. Once $\mathbf{G}$ is known, $\mathbf{\Lambda}$ may also be computed directly from (3.4). As a practical matter, we note that in this approach, the lattice vectors need not be those of a fully relaxed bulk crystal, provided the strain is small and kept fixed.

Experimental works often report the variations in *chemical strain*, the strain due to the presence of defects, with respect to stoichiometric deviations in the crystalline chemical formula. From the above considerations, the chemical strain is $\boldsymbol{\epsilon}_c \equiv n_d\mathbf{\Lambda}$. Deviations in stoichiometry specify the number of defects per chemical

unit, δ, so that, in this context, the concentration of defects per unit volume is $n_d = \delta/V_c$, where V_c is the volume of the chemical unit. These two relations then immediately provide the chemical strain as proportional to this *stoichiometric defect deviation*, δ,

$$\boldsymbol{\epsilon}_c = \left(\frac{\boldsymbol{\Lambda}}{V_c}\right)\delta. \tag{3.6}$$

Experimentally, one does not generally obtain a full tensor for $\boldsymbol{\epsilon}_c$ but, instead, an average over all equivalent defect orientations which restore the symmetry of the underlying crystal. In cubic crystals, one measures a scalar ϵ_c which corresponds to the mean diagonal component of $\boldsymbol{\epsilon}_c$.

Finally, we note that for the present case of cubic lattices, (3.4) reduces to a simpler form. For the diagonal elements,

$$\Lambda_{11} = \frac{1}{3}\left(\frac{2}{C_{11}-C12} + \frac{1}{C_{11}+2C12}\right)G_{11} + \frac{1}{3}\left(\frac{2}{C_{11}+2C12} - \frac{1}{C_{11}-C12}\right)(G_{22}+G_{33}), \tag{3.7}$$

with cyclic permutations giving the corresponding results for Λ_{22} and Λ_{33}. For the off-diagonal elements,

$$\Lambda_{12} = \frac{G_{12}}{C_{44}} \qquad (+ \text{ cycl. perm.}) \tag{3.8}$$

3.3 Methods

To simulate strontium titanate, we employ a shell-potential model[24] parameterized for strontium titanate[25]. Shell-potential models are formulated as an extension to ionic pair potentials and employed to capture the polarizability of the atomic constituents. The shell model separates each ion into two parts, a core and

an outer shell, which possess individual charges that sum to the nominal charge of the ion. The total model potential U consists of three terms,

$$U \equiv U_P + U_C + U_B, \tag{3.9}$$

representing, respectively, the polarizability of the ions, and the Coulomb and short-range interactions among the ions. The polarizability is captured by harmonic springs connecting the core and shell of each ion, so that U_P has the form,

$$U_P = \tfrac{1}{2} \sum_i k_i \left|\Delta r_i\right|^2, \tag{3.10}$$

where $|\Delta r_i|$ is the core-shell separation for ion i and the k_i are a set of ion-specific spring constants. The Coulomb contributions take the form,

$$U_C = \tfrac{1}{2} \sum_{i,j}{}' \frac{k_c q_i q_j}{r_{ij}}, \tag{3.11}$$

where i and j range over all cores and shells (excluding terms where i and j refer to the same ion), q_i and q_j are the corresponding charges, r_{ij} is the distance between the charge centers, and k_c is Coulomb's constant. We compute this Coulombic interaction[26] using a Particle Mesh Ewald algorithm[27–29] with all real-space pair-potential terms computed out to a fixed cutoff distance using neighbor tables. Finally, the short-range interactions are included through a sum of Buckingham[30] pair potentials (which can be viewed as combinations of Born-Mayer[31] and Lennard-Jones[32] potentials) of the form,

$$U_B = \tfrac{1}{2} \sum_{i,j} \left(A_{ij} e^{-r_{ij}/\rho_{ij}} - C_{ij} r_{ij}^{-6} \right), \tag{3.12}$$

where i and j range over *all shells* and A_{ij}, ρ_{ij}, and C_{ij} are pair-specific adjustable parameters. Here, the first term (Born-Mayer) serves as a repulsive short-range interaction to respect the Pauli exclusion principle, and the second term (Lennard-Jones) models the dispersion or van der Waals interactions[33]. The specific electrostatic and short-range shell-model parameters used in this study were fit to

strontium titanate by Akhtar et al.[25], with values as listed in Tables 3.1 and 3.2. Finally, we wish to emphasize again, as it is rarely mentioned explicitly in the shell-potential literature, that the pair-potential terms in U_B apply to the *shells only*, and *not* to the cores.

Shell models have been extensively used for decades as the primary empirical potential for modeling perovskites and other oxides[34, 35]. We tested the correctness of our coded implementation of this potential through comparisons of lattice constants and elastic moduli and find excellent agreement. For instance, using the same shell potential and ground-state structure, we predict a lattice constant for cubic strontium titanate of 3.881 Å, which is within 0.3% of the value calculated by Akhtar et al.[25] For the elastic moduli, we find $C_{11} = 306.9$ GPa, $C_{12} = 138.7$ GPa, and $C_{44} = 138.8$ GPa, which are within 1.8%, 1.0%, and 0.7%, respectively, of the values from Akhtar et al.[25] From this, we conclude that our implementation of the potential is correct.

As is well known, strontium titanate has a large number of similar, competing ground-state structures[20]. We should emphasize, at this point, that the main quantities of interest to this study, either local atomic displacements or the elastic dipole and defect-strain tensors (from (3.3), (3.4), and (3.5)), are all defined as defect-induced changes relative to the bulk structure, and so are likely quite insensitive to which of the competing structures are used to represent the bulk.

Accordingly, we have carried out what we regard as a thorough, but not exhaustive, search for a *probable* ground-state structure. Indeed, we have found no alternative structure which relaxes to an energy less than our candidate ground-state structure within our potential. We performed quenches on hundreds of random displacements from the idealized positions of the $1 \times 1 \times 1$ primitive unit cell

Table 3.1: Electrostatic shell-model potential parameters for strontium titanate (from Akhtar et al.[25]).

Ion	Shell Charge [e]	Core Charge [e]	Spring Constant $[\mathrm{eV} \cdot \mathrm{\AA}^{-2}]$
Sr^{2+}	1.526	0.474	11.406
Ti^{4+}	−35.863	39.863	65974.0
O^{2-}	−2.389	0.389	18.41

Table 3.2: Short-range shell-model potential parameters for strontium titanate (from Akhtar et al.[25]).

Interaction	A [eV]	ρ [Å]	C [eV $\cdot$ Å^6]
$Sr^{2+} \Leftrightarrow O^{2-}$	776.84	0.35867	0.0
$Ti^{4+} \Leftrightarrow O^{2-}$	877.20	0.38096	9.0
$O^{2-} \Leftrightarrow O^{2-}$	22764.3	0.1490	43.0

to explore various potential reconstructions for supercells up to $6 \times 6 \times 6$. We also considered a number of highly ordered, human-inspired configurations commensurate with the antiferrodistortive disordering that is observed experimentally[36, 37] and predicted theoretically[20, 38, 39]. Among those minima which we explored, we selected the lowest-energy configuration to serve as the bulk crystalline state throughout this study. This configuration possesses a fairly regular pattern, namely each oxygen octahedron rotates slightly along $\pm[111]$ (trigonal) directions in an alternating three-dimensional $2 \times 2 \times 2$ checkerboard pattern.

We investigated five defects in strontium titanate: the oxygen, strontium, and titanium vacancies, and the strontium-oxygen and titanium-oxygen divacancies. Since the octahedra rotations break the original crystalline symmetry and generate a set of different symmetry-related reconstructions, each of these five defects can be situated in multiple equivalent sites within each reconstruction.

Even well below room temperature, strontium titanate shows local fluctuations among the possible reconstructions. Thus, in addition to raw results for a specific realization of each defect in a given reconstruction, we also report results for each defect averaged over all possible reconstructions for a given orientation of the defect. The strontium and titanium vacancies do not select a specific direction and, thus, this averaging represents the full cubic crystalline symmetry group; their respective tensors therefore are always diagonal with cubic symmetry. The other defects do select specific crystalline directions, which must be specified when reporting the corresponding defect tensors. We thus reconstructionally average these latter defect tensors using either symmetry arguments or explicit calculations with different reconstructions, as appropriate. Finally, with a view to chemical strain measurements in macroscopic samples, we also report final averages over all

defect orientations.

In the case of the oxygen vacancy, the oxygen sits between two unique nearest-neighbor titanium atoms, thus uniquely distinguishing the Ti-V_O-Ti direction, which we define as [100], among the three cubic axes. Next, the titanium-oxygen divacancy selects a unique V_{Ti}-V_O direction, which we define as $[\bar{1}00]$, directed from the titanium site toward the oxygen site. Finally, the strontium-oxygen divacancy selects a unique V_{Sr}-V_O direction, which we define as $[1\bar{1}0]$, directed from the strontium toward the oxygen site. Once the reconstructional averaging is accomplished, the average over defect orientations requires generation of the crystal's response to all different possible orientations (three for the oxygen vacancies, six for the titanium-oxygen divacancy, and twelve for the strontium-oxygen divacancy) and restores full cubic symmetry.

To obtain the results in Section 3.4, each of these defects was placed within the bulk-reconstructed strontium titanate supercell, with cubic symmetry as experimentally observed for $T \gtrsim 105$ K[17–19], and then relaxed via the technique of preconditioned conjugate gradient minimization[40] (specifically, the Polak-Ribière[41] method) to find the minimal energy configuration (to within $\sim$1 μeV). Supercell convergence studies examined all five defects in cells containing up to 13 720 atoms and verified that such defects were sufficiently separated so that interactions across periodic supercell boundaries were negligible[42]. The final relaxed atomic configurations in the largest cells ($14 \times 14 \times 14$) provide the local strain fields which we report below for each defect. To determine the long-range strain fields, we compute the elastic dipole tensor $\mathbf{G}$ through the prescription described in (3.5) above; namely, we calculate the stress induced by the introduction of a single defect in the supercell, holding the lattice vectors fixed while allowing the atomic coordinates

to relax. (As a technical detail, we computed these stresses numerically as a finite difference on the total energy under changes in strain as in (3.2).)

3.4 Results

For a series of important and fundamental strontium titanate defects, we examine both the elastic dipole and defect-strain tensors, as introduced in Section 3.2, as well as the local strains surrounding each defect. This section first examines the role of the oxygen vacancy as a case study of a defect in strontium titanate. Subsequently, the results for the same set of studies are presented for four other point defects in strontium titanate: strontium and titanium vacancies and strontium-oxygen and titanium-oxygen divacancies. Section 3.5 continues with more general implications of our results.

3.4.1 Oxygen vacancy

As described above, there are three distinct orientations for the oxygen vacancy as defined by the Ti-V_O-Ti direction. Moreover, because of the reconstruction, there are in fact two distinct classes of site within each possible orientation. As one moves in the positive sense of direction along the Ti-V_O-Ti axis, these sites are distinguished by whether the rotation of the octahedra surrounding the two titanium sites changes from positive to negative or from negative to positive (in the right-hand sense about the +[111] direction). Below, we report results for the latter type of site.

We first examine the elastic dipole tensor computed according to (3.5). To

explore convergence, we compute the dipole tensor components in supercells of sizes $2 \times 2 \times 2$, $4 \times 4 \times 4$, ... , $14 \times 14 \times 14$, containing between 40 and 13 720 atoms with defect separations between $\sim$8 Å and $\sim$54 Å.

Specifically, we calculate the values of this tensor by means of the finite-difference method — namely, we introduce small strains ϵ_{ij} into each component of the lattice and measure the resultant changes in energy of the system: $G_{ij} = \Delta E/(2\epsilon_{ij})$. This method avoids the need to code explicit analytic derivatives of the energy with respect to strain, although it potentially introduces some error due to the disregard of terms higher than linear order. While smaller values of ϵ_{ij} obviously introduce smaller errors in the above expansion, such calculations suffer from numerical issues that necessitate the determination of the energies in the finite difference to much higher precision. Figure 3.1 presents the results from the introduction of various values of strain to compute the G_{11}-component in an $8 \times 8 \times 8$ supercell. We select a 1% value for strain as the best compromise between these competing issues and quantify the resulting error as less than 1% for all supercells. All system sizes and tensor components were similarly probed and confirmed to give less than 1% error for $\epsilon_{ij} = 0.01$.

Figure 3.2 depicts the convergence of the diagonal components of the elastic dipole tensor as a function of inverse linear dimension of the supercell. The linear behavior in the figure for large cells indicates that this quantity converges in the same way as the Coulomb interaction between defects and allows extrapolation of the fully converged value for these components in an infinite supercell. We observe exactly the same linear behavior with inverse linear dimension of cell for the convergence of the off-diagonal components of the dipole tensor. A linear fit to the data, for all tensor components for cell sizes in the range exhibiting linear

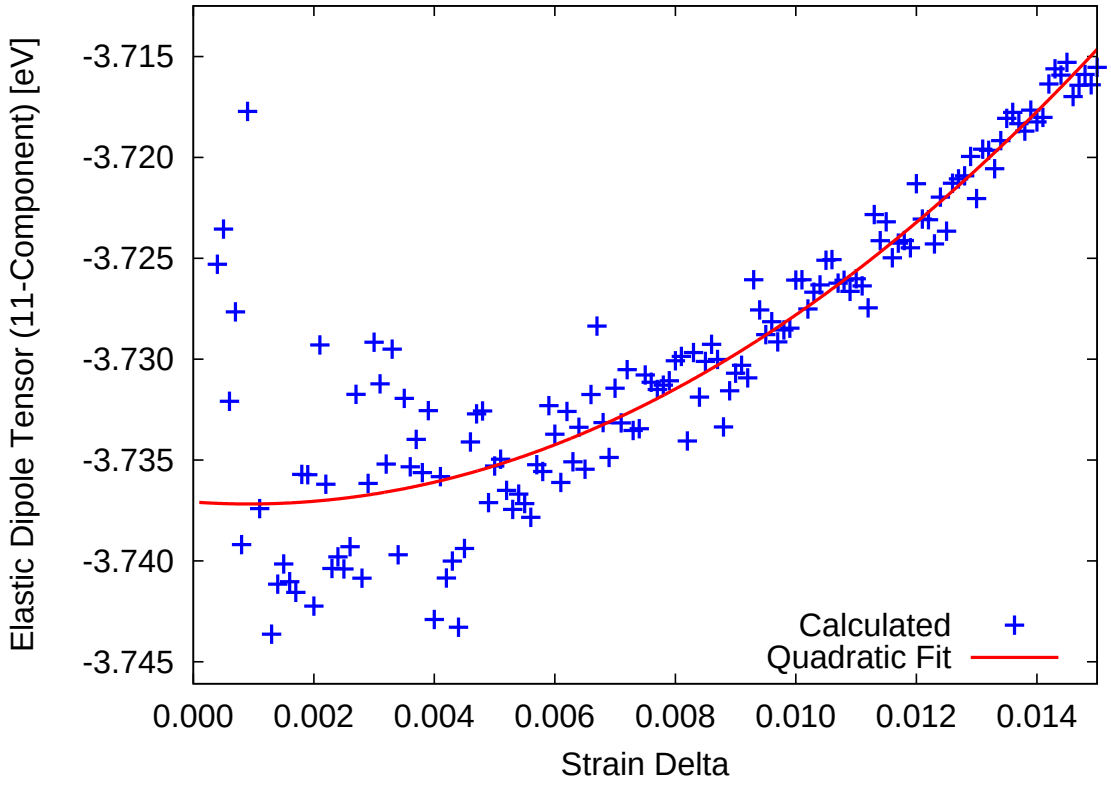

Figure 3.1: Centered finite-difference calculation of 11-component of elastic dipole tensor in $8 \times 8 \times 8$ supercell as a function of strain difference. Data illustrate the nature of finite-difference errors in computing elastic dipole tensor.

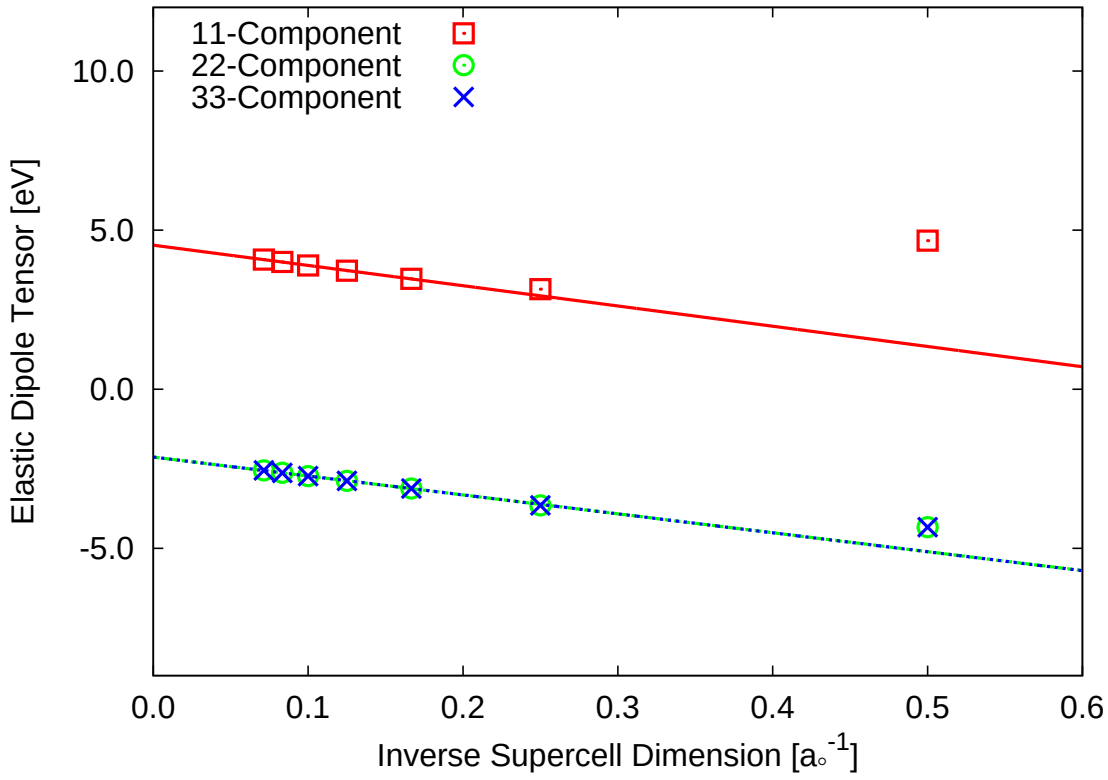

Figure 3.2: Diagonal components of elastic dipole tensor for oxygen vacancy in strontium titanate. Data show linear convergence with inverse linear dimension of supercell size.

behavior ($6\times6\times6$ through $14\times14\times14$), yields the elastic dipole tensor, *extrapolated to infinite cell size*, for this oxygen vacancy in strontium titanate,

$$\mathbf{G}_{\mathrm{O}} = \begin{pmatrix} 4.53 & -3.11 & -3.11 \\ -3.11 & -2.13 & 1.06 \\ -3.11 & 1.06 & -2.13 \end{pmatrix} \text{eV}.$$

As described above in Section 3.3, at finite temperatures ($T \gtrsim 105$ K), local fluctuations in the reconstruction make it appropriate to average this tensor over all reconstructions. The result is to eliminate the off-diagonal components, leaving the reconstructionally averaged elastic dipole tensor,

$$\overline{\mathbf{G}}_{\mathrm{O}} = \begin{pmatrix} 4.53 & 0.00 & 0.00 \\ 0.00 & -2.13 & 0.00 \\ 0.00 & 0.00 & -2.13 \end{pmatrix} \text{eV}.$$

Since the underlying, non-defected, crystal is now cubic, we can readily apply (3.7) and (3.8) and our *cubic* elastic stiffness tensor (elastic moduli) to $\overline{\mathbf{G}}_{\mathrm{O}}$ to obtain the reconstructionally averaged defect-strain tensor,

$$\overline{\mathbf{\Lambda}}_{\mathrm{O}} = \begin{pmatrix} 16.33 & 0.00 & 0.00 \\ 0.00 & -8.05 & 0.00 \\ 0.00 & 0.00 & -8.05 \end{pmatrix} \text{Å}^3.$$

The above results indicate that the oxygen vacancy tends to cause the crystal to expand along the Ti-V_O-Ti direction and to contract along the two orthogonal directions by an amount which results in negligible net volume change in the crystal. When the above tensor is averaged over all defect orientations (permutations of the three coordinate axes), the result is near perfect cancellation, resulting in a constant tensor (multiple of the identity) with a uniform chemical strain per unit defect concentration of $+0.07$ Å^3. This corresponds to a ratio of chemical strain

ϵ_c to the deviation from stoichiometry δ in $SrTiO_{3-\delta}$ of $\epsilon_c/\delta = +0.001$, indicating a *very slight* tendency for the crystal to expand due to the presence of oxygen vacancies.

Following Figure 3.3, we now examine the local strain of this system after reconstructional averaging. We note that the removal of the oxygen ion, with a nominal charge of -2, leaves an effective local positive environment in the location of the vacancy. We should expect pronounced Coulombic response to this environment in the form of local crystal polarization. Indeed, the nearest neighbors of the oxygen vacancy, the two titanium atoms, now move directly *away* from the vacancy on the precise vector connecting them, by 0.21 Å. The next-nearest neighbors are the eight oxygens comprised of two equidistant rings of four oxygens each, each of which move 0.21 Å *toward* the vacancy (0.19 Å along $\hat{e}_1$ with remaining projection of 0.08 Å either along $\hat{e}_2$ or $\hat{e}_3$ as dictated by symmetry), and one ring of four strontium atoms, each of which moves 0.10 Å directly *away* from the vacancy. The third shell of neighbors, a set of six oxygens, each one lattice constant away from the vacancy along the three lattice directions in the crystal, move different amounts depending upon the vector; the two oxygens along the Ti-V_O-Ti direction move 0.06 Å directly *away* from the vacancy (pushed sterically by the second-shell titanium atoms), while the other four oxygens move by a negligible amount (only 0.01 Å). While the fourth shell of neighbors, a set of eight titanium atoms at a distance $\sqrt{5}/2\, a_\circ$ from the vacancy, moves negligibly, the fifth shell of neighbors (sixteen oxygen and eight equidistant strontium atoms) shows significant movement in the strontium atoms of 0.15 Å *away* from the vacancy (0.08 Å along $\hat{e}_1$ with remaining projections of 0.09 Å along both $\hat{e}_2$ and $\hat{e}_3$), even though the oxygen atoms move a negligible amount. Finally, in the sixth shell of neighbors, a set of twelve oxygen atoms, eight oxygens (those not in the plane containing the defect

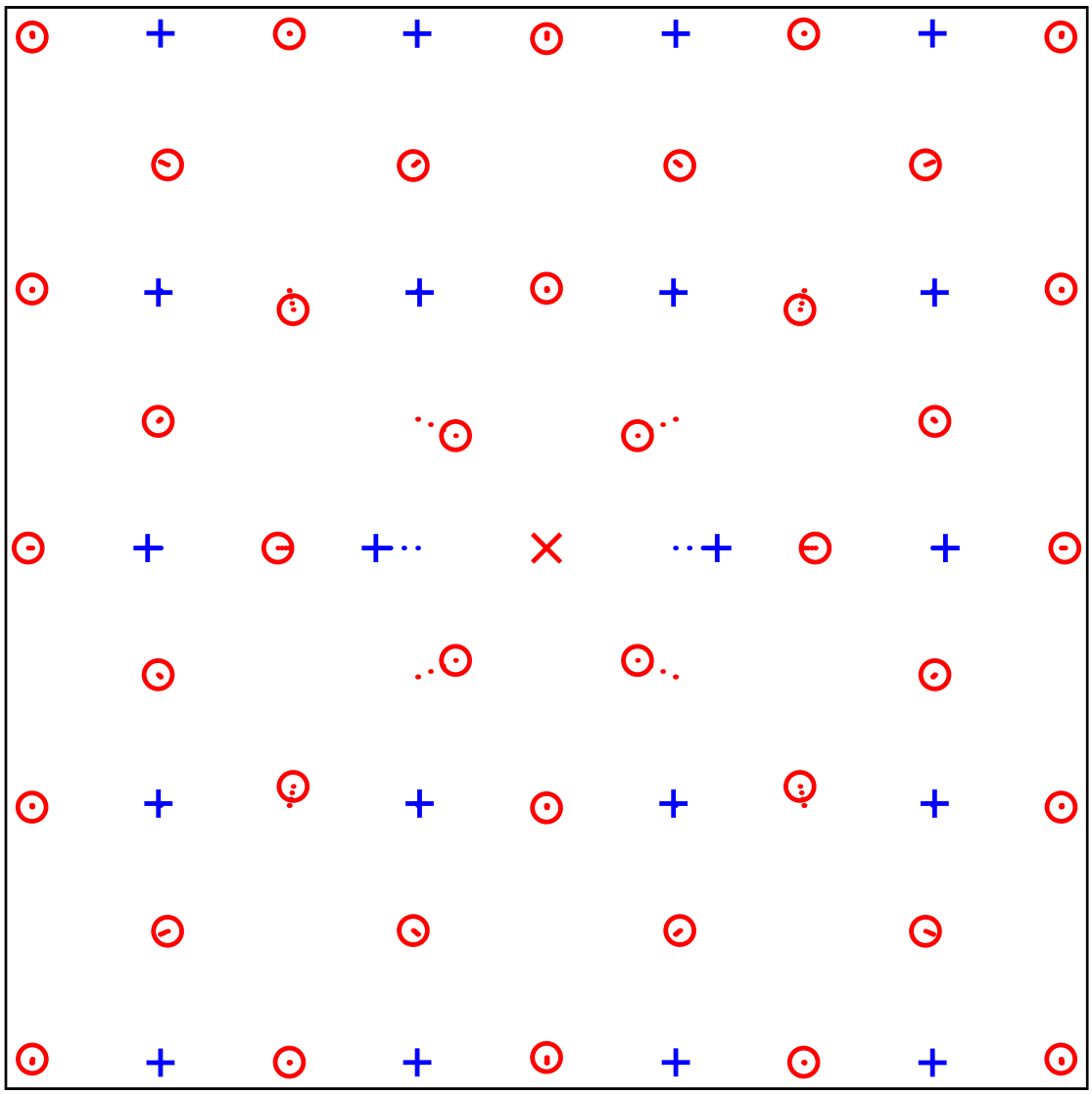

Figure 3.3: Local strain pattern for oxygen vacancy in the $\hat{e}_1\hat{e}_2$ plane of strontium titanate: titanium atoms ($+$), oxygen atoms ($\bigcirc$), oxygen vacancy ($\times$). Titanium displacements ($\cdots$) and oxygen displacements ($\cdots$) exaggerated by a factor of three for clarity.

and perpendicular to $\hat{e}_1$) move 0.10 Å *toward* the vacancy (0.02 Å along $\hat{e}_1$ with remaining projection of 0.10 Å either along $\hat{e}_2$ or $\hat{e}_3$ as dictated by the symmetry), while four others (those in the plane perpendicular to $\hat{e}_1$) move a negligible amount. All other atoms in the crystal move less than 0.06 Å.

Finally, we would like to comment on the relation between local strains and defect tensors. We observe that the direction of motion of the near-neighboring atoms often correlates with the far-field motion described by the defect-strain tensor. In this case, in the first and second shells, we see a general pattern of movement which is away from the defect along $\hat{e}_1$ and toward the defect in the other two directions, consistent with the signs in the long-range defect-strain tensor.

3.4.2 Strontium vacancy

We now repeat the above procedures to obtain similar results for the strontium vacancy. As described above, the strontium-vacancy site defines no unique direction and reconstructional averaging recovers the full cubic symmetry group. For any realization of the reconstruction there are in fact two distinct types of strontium sites. Each such site sits at the center of a cube with oxygen octahedra at the corners with alternating signs of rotations. The results reported below, prior to reconstructional averaging, correspond to the site in which the rotation at the [111] corner is positive.

For the elastic dipole tensor we find

$$\mathbf{G}_{\mathrm{Sr}} = \begin{pmatrix} 2.08 & -0.23 & -0.23 \\ -0.23 & 2.08 & -0.23 \\ -0.23 & -0.23 & 2.08 \end{pmatrix} \mathrm{eV},$$

where Figure 3.4 shows the convergence of the diagonal elements of the above tensor. Performing the reconstructional average gives

$$\overline{\mathbf{G}}_{\mathrm{Sr}} = \begin{pmatrix} 2.08 & 0.00 & 0.00 \\ 0.00 & 2.08 & 0.00 \\ 0.00 & 0.00 & 2.08 \end{pmatrix} \mathrm{eV},$$

with a corresponding defect-strain tensor,

$$\overline{\mathbf{\Lambda}}_{\mathrm{Sr}} = \begin{pmatrix} 1.78 & 0.00 & 0.00 \\ 0.00 & 1.78 & 0.00 \\ 0.00 & 0.00 & 1.78 \end{pmatrix} \mathrm{\AA}^3.$$

This result expresses the tendency of the crystal to expand due to the strontium vacancy, by an amount significantly greater than the net effect of the oxygen vacancy. Since the original defect defines no unique direction, no orientational averaging is necessary, and we find a ratio of chemical strain ϵ_c to the deviation from stoichiometry δ in $Sr_{1-\delta}TiO_3$ of $\epsilon_c/\delta = +0.030$, indicating a tendency for the crystal to expand due to the presence of strontium vacancies.

We now examine the local strains around such a strontium vacancy after reconstructional averaging (Figure 3.5). Twelve oxygen atoms (three in each of four neighboring octahedra) are nearest neighbors to the strontium vacancy; these twelve atoms all move directly *away* from the vacancy by a distance of 0.15 Å. The next-nearest neighbors are the eight titanium atoms in each of the surrounding octahedra, each of which moves 0.09 Å directly *toward* the strontium vacancy. All other atoms move less than 0.08 Å.

In this case, as expected, both the defect-strain tensor and the local strain displacements are symmetric after reconstructional averaging. The nearest-neighbor displacement shows an expansion in all directions, similar to the defect-strain

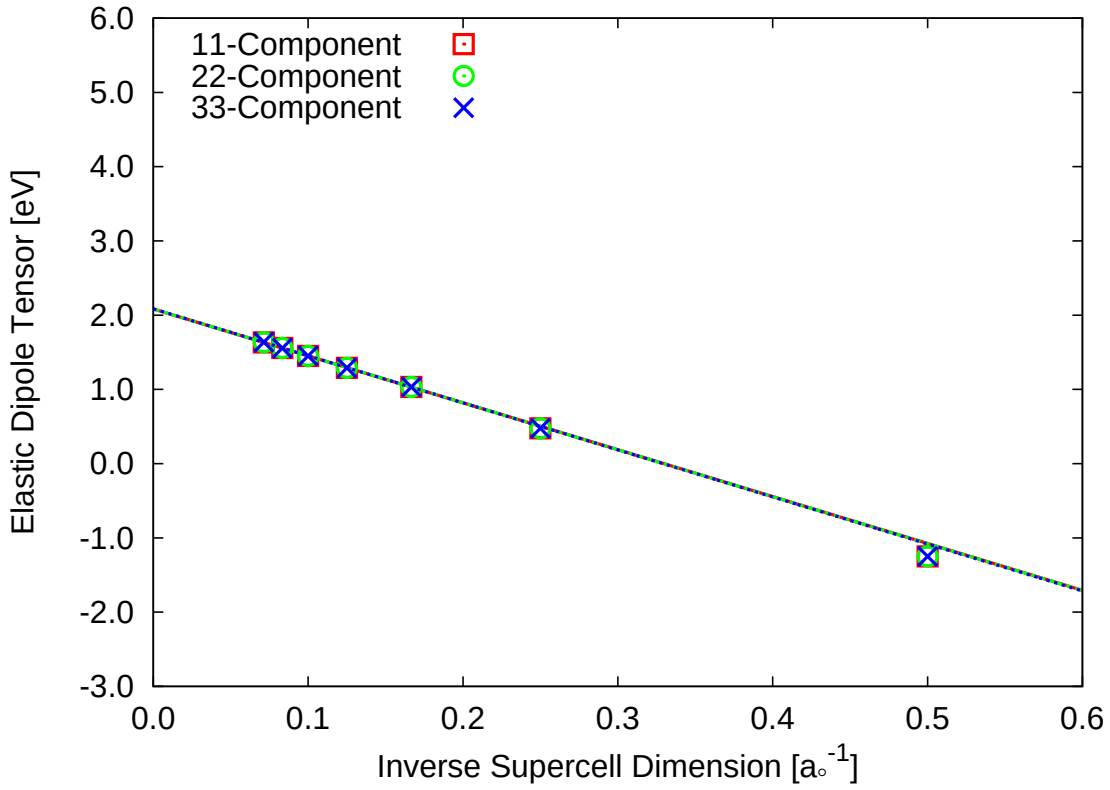

Figure 3.4: Diagonal components of elastic dipole tensor for strontium vacancy in strontium titanate. Data show linear convergence with inverse linear dimension of supercell size.

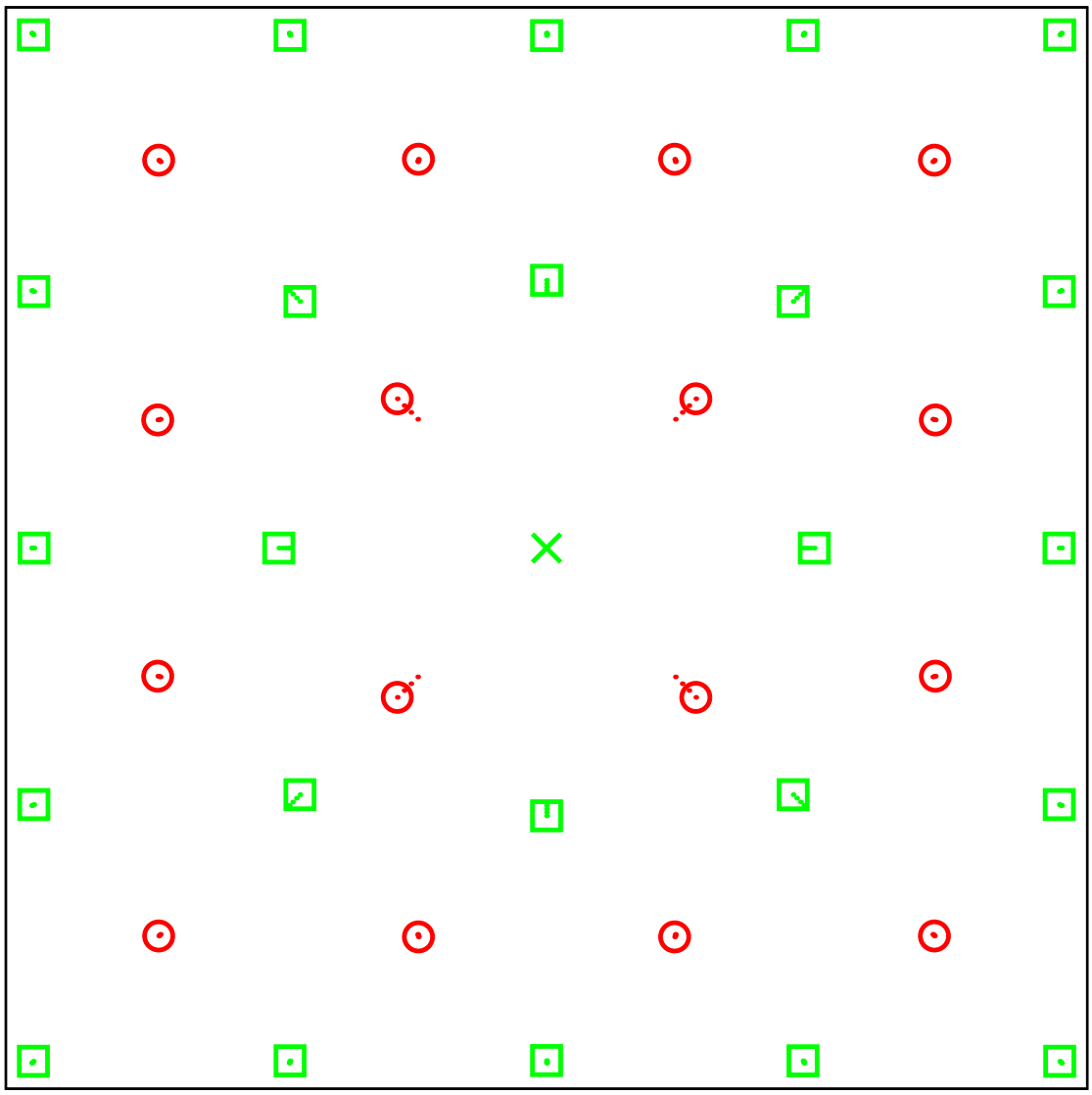

Figure 3.5: Local strain pattern for strontium vacancy in the $\hat{e}_1\hat{e}_2$ plane of strontium titanate: strontium atoms (□), oxygen atoms (○), strontium vacancy (×). Strontium displacements (· · ·) and oxygen displacements (· · ·) exaggerated by a factor of three for clarity.

tensor. The next-nearest neighbors, which have an opposite charge from that of the nearest neighbors, move in the opposite direction, reinforcing that there is no simple connection between local displacements and far-field strain patterns.

3.4.3 Titanium vacancy

The titanium-vacancy site also defines no unique direction in the ideal crystal, and the reconstructional averaging restores the full cubic symmetry. For any realization of the reconstruction there are, in fact, two distinct types of titanium site. Each such site sits at the center of an octahedra with either positive or negative signs of the rotations relative to the +[111] axis. The results reported below, prior to reconstructional averaging, correspond to the site in which the rotation is positive.

We first report our results for the elastic dipole tensor,

$$\mathbf{G}_{\mathrm{Ti}} = \begin{pmatrix} 28.08 & -0.70 & -0.70 \\ -0.70 & 28.08 & -0.70 \\ -0.70 & -0.70 & 28.08 \end{pmatrix} \mathrm{eV},$$

where Figure 3.6 shows the convergence of the diagonal elements of the above tensor. The reconstructional average is then

$$\overline{\mathbf{G}}_{\mathrm{Ti}} = \begin{pmatrix} 28.08 & 0.00 & 0.00 \\ 0.00 & 28.08 & 0.00 \\ 0.00 & 0.00 & 28.08 \end{pmatrix} \mathrm{eV},$$

with defect-strain tensor,

$$\overline{\mathbf{\Lambda}}_{\mathrm{Ti}} = \begin{pmatrix} 23.92 & 0.00 & 0.00 \\ 0.00 & 23.92 & 0.00 \\ 0.00 & 0.00 & 23.92 \end{pmatrix} \mathrm{\AA}^3.$$

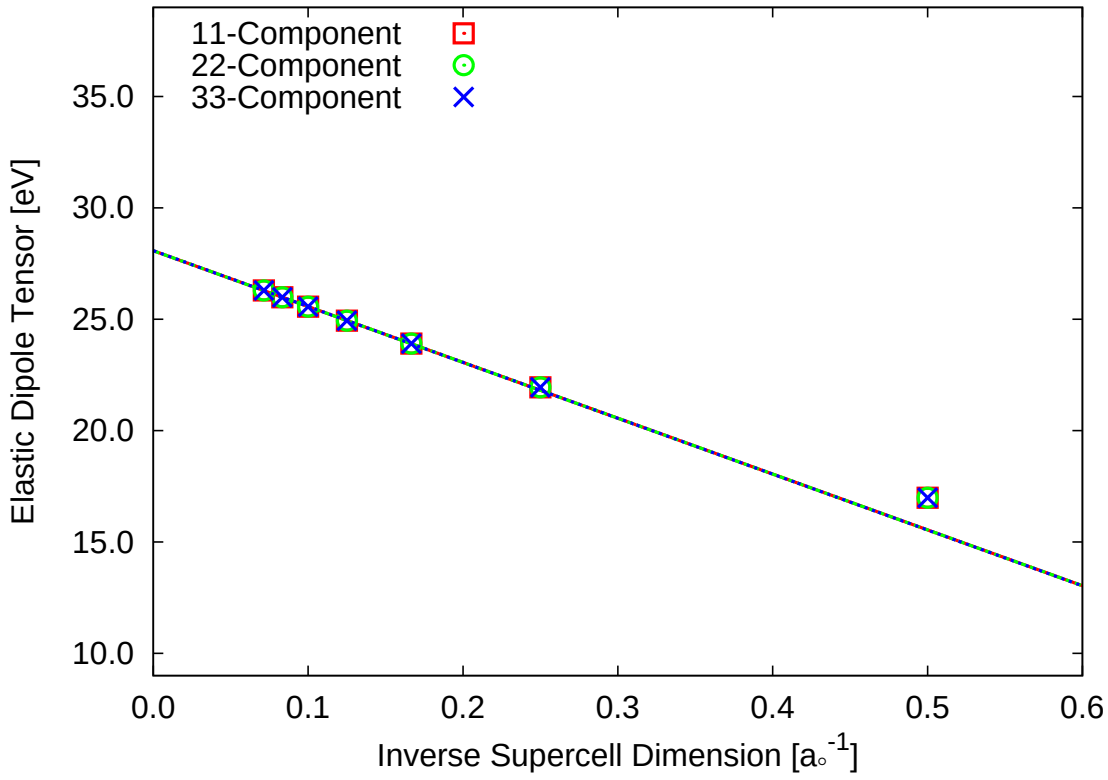

Figure 3.6: Diagonal components of elastic dipole tensor for titanium vacancy in strontium titanate. Data show linear convergence with inverse linear dimension of supercell size.

This defect-strain tensor expresses the tendency of the crystal to expand due to the titanium vacancy — a significantly greater amount even than that of the strontium. Again, since the original defect defines no unique direction, no orientational averaging over defect types is necessary. Finally, we report a ratio of chemical strain ϵ_c to the deviation from stoichiometry δ in $SrTi_{1-\delta}O_3$ of $\epsilon_c/\delta = +0.402$, indicating a significant tendency for the crystal to expand due to the presence of titanium vacancies.

As depicted in Figure 3.7, we now describe the local strain effects on the atoms surrounding the titanium vacancy: The nearest neighbors are six surrounding oxygen atoms which move 0.22 Å directly *away* from the titanium vacancy. The next-nearest neighbors are the eight surrounding strontium atoms along the body diagonals from the titanium vacancies; these strontium atoms move the very significant distance of 0.52 Å directly *toward* the titanium vacancy. The third shell is made up of six titanium atoms separated by a lattice constant from the vacancy along all three directions (positive and negative); all of these titanium atoms move 0.09 Å directly *away* from the titanium vacancy. Finally, the fourth shell of atoms is comprised of 24 oxygen atoms, arranged as six groups of four oxygens, each in a diamond-shape with its center one lattice coordinate away from the titanium vacancy in each lattice direction. These oxygens each move 0.08 Å *away* from the vacancy (0.08 Å along the vector separating the diamond-group from the vacancy, and 0.03 Å along either of the two other directions, so as to cause the diamond-group to spread outward). All other atoms in the crystal move less than 0.07 Å.

We again observe connections between the reconstructionally averaged local displacements and the far-field defect-strain tensor which have similar symmetry. In this case of the titanium vacancy, the nearest neighbor atoms are displaced

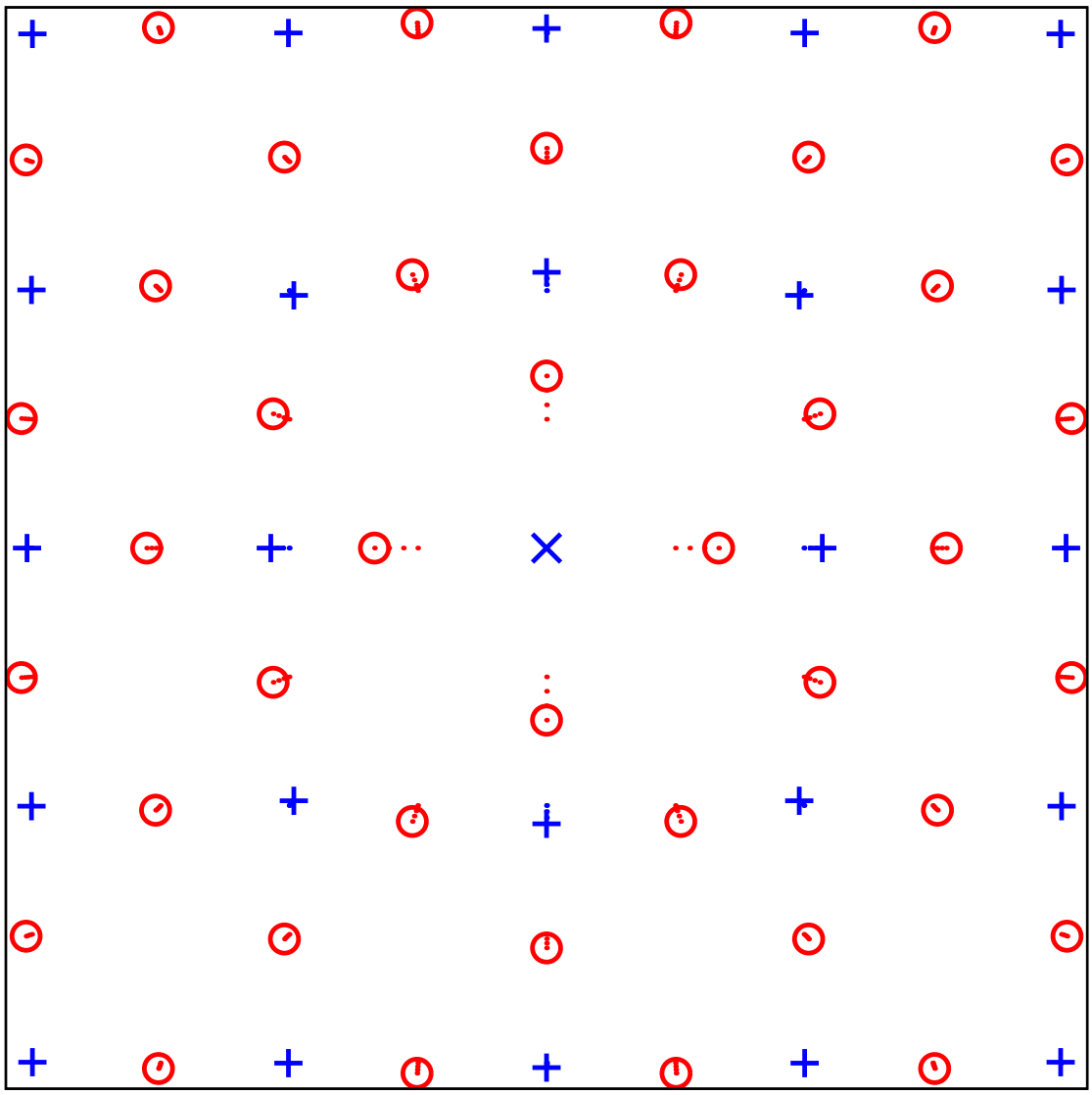

Figure 3.7: Local strain pattern for titanium vacancy in the $\hat{e}_1\hat{e}_2$ plane of strontium titanate: titanium atoms ($+$), oxygen atoms ($\bigcirc$), titanium vacancy ($\times$). Titanium displacements ($\cdots$) and oxygen displacements ($\cdots$) exaggerated by a factor of three for clarity.

away from the vacancy, showing the same behavior as the defect-strain tensor. Interestingly, however, the next-nearest neighbors, which move toward the titanium vacancy, actually have more than twice the displacement of the nearest neighbors. So here we observe that the far-field strain does not correlate with the largest magnitude displacement, but instead with that of the nearest-neighbor atoms.

3.4.4 Strontium-oxygen divacancy

As described above in Section 3.3, there are twelve distinct orientations for the strontium-oxygen divacancy as defined by the V_{Sr}-V_O direction. For any realization of the reconstruction there are in fact two distinct types of strontium-oxygen sites. Each such strontium site sits at the center of a cube with oxygen octahedra at the corners with alternating signs of rotations. The results reported below, prior to reconstructional averaging, correspond to the $[1\bar{1}0]$ defect with negative sense of rotation for the octahedron at the [111] corner.

The elastic dipole tensor for this defect is

$$\mathbf{G}_{\mathrm{SrO}} = \begin{pmatrix} -4.62 & 3.00 & -2.28 \\ 3.00 & -4.62 & -2.28 \\ -2.28 & -2.28 & 6.95 \end{pmatrix} \mathrm{eV},$$

where Figure 3.8 shows the convergence of the diagonal elements of the above tensor. The reconstructional average is then

$$\overline{\mathbf{G}}_{\mathrm{SrO}} = \begin{pmatrix} -3.00 & 1.78 & 0.00 \\ 1.78 & -3.00 & 0.00 \\ 0.00 & 0.00 & 4.27 \end{pmatrix} \mathrm{eV},$$

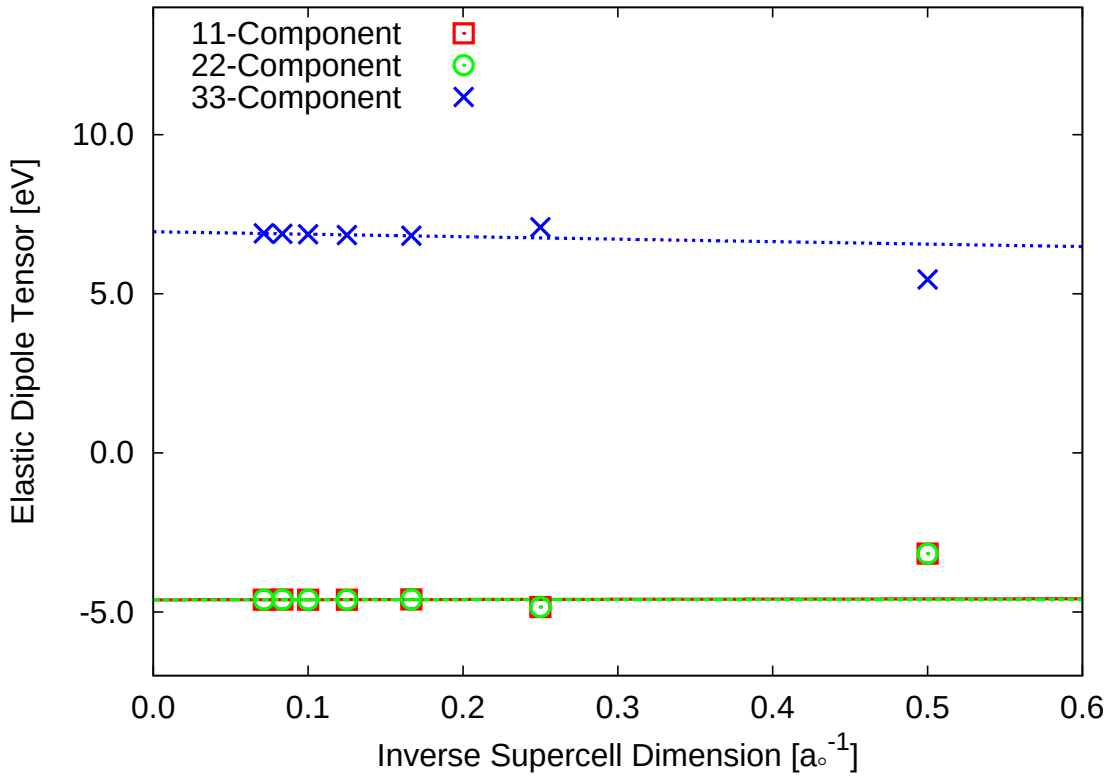

Figure 3.8: Diagonal components of elastic dipole tensor for strontium-oxygen divacancy in strontium titanate. Data show linear convergence with inverse linear dimension of supercell size.

with defect-strain tensor,

$$\overline{\mathbf{\Lambda}}_{\mathrm{SrO}} = \begin{pmatrix} -9.37 & 2.14 & 0.00 \\ 2.14 & -9.37 & 0.00 \\ 0.00 & 0.00 & 17.25 \end{pmatrix} \text{Å}^3.$$

This defect-strain tensor expresses a slight tendency of the crystal to contract due to the strontium-oxygen divacancy. The lower symmetry of this defect, with its orientation along a diagonal, leads to remaining off-diagonal elements even after reconstructional averaging. However, when the above tensor is averaged over all twelve defect orientations, the result is a constant tensor with a uniform chemical strain per unit concentration of defect of -0.50 Å^3. This corresponds to a ratio of chemical strain ϵ_c to the deviation from stoichiometry δ in $\mathrm{Sr}_{1-\delta}\mathrm{TiO}_{3-\delta}$ of $\epsilon_c/\delta = -0.008$, indicating a tendency for the crystal to contract due to the presence of strontium-oxygen divacancies.

Referring to Figure 3.9, we now examine the local displacements after reconstructional averaging. The situation with this divacancy is more complicated than that of earlier isolated atomic vacancies, leading us to characterize the atomic displacements with respect to each independent missing atom in the strontium-oxygen divacancy. The first shell is comprised of the eleven remaining oxygen atoms that are nearest neighbors of the strontium vacancy. This strontium vacancy would normally have twelve neighboring oxygen atoms forming three squares in the three planes, each comprised of four atoms centered around the strontium vacancy; however, one of these oxygen atoms is missing to form the divacancy. The four oxygens, which are farthest from the oxygen vacancy but not in the same square as the oxygen vacancy, all move *away* from the strontium vacancy by 0.14 Å (0.10 Å along $\hat{e}_3$, and 0.09 Å along either $\hat{e}_1$ or $\hat{e}_2$, depending upon symmetry, with 0.004 Å along the opposite vector, chosen such that most of the displacement is within the plane

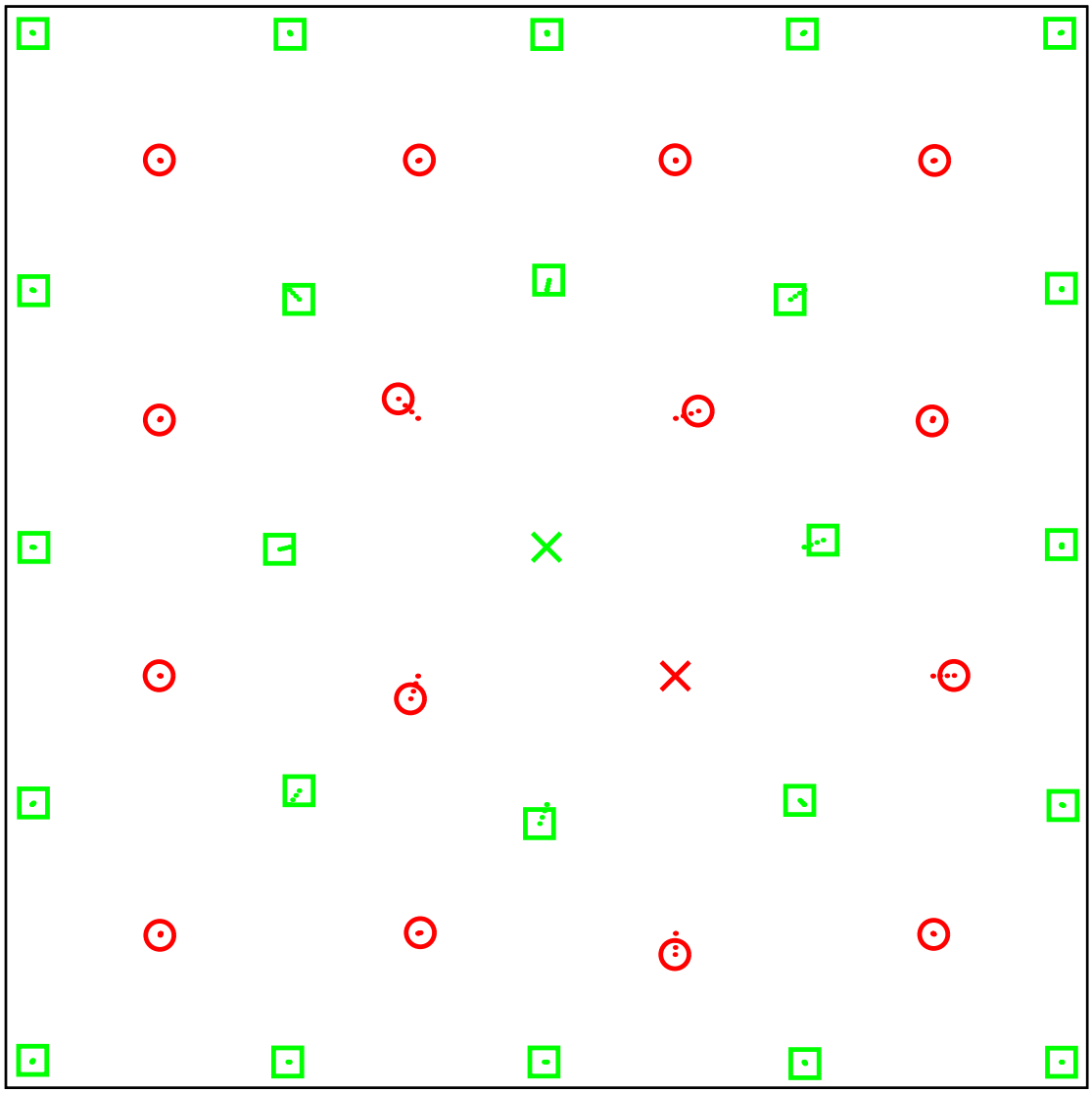

Figure 3.9: Local strain pattern for strontium-oxygen divacancy in the $\hat{e}_1\hat{e}_2$ plane of strontium titanate: strontium atoms (□), oxygen atoms (○), strontium vacancy (×), oxygen vacancy (×). Strontium displacements (···) and oxygen displacements (···) exaggerated by a factor of three for clarity.

of squares to which that oxygen belongs). The four oxygens that are closest to the oxygen vacancy and still not in the same square as the oxygen vacancy also move as a group. These oxygen atoms all move *away* from the strontium vacancy by 0.11 Å (0.05 Å along $\hat{e}_3$, and 0.09 Å along either $\hat{e}_1$ or $\hat{e}_2$, depending upon symmetry, with 0.05 Å along the opposite vector, chosen such that more of the displacement is within the plane of the square to which that oxygen belongs). The two oxygens, in the same square as the oxygen vacancy and closer to such vacancy, are displaced *away* from the defect, in that plane, by 0.12 Å (0.12 Å along either $\hat{e}_1$ or $\hat{e}_2$, and 0.04 Å along the opposite vector, chosen to ensure that the displacement maximizes its overall movement away from the remaining oxygen in this square). The final oxygen atom is also in the same square as the oxygen vacancy, but is the farthest atom from the vacancy in this square; it is displaced directly *away* from the defect in that plane by 0.14 Å. Also included in the first shell are the remaining oxygen atoms that are nearest neighbors to the missing oxygen vacancy. That oxygen vacancy, part of two oxygen octahedra, has eight neighboring oxygens, four in each octahedron; of those eight oxygens, the four closest to the strontium vacancy have already been considered as part of the nearest neighbors to the missing strontium atom. The remaining four oxygen atoms in the other octahedron, farthest from the strontium vacancy, move the appreciable distance of 0.33 Å *toward* the vector connecting the strontium and oxygen vacancies (0.30 Å along $\hat{e}_3$ and 0.11 Å along either $\hat{e}_1$ or $\hat{e}_2$, depending upon symmetry, with 0.005 Å along the opposite vector, chosen such that most of the displacement in the $\hat{e}_1\hat{e}_2$ plane is toward the oxygen vacancy). Finally, this first shell also includes the three strontium atoms (the fourth is itself missing) nearest the oxygen vacancy. The one strontium atom farthest from the strontium vacancy moves directly *toward* the oxygen vacancy by 0.03 Å (0.02 Å along both $\hat{e}_1$ and $\hat{e}_2$). The other two strontium

atoms move *away* from the oxygen vacancy by 0.10 Å (0.10 Å along either $\hat{e}_1$ or $\hat{e}_2$, depending upon symmetry, with 0.04 Å along the opposite vector, chosen such that the displacement maximizes the distances of these strontium atoms from the strontium vacancy).

The second shell is comprised of the eight titanium atoms that are the nearest neighbors to the missing strontium atom. Two of these nearest neighboring titanium atoms, which could alternatively have been categorized as the nearest-neighboring shell of atoms from the oxygen vacancy, move *away* from the strontium vacancy (as well as the oxygen vacancy) by 0.19 Å (0.19 Å away from the vacancies along $\hat{e}_3$, and 0.03 Å toward the strontium vacancy along both $\hat{e}_1$ and $\hat{e}_2$). Two other nearest-neighbor titanium atoms, those that are furthest from the oxygen vacancy amongst these eight titanium atoms, move 0.09 Å *toward* the strontium vacancy (0.06 Å along $\hat{e}_3$, and 0.05 Å along both $\hat{e}_1$ and $\hat{e}_2$). The final four of these eight nearest-neighbor titanium atoms move *toward* the vacancies by 0.11 Å (0.05 Å along $\hat{e}_3$ and 0.08 Å along either $\hat{e}_1$ or $\hat{e}_2$, depending upon symmetry, with 0.05 Å along the opposite vector, chosen such that more of the displacement in the $\hat{e}_1\hat{e}_2$ plane is toward the oxygen vacancy). All other atoms move less than 0.17 Å.

We now investigate correlations between these above reconstructionally averaged local displacements and the far-field defect-strain tensor. We find surprising results in this case of the strontium-oxygen divacancy. While the defect-strain tensor and local displacement pattern both show expansion on the [001] axis outward from the defect, we see a disagreement in sign in the (001) plane between the far-field contraction and the expansion of the nearest neighbors. This serves as a cautionary note that far-field and near-field strain patterns need not be simply related and reinforces the importance of providing both sets of information for

further experimental analysis of x-ray scattering signatures.

3.4.5 Titanium-oxygen divacancy

As described above in Section 3.3, there are six distinct orientations for the titanium-oxygen divacancy as defined by the V_{Ti}-V_O direction. Moreover, because of the reconstruction, there are in fact two distinct classes of sites within each possible orientation, as distinguished by the rotation state of the octahedron in which the titanium sits. Below, we report results for a $[\bar{1}00]$ defect with the titanium sitting in an octahedron of positive rotation.

The elastic dipole tensor for this defect is

$$\mathbf{G}_{\mathrm{TiO}} = \begin{pmatrix} 14.74 & -0.08 & -4.76 \\ -0.08 & 18.13 & -3.87 \\ -4.76 & -3.87 & 21.56 \end{pmatrix} \mathrm{eV},$$

where Figure 3.10 shows the convergence of the diagonal elements of the above tensor. The reconstructional average gives

$$\overline{\mathbf{G}}_{\mathrm{TiO}} = \begin{pmatrix} 14.74 & 0.00 & 0.00 \\ 0.00 & 19.84 & 0.00 \\ 0.00 & 0.00 & 19.84 \end{pmatrix} \mathrm{eV},$$

with corresponding defect-strain tensor,

$$\overline{\mathbf{\Lambda}}_{\mathrm{TiO}} = \begin{pmatrix} 3.00 & 0.00 & 0.00 \\ 0.00 & 21.68 & 0.00 \\ 0.00 & 0.00 & 21.68 \end{pmatrix} \mathrm{\AA}^3.$$

The defect-strain tensor expresses the tendency of this defect to expand the crystal in all directions, but primarily along the directions orthogonal to the V_{Ti}-V_O axis.

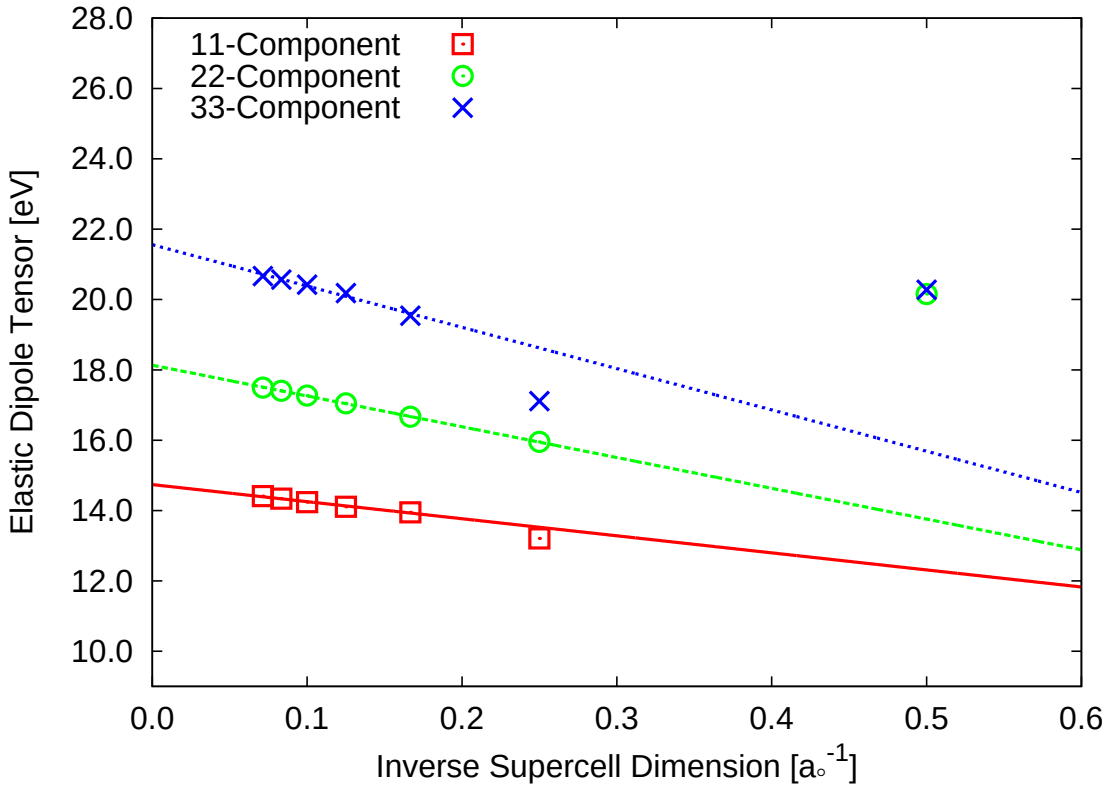

Figure 3.10: Diagonal components of elastic dipole tensor for titanium-oxygen divacancy in strontium titanate. Data show linear convergence with inverse linear dimension of supercell size.

When the above tensor is averaged over all six defect orientations (oxygen sites in octahedra surrounding the central titanium site, recalling that the V_{Ti}-V_O axis is direction dependent), the result is a constant tensor with a uniform chemical strain per unit concentration of defect of +15.45 Å^3. Such expansion corresponds to a ratio of chemical strain ϵ_c to the deviation from stoichiometry δ in $SrTi_{1-\delta}O_{3-\delta}$ of $\epsilon_c/\delta = +0.260$, indicating a significant tendency for the crystal to expand due to the presence of titanium-oxygen divacancy.

Now that our reconstructional averaging has symmetrized the displacement patterns of neighboring atoms, it is instructive to examine this set of near-field atomic strains, shown in Figure 3.11. The situation with this divacancy is again more complicated than that of earlier isolated atomic vacancies. There are six atoms in the first shell around the divacancy. The five remaining (the sixth is itself missing) oxygen atoms that are nearest neighbors of the titanium vacancy all move *away* from that vacancy: the one that is furthest from the oxygen vacancy moves 0.20 Å directly *away* from the vacancy, while the other four (which are in the $\hat{e}_2\hat{e}_3$ plane) move 0.23 Å *away* from the vacancy (0.13 Å along $\hat{e}_1$ toward the oxygen vacancy with the remaining projection of 0.19 Å away from the divacancy either along $\hat{e}_2$ or $\hat{e}_3$ as dictated by the symmetry). The sixth atom in this first shell is the sole titanium atom that is the nearest neighbor to the oxygen vacancy; it moves directly *away* from the vacancy by 0.13 Å. In the second shell, we identify four of the oxygen atoms that are nearest neighbor to the oxygen vacancy (we already counted the other four nearest-neighbor oxygens above, "assigning" them to the titanium vacancy); these oxygens move 0.33 Å *toward* the oxygen vacancy (0.31 Å along $\hat{e}_1$ with remaining projection of 0.10 Å either along $\hat{e}_2$ or $\hat{e}_3$ as dictated by symmetry). Also, in this second shell, we can loosely consider the eight nearest-neighbor strontium atoms to the titanium vacancy, all of which move toward the

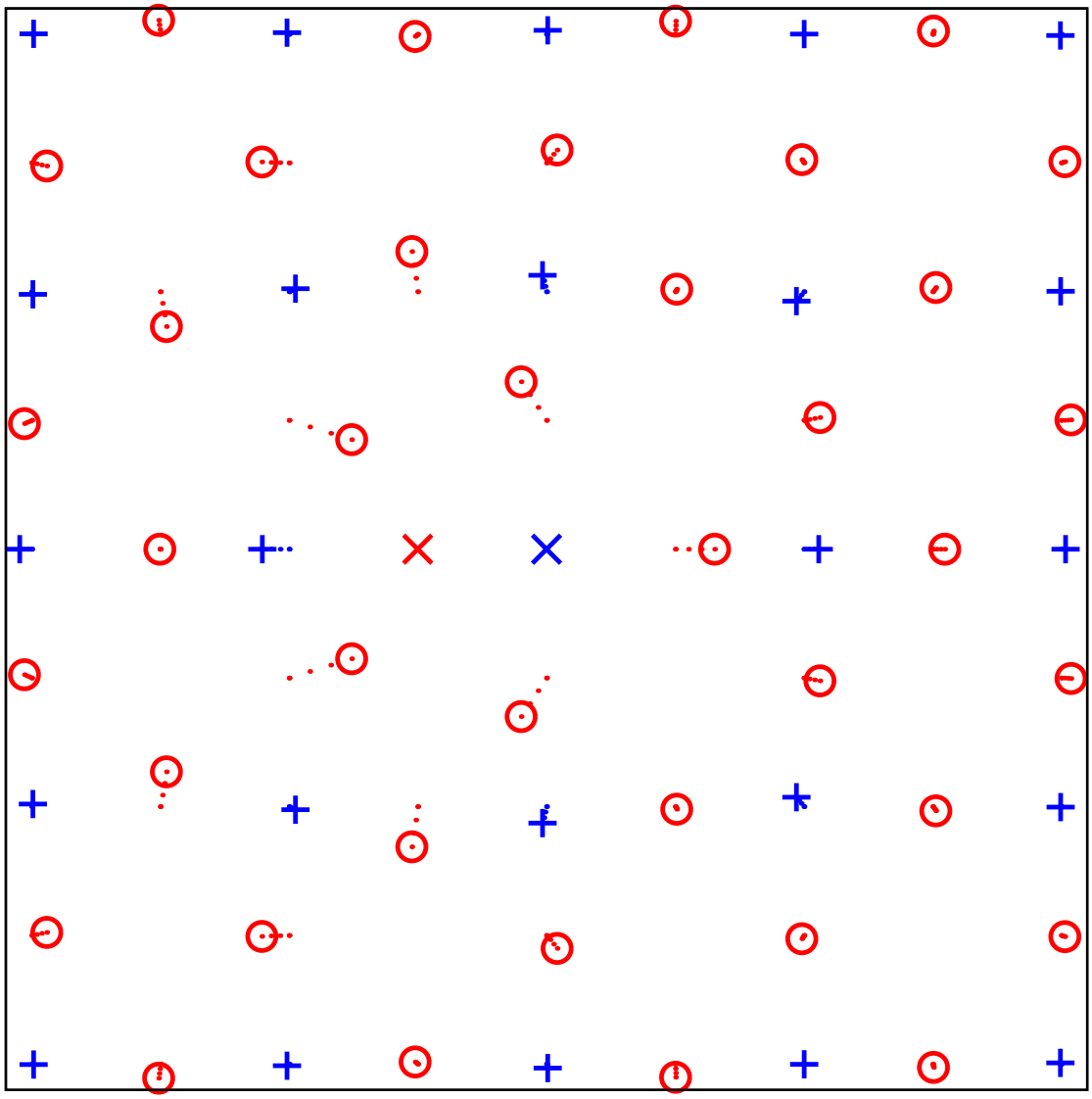

Figure 3.11: Local strain pattern for titanium-oxygen divacancy in the $\hat{e}_1\hat{e}_2$ plane of strontium titanate: titanium atoms ($+$), oxygen atoms ($\bigcirc$), titanium vacancy ($\times$), oxygen vacancy ($\times$). Titanium displacements ($\cdots$) and oxygen displacements ($\cdots$) exaggerated by a factor of three for clarity.

titanium vacancy: four of these strontium atoms are in a plane that includes the oxygen vacancy, and these move 0.22 Å *toward* the titanium vacancy (0.17 Å along $\hat{e}_1$ and 0.09 Å along both $\hat{e}_2$ and $\hat{e}_3$); the other four strontium atoms are on the opposite side of the titanium vacancy, and these move significantly *toward* the vacancy by 0.58 Å (0.38 Å along $\hat{e}_1$ and 0.31 Å along both $\hat{e}_2$ and $\hat{e}_3$). All other atoms move less than 0.20 Å.

We again examine connections between the reconstructionally averaged local displacements and the far-field defect-strain tensor. In this case of the titanium-oxygen divacancy, the nearest-neighbor atoms to both vacancies move outward, showing the same behavior as the defect-strain tensor. These atoms also demonstrate larger movements in those directions orthogonal to the V_{Ti}-V_O axis, which conforms with the far-field tensor. The next-nearest neighbors to both vacancies move inward with significant displacements, with those closest to the titanium vacancy moving by almost three times the amount that the nearest-neighbor atoms move. So here we note once more that the far-field strain does not appear to correlate with the largest magnitude displacement, but instead with that of the nearest-neighbor atoms.

3.5 Discussion

The above results for the local strain patterns and detailed defect tensors are now available for direct comparison to diffuse x-ray measurements; however, we are not aware of any such x-ray data to date. Nonetheless, the fully averaged (over both reconstructions and orientations) defect-strain tensors relate directly to measurements which are commonly done of chemical strain as a function of

defect concentration. Table 3.3 summaries the results from Section 3.4 for the ratios of chemical strain ϵ_c to stoichiometric defect deviation δ for all of the defects considered in this study.

Oxygen-vacancy concentration is widely thought to serve a crucial role in the properties of perovskites[43–50], is readily varied but difficult to control[51, 52], and is experimentally observed to affect chemical strain[53]. Moreover, cation stoichiometry is also difficult to control[54, 55] and so it is uncertain whether, as oxygen vacancies are introduced into the crystal, such vacancies bind to cation vacancies or form in isolation. In the former case, where the oxygen vacancies eventually bind to preexisting cation vacancies, the reference configuration should be the crystal containing the cation vacancy. Hence, it is the *difference* between the chemical strain of the oxygen-cation divacancy and that of the isolated cation vacancy that describes the change in the crystal lattice as a function of varying oxygen-vacancy concentration. In the latter case of isolated vacancies, the bulk crystal is in fact the system into which these vacancies are introduced, and thus the chemical strain as a function of oxygen-vacancy concentration is described precisely by that of the isolated oxygen vacancy in our study. Table 3.4 summarizes the resulting *net* chemical strain $\Delta\epsilon_c$ versus oxygen-vacancy concentration δ.

For the oxygen vacancy, we have the intriguing result that the elastic dipole tensor and corresponding defect-strain tensor almost vanish under orientational averaging. Thus, very little net effect on the lattice can be expected from the presence of isolated oxygen vacancies. Moreover, the large anisotropy of the dipole tensor of the oxygen vacancy and the ease of introduction and high mobility of such vacancies should allow for the control of the population and orientation of oxygen vacancies by applying external stress. (For instance, at 1% strain, the

Table 3.3: Individual ratios of chemical strain ϵ_c to stoichiometric defect deviation δ for different defects as calculated in Section 3.4.

Defect	ϵ_c/δ
V_O	0.001
V_{Sr}	0.030
V_{Ti}	0.402
V_{SrO}	−0.008
V_{TiO}	0.260

Table 3.4: Net ratios of chemical strains to stoichiometric defect deviation for oxygen vacancies, referenced against bulk and isolated cation vacancies as appropriate.

Reference state	$\Delta\epsilon_c/\delta$
Bulk	0.001
V_{Sr}	−0.038
V_{Ti}	−0.142

orientational energy differences from $\overline{\mathbf{G}}_{\mathrm{O}}$ are 66 meV, or about 2.6 times room temperature.) Also, such vacancies can be expected to tend to shield internal crystalline stresses that result from materials processing, a fact potentially related to the observed difficulties in controlling the oxygen-vacancy concentration during crystalline growth.

One of the earliest sets of available experimental data on chemical strain due to oxygen vacancies in strontium titanate comes from Yamada and Miller[53], who unfortunately found a null result. Nonetheless, that null result places bounds which, in conjunction with our results, allow some conclusions to be drawn. Yamada and Miller varied the oxygen-vacancy concentration over a range from nearly zero up to 3.24×10^{19} cm^{-3} ($\delta = 0.0019$ in $SrTiO_{3-\delta}$), stating that "no volume change upon reduction was assumed," due to the experimental uncertainty of the lattice constant ($\Delta a = 5 \times 10^{-4}$ Å) in their x-ray diffraction measurements. Their detection limit for chemical strain per stoichiometric defect deviation is therefore $|\epsilon_c/\delta| = |(\Delta a/a)/\delta| < 0.066$, where a is the cubic lattice constant. From Table 3.4, it is evident that this bound is consistent with either isolated oxygen vacancies or strontium-oxygen divacancies, but is inconsistent with titanium-oxygen divacancies.

The literature also presents studies of chemical strain due to *cation* non-stoichiometry. Ohnishi et al. present experimental results on the ratio of chemical strain to deviation from cation stoichiometry[56]. Specifically, they measure the lattice changes for both strontium-rich and strontium-poor strontium titanate. They associate the strontium-rich phase with creation of Ruddlesden–Popper[57, 58] planar faults (extra SrO layers) and the strontium-poor regime with the presence of strontium vacancies, possibly bound into strontium-oxygen divacancies. A least-

squares fit to the results of Ohnishi and coworkers provides a value for ϵ_c/δ between +0.13 (non-weighted) and +0.14 (weighted by reported experimental uncertainty) for the strontium-rich phase ($Sr_{1+\delta}TiO_3$) and between +0.5 (non-weighted) and +0.8 (weighted by reported experimental uncertainty) for the strontium-poor phase ($Sr_{1-\delta}TiO_3$).

Our calculations of titanium-vacancy chemical strains are not directly relevant to the strontium-rich phase because they do not account for Ruddlesden–Popper planar faults. On the other hand, our results for strontium vacancies, under Ohnishi and coworkers' interpretation, should be directly relevant to their strontium-poor samples. Table 3.3 gives $\epsilon_c/\delta = +0.030$ and $\epsilon_c/\delta = -0.008$, respectively, for isolated strontium vacancies and bound strontium-oxygen divacancies. However, both of these are an order of magnitude smaller than the observed chemical strain. (We note parenthetically that, while our calculations reflect chemical strains for isolated defects and Ohnishi and coworkers measure strains for relatively high defect densities, Figures 3.4 and 3.8 show that trends in our data with increasing defect concentration only tend to reinforce our conclusions.) We remark that our results are consistent with the observation that, within a given structural class, the lattice constants of the titanates are largely insensitive to the nature of the A-site cations. (See data on $A^{2+}B^{4+}O_3$ perovskites compiled by Galasso[59].) From both the results of our calculations and this general observation, it seems implausible that simple A-site vacancies should produce the measured magnitude of chemical strain. Chemical strains of the magnitude measured by Ohnishi and coworkers more plausibly arise from B-site vacancies or defect complexes associated with such vacancies.

We note that, intriguingly, there is an approximate coincidence between the

order of magnitude of our calculated ratio of chemical strain to stoichiometric deviation due to titanium vacancies, $|\epsilon_c/\delta| = 0.4$, and the observed values (+0.5 and +0.8, depending upon weighting of fit) for the strontium-poor samples. Given the magnitude of the observed lattice expansion and the fact that *only* titanium vacancies appear capable of producing an effect of this size, we are led to the intriguing conjecture that, perhaps, the strontium-poor samples exhibit defects that include titanium vacancies and thus a structure more complex than initially thought (simple strontium vacancies or strontium-oxygen divacancies). Of course, to correspond to the stoichiometry observed in the experiments, these complexes would have to involve both a greater number of strontium than titanium vacancies, so that the overall samples are strontium poor, as well as a commensurate number of oxygen vacancies to satisfy charge neutrality (e.g., $V_{Sr_2TiO_4}$, $V_{Sr_4TiO_6}$, etc.). Clearly, more investigation is needed on this point, specifically as to the nature of the point defects in the strontium-poor samples.

3.6 Summary and conclusion

We have calculated both near- and far-field strains for five defects in reconstructed strontium titanate: isolated oxygen, strontium, and titanium vacancies, as well as strontium-oxygen and titanium-oxygen divacancies. Given the propensity of the crystal for local fluctuations in the reconstruction, we report results both for a particular reconstructed state and as averaged over all possible local reconstructions. The reconstructionally averaged near-field strain results are presented and interpreted in terms of the movement of neighboring shells of atoms at increasing distances from the vacancy or divacancy. We report far-field strain results in terms of both elastic dipole tensors, with and without reconstructional averaging,

and associated defect-strain tensors, with reconstructional averaging. Anticipating that far-field effects will necessarily involve contributions from an ensemble of defects, we also present results averaged over all possible orientations of the defect within the bulk crystal. From these averaged tensors, we extract the resultant ratio of chemical strain to stoichiometric defect deviation. Finally, the combination of local and long-range results presented herein will enable determination of x-ray scattering signatures for comparison with experimental results and should further motivate future work on defect mechanics, including the influence of externally imposed strain (such as in heterostructures) on vacancy populations.

For the oxygen vacancy, we find a highly anisotropic elastic dipole tensor, with almost perfect cancellation under orientational averaging. This may be correlated with observed difficulties in controlling oxygen concentration and lack of observation of effects of oxygen-vacancy concentration on lattice strain. The anisotropy of this tensor also suggests that oxygen vacancies may provide a mechanism to shield local internal strains and that application of external stress may allow for control of oxygen stoichiometry. From comparison to lattice-strain studies, we identify both isolated oxygen vacancies and bound strontium-oxygen divacancies as consistent with the experimentally observed chemical strain as a function of oxygen-vacancy concentration in strontium titanate.

For cation non-stoichiometry, we find strong indications that the point defects in strontium-poor strontium titanate are not simple strontium vacancies or strontium-oxygen divacancies, but likely more complicated defect complexes. Further, we identify indications that titanium vacancies may play a role in these defect complexes.

BIBLIOGRAPHY

[1] Daniel E. Grupp and Allen M. Goldman. Giant Piezoelectric Effect in Strontium Titanate at Cryogenic Temperatures. *Science*, 276(5311):392–394, 1997. 49

[2] John H. Barrett. Dielectric Constant in Perovskite Type Crystals. *Phys. Rev.*, 86(1):118–120, 1952. 49

[3] K. A. Müller and H. Burkard. $SrTiO_3$: An intrinsic quantum paraelectric below 4 K. *Phys. Rev. B*, 19(7):3593–3602, 1979. 49

[4] P. A. Fleury, J. F. Scott, and J. M. Worlock. Soft Phonon Modes and the 110°K Phase Transition in $SrTiO_3$. *Phys. Rev. Lett.*, 21(1):16–19, 1968. 49

[5] J. G. Bednorz and K. A. Müller. $Sr_{1-x}Ca_xTiO_3$: An XY Quantum Ferroelectric with Transition to Randomness. *Phys. Rev. Lett.*, 52(25):2289–2292, 1984.

[6] F. Gervais, B. Calès, and P. Odier. Characterization of Strontium Titanate Ceramics by Infrared Reflectivity Spectroscopy and Electron Paramagnetic Resonance. *Mater. Res. Bull.*, 22(12):1629–1633, 1987.

[7] Ronald E. Cohen. Origin of ferroelectricity in perovskite oxides. *Nature*, 358 (6382):136–138, 1992. 49

[8] Hiromoto Uwe and Tunetaro Sakudo. Stress-induced ferroelectricity and soft phonon modes in $SrTiO_3$. *Phys. Rev. B*, 13(1):271–286, 1976. 49

[9] Y. Moritomo, A. Asamitsu, H. Kuwahara, and Y. Tokura. Giant magnetoresistance of manganese oxides with a layered perovskite structure. *Nature*, 380 (6570):141–144, 1996. 49

[10] A. P. Ramirez. Colossal magnetoresistance. *J. Phys.: Condens. Matter*, 9 (39):8171–8199, 1997. 49

[11] W. Zhong, David Vanderbilt, and K. M. Rabe. Phase Transitions in $BaTiO_3$ from First Principles. *Phys. Rev. Lett.*, 73(13):1861–1864, 1994. 49, 50

[12] K. Alex Müller, W. Berlinger, and E. Tosatti. Indication for a novel phase in the quantum paraelectric regime of $SrTiO_3$. *Z. Phys. B*, 84(2):277–283, 1991. 49

[13] N.-H. Chan, R. K. Sharma, and D. M. Smyth. Nonstoichiometry in $SrTiO_3$. *J. Electrochem. Soc.*, 128(8):1762–1769, 1981. 49

[14] N. G. Eror and U. Balachandran. High-Temperature Defect Structure of Acceptor-Doped Strontium Titanate. *J. Am. Ceram. Soc.*, 65(9):426–431, 1982. 49

[15] J. F. Schooley, W. R. Hosler, and Marvin L. Cohen. Superconductivity in Semiconducting $SrTiO_3$. *Phys. Rev. Lett.*, 12(17):474–475, 1964. 49

[16] C. S. Koonce, Marvin L. Cohen, J. F. Schooley, W. R. Hosler, and E. R. Pfeiffer. Superconducting Transition Temperatures of Semiconducting $SrTiO_3$. *Phys. Rev.*, 163(2):380–390, 1967. 49

[17] Hiromi Unoki and Tunetaro Sakudo. Electron Spin Resonance of Fe^{3+} in $SrTiO_3$ with Special Reference to the 110°K Phase Transition. *J. Phys. Soc. Jpn.*, 23(3):546–552, 1967. 49, 59

[18] Berthold Alefeld. Die Messung der Gitterparameteränderung von Strontiumtitanat am Phasenübergang bei 108 °K. *Z. Phys.*, 222(2):155–164, 1969.

[19] Th. von Waldkirch, K. A. Müller, and W. Berlinger. Fluctuations in $SrTi_3$ near the 105-K Phase Transition. *Phys. Rev. B*, 7(3):1052–1066, 1973. 49, 59

[20] W. Zhong and David Vanderbilt. Competing Structural Instabilities in Cubic Perovskites. *Phys. Rev. Lett.*, 74(13):2587–2590, 1995. 50, 55, 58

[21] M. E. Lines and A. M. Glass. *Principles and Applications of Ferroelectrics and Related Materials*. Clarendon Press, Oxford, UK, 1977. 50

[22] Aaron Fleet, Darren Dale, A. R. Woll, Y. Suzuki, and J. D. Brock. Multiple Time Scales in Diffraction Measurements of Diffusive Surface Relaxation. *Phys. Rev. Lett.*, 96(5):055508, 2006. 50

[23] M. J. Gillan. The elastic dipole tensor for point defects in ionic crystals. *J. Phys. C*, 17(9):1473–1488, 1984. 51

[24] B. G. Dick, Jr. and A. W. Overhauser. Theory of the Dielectric Constants of Alkali Halide Crystals. *Phys. Rev.*, 112(1):90–103, 1958. 53

[25] M. Javed Akhtar, Zeb-Un-Nisa Akhtar, Robert A. Jackson, and C. Richard A. Catlow. Computer Simulation Studies of Strontium Titanate. *J. Am. Ceram. Soc.*, 78(2):421–428, 1995. 53, 55, 56, 57

[26] P. P. Ewald. Die Berechnung optischer und elektrostatischer Gitterpotentiale. *Ann. Phys.*, 369(3):253–287, 1921. 54

[27] Tom Darden, Darrin York, and Lee Pedersen. Particle mesh Ewald: An $N \cdot \log(N)$ method for Ewald sums in large systems. *J. Chem. Phys.*, 98(12): 10089–10092, 1993. 54

[28] Ulrich Essmann, Lalith Perera, Max. L Berkowitz, Tom Darden, Hsing Lee,

and Lee G. Pedersen. A smooth particle mesh Ewald method. *J. Chem. Phys.*, 103(19):8577–8593, 1995.

[29] Markus Deserno and Christian Holm. How to mesh up Ewald sums. I. A theoretical and numerical comparison of various particle mesh routines. *J. Chem. Phys.*, 109(18):7678–7693, 1998. 54

[30] R. A. Buckingham. The Repulsive Interaction of Atoms in S States. *Trans. Faraday Soc.*, 54(4):453–459, 1958. 54

[31] Max Born and Joseph E. Mayer. Zur Gittertheorie der Ionenkristalle. *Z. Phys.*, 75(1–2):1–18, 1932. 54

[32] J. E. Lennard-Jones. Cohesion. *Proc. Phys. Soc.*, 43(5):461–482, 1931. 54

[33] Johannes Diderik van der Waals. *Over de Continuiteit van den Gas- en Vloeistoftoestand*. PhD thesis, University of Leiden, 1873. 54

[34] G. V. Lewis and C. R. A. Catlow. Potential models for ionic oxides. *J. Phys. C*, 18(6):1149–1161, 1985. 55

[35] C. R. A. Catlow and A. M. Stoneham. Ionicity in solids. *J. Phys. C*, 16(22): 4321–4338, 1983. 55

[36] Yu A. Abramov, V. G. Tsirelson, V. E. Zavodnik, S. A. Ivanov, and I. D. Brown. The Chemical Bond and Atomic Displacements in $SrTiO_3$ from X-ray Diffraction Analysis. *Acta Crystallogr.*, B51(6):942–951, 1995. 58

[37] K. A. Müller, W. Berlinger, and F. Waldner. Characteristic Structural Phase Transition in Perovskite-Type Compounds. *Phys. Rev. Lett.*, 21(12):814–817, 1968. 58

[38] E. Pytte and J. Feder. Theory of a Structural Phase Transition in Perovskite-Type Crystals. *Phys. Rev.*, 187(3):1077–1088, 1969. 58

[39] W. Zhong and David Vanderbilt. Effect of quantum fluctuations on structural phase transitions in $SrTiO_3$ and $BaTiO_3$. *Phys. Rev. B*, 53(9):5047–5050, 1996. 58

[40] Magnus R. Hestenes and Eduard Stiefel. Methods of Conjugate Gradients for Solving Linear Systems. *J. Res. Natl. Bur. Stand.*, 49(6):409–436, 1952. 59

[41] E. Polak and G. Ribière. Note sur la Convergence de Méthodes de Directions Conjuguées. *Rev. Fr. Inform. Rech. O.*, 3(16):35–43, 1969. 59

[42] M. Leslie and M. J. Gillan. The energy and elastic dipole tensor of defects in ionic crystals calculated by the supercell method. *J. Phys. C*, 18(5):973–982, 1985. 59

[43] J. F. Scott and Matthew Dawber. Oxygen-vacancy ordering as a fatigue mechanism in perovskite ferroelectrics. *Appl. Phys. Lett.*, 76(25):3801–3803, 2000. 86

[44] M. Cherry, M. S. Islam, and C. R. A. Catlow. Oxygen Ion Migration in Perovskite-Type Oxides. *J. Solid State Chem.*, 118(1):125–132, 1995.

[45] C. H. Park and D. J. Chadi. Microscopic study of oxygen-vacancy defects in ferroelectric perovskites. *Phys. Rev. B*, 57(22):R13961–R13964, 1998.

[46] M. V. Raymond and D. M. Smyth. Defects and Charge Transport in Perovskite Ferroelectrics. *J. Phys. Chem. Solids*, 57(10):1507–1511, 1996.

[47] Lixin He and David Vanderbilt. First-principles study of oxygen-vacancy pinning of domain walls in $PbTiO_3$. *Phys. Rev. B*, 68(13):134103, 2003.

[48] Veng Cheong Lo. Modeling the role of oxygen vacancy on ferroelectric properties in thin films. *J. Appl. Phys.*, 92(11):6778–6786, 2002.

[49] Shigenobu Kimura, Jun Yamauchi, Masaru Tsukada, and Satoshi Watanabe. First-principles study on electronic structure of the (001) surface of $SrTiO_3$. *Phys. Rev. B*, 51(16):11049–11054, 1995.

[50] Victor E. Henrich, G. Dresselhaus, and H. J. Zeiger. Surface defects and the electronic structure of $SrTiO_3$ surfaces. *Phys. Rev. B*, 17(12):4908–4921, 1978. 86

[51] R. J. D. Tilley. An Electron Microscope Study of Perovskite-Related Oxides in the Sr–Ti–O System. *J. Solid State Chem.*, 21(4):293–301, 1977. 86

[52] K. Szot and W. Speier. Surfaces of reduced and oxidized $SrTiO_3$ from atomic force microscopy. *Phys. Rev. B*, 60(8):5909–5926, 1999. 86

[53] Hisao Yamada and G. R. Miller. Point Defects in Reduced Strontium Titanate. *J. Solid State Chem.*, 6(1):169–177, 1973. 86, 89

[54] Shintaro Yamamichi, Hisato Yabuta, Toshiyuki Sakuma, and Yoichi Miyasaka. (Ba+Sr)/Ti ratio dependence of the dielectric properties for $(Ba_{0.5}Sr_{0.5})TiO_3$ thin films prepared by ion beam sputtering. *Appl. Phys. Lett.*, 64(13):1644–1646, 1994. 86

[55] T. R. Taylor, P. J. Hansen, N. Pervez, B. Acikel, R. A. York, and J. S. Speck. Influence of stoichiometry on the dielectric properties of sputtered strontium titanate thin films. *J. Appl. Phys.*, 94(5):3390–3396, 2003. 86

[56] Tsuyoshi Ohnishi, Keisuke Shibuya, Takahisa Yamamoto, and Mikk Lippmaa. Defects and transport in complex oxide thin films. *J. Appl. Phys.*, 103(10): 103703, 2008. 89

[57] S. N. Ruddlesden and P. Popper. New compounds of the K_2NiF_4 type. *Acta Crystallogr.*, 10(8):538–539, 1957. 89

[58] S. N. Ruddlesden and P. Popper. The compound $Sr_3Ti_2O_7$ and its structure. *Acta Crystallogr.*, 11(1):54–55, 1958. 89

[59] Francis S. Galasso. *Structure, Properties and Preparation of Perovskite-Type Compounds*, pages 18–19. Pergamon Press, Oxford, UK, 1969. 90

CHAPTER 4

IMPACT OF OCTAHEDRAL ROTATIONS ON RUDDLESDEN–POPPER PHASES OF ANTIFERRODISTORTIVE PEROVSKITES

4.1 Introduction

Perovskites possess a vast range of scientifically interesting and technologically important properties. These materials are highly valued for their dielectricity[1–4], ferroelectricity[5–7], semiconductivity[8–11], superconductivity[12–14], catalytic activity[15–17], and colossal magnetoresistance[18]. Such physical properties allow for the use of perovskites in diverse technological applications, including tunneling semiconductor valves and magnetic tunnel junctions in spintronics[19–21], dielectric insulators in dynamic random access memory[22, 23], thin films in graded ferroelectric devices (GFDs)[24, 25], and alternative gates in metal-oxide-semiconductor field transistors (MOSFETs)[26, 27].

Cation stoichiometry has a large impact on the physics of these materials, but is difficult[28, 29] to control during film growth. Cation non-stoichiometries in the perovskites can potentially take the form of point or planar defects, with perovskites experimentally found to resist point defect formation upon sufficient cation non-stoichiometry[30–32]. In $A^{2+}B^{4+}O_3^{2-}$ materials (such as $SrTiO_3$) with an excess of species A (or, more precisely, additional AO to maintain charge neutrality), the resulting planar defects produce a series of homologous compounds of the form $A_{n+1}B_nO_{3n+1}$. (Note that bulk ABO_3 corresponds to one end member of this series, $n = \infty$, and bulk AO corresponds to the other end member, $n = 0$.) The $A_{n+1}B_nO_{3n+1}$ compounds, known as the Ruddlesden–Popper (RP) phases[33, 34],

reflect the modification of the cation stoichiometry by the addition of an extra unit of AO per n units of bulk ABO_3 material. Structurally, they take the form of bulk ABO_3, separated every n layers by the insertion of excess (001) planes of AO to create stacking faults of the form $\ldots/AO/BO_2/AO/AO/BO_2/AO/\ldots$ in the normal $\ldots/AO/BO_2/AO/BO_2/AO/\ldots$ stacking sequence of the material. Across each such stacking fault, the bulk perovskite slabs are alternately displaced by in-plane vectors of the form $\frac{a_0}{2}[\pm 1, \pm 1, 0\,]$. Figure 4.1 depicts four members of the homologous series $A_{n+1}B_nO_{3n+1}$, with $n = 1$, 2, 3, and ∞.

RP phases, specifically, manifest additional properties beyond those of bulk perovskites; these include high dielectricity[35, 36], thermoelectricity[37], photocatalysis[38], unconventional superconductivity[39], quantum criticality[40], metamagnetism[41], ferromagnetism[42], colossal magnetoresistance[43], and x-ray optic adaptability[44]. Despite the interest in such compounds, experimentalists have faced difficulties growing RP phases for "intermediate" values of n ($n \gtrsim 4$)[45–48]. For example, strontium titanate ($SrTiO_3$) compounds with such stoichiometries tend not to form growths of a single uniform RP phase, but rather materials with multiple regions, each with RP phases of different values of n, so-called "intergrowths."[49–51] Indeed, conventional ceramic powder sintering has only produced single-phase RP samples for $n \leq 3$: Sr_2TiO_4, $Sr_3Ti_2O_7$, and $Sr_4Ti_3O_{10}$[49, 52]. More recently, successful creation of intermediate members of the $Sr_{n+1}Ti_nO_{3n+1}$ series has been accomplished with advanced techniques for epitaxial growth of thin-films under thermodynamical non-equilibrium conditions, such as sputtering[29], pulsed laser deposition (PLD)[53–55], and molecular beam epitaxy (MBE)[36, 56–58], with characterization by high-resolution transmission electron microscopy (HRTEM)[57] and x-ray diffraction (XRD)[59]. Such recent observations renew the urgency for a careful theoretical study of RP phases with

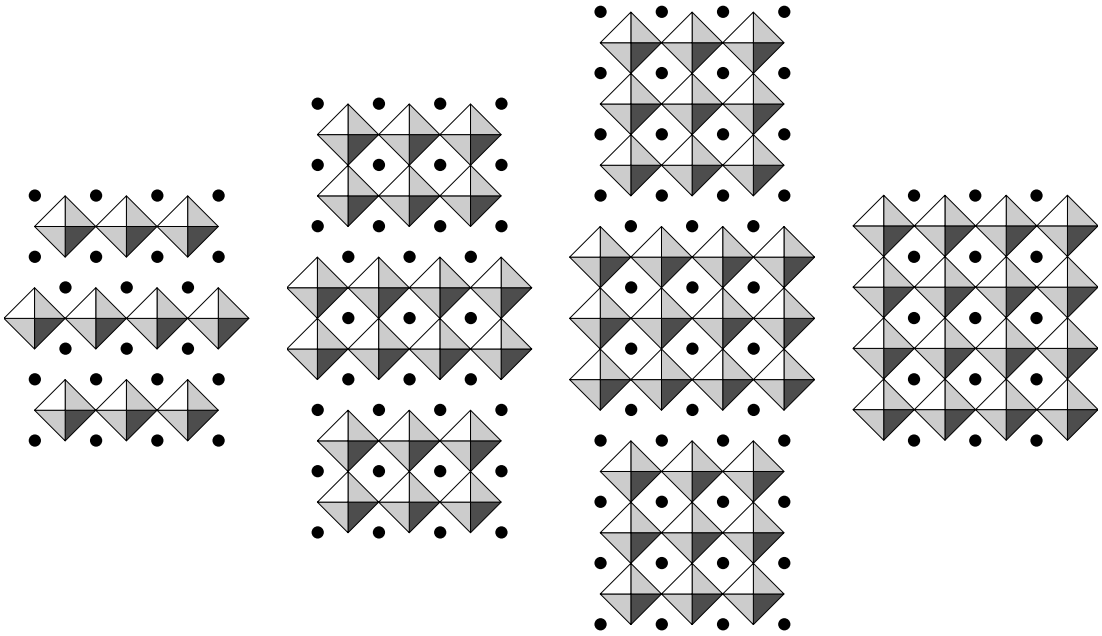

(a) A_2BO_4 (b) $A_3B_2O_7$ (c) $A_4B_3O_{10}$ (d) ABO_3

Figure 4.1: Four members of series of homologous compounds of form $A_{n+1}B_nO_{3n+1}$, showing n layers of bulk perovskite between stacking faults: (a) A_2BO_4 with $n = 1$, (b) $A_3B_2O_7$ with $n = 2$, (c) $A_4B_3O_{10}$ with $n = 3$, and (d) bulk ABO_3 with $n = \infty$.

intermediate and large values of n.

Previous theoretical work on RP phases of perovskites includes a limited number of both *ab initio* electronic structure calculations and empirical potential studies. A pioneering empirical-potential study[60] in the 1980's considered all values of $n \leq 12$ for strontium titanate but did not report sufficient precision to resolve differences among any of the phases above $n = 1$. A decade later, a subsequent empirical-potential study[61] was able to resolve differences among phases but only considered phases for $n \leq 4$. Total energy electronic structure studies have also been carried out, primarily for strontium titanate[62–68] ($n \leq 3$) but also for three additional perovskite transition-metal oxides[66] ($n = 2$ *only*). None of these studies have explored the significant interactions which we find to exist between the rotational states of the oxygen octahedra on opposite sides of the AO/AO stacking faults.

Many perovskites that form RP phases exhibit antiferrodistortive (AFD) behavior in which the oxygen octahedra tend to rotate in an alternating spatial pattern from their ideal orientations with a relatively low energy scale, so that numerous structural phases exist for the corresponding bulk materials. Unless a full quantum statistical treatment of the RP phases is considered in the theoretical calculations, the bulk regions in these phases will tend to relax to the zero-temperature ground state within the model used to describe the material. One must therefore carefully and explicitly consider two interrelated effects: (a) the interaction between different possible antiferrodistortive reconstructions on either side of the stacking faults and (b) the possibility that these reconstructions will assume different orientations and thus prefer lattice structures in potential conflict across the stacking fault. If the different possible reconstructions of octahedral rotations

are not considered, the true ground state of the RP phases may be missed. If the lattice vectors are not allowed to relax fully, the extraction of the formation energy of the RP phases will suffer errors which scale with the size of the bulk regions (i.e., linearly with n), as we demonstrate below in Section 4.5.1. The aforementioned theoretical works thus have limited applicability, even for the small values of n which they consider.

Indeed, experiments reveal that these effects are known to be present in RP phases of perovskites; for example, both $Sr_{n+1}Ti_nO_{3n+1}$ and $Ca_{n+1}Ti_nO_{3n+1}$ exhibit rotations of their oxygen octahedra, for $n = 2$ and $n = 3$ RP phases[69]. Previous work has considered general group-theoretical studies of the space groups of possible octahedral rotation patterns in RP phases[70, 71], but with restrictions either to the $n = 1$ RP phase or to a limited number of possible relative rotational orientations on opposite sides of the stacking faults.

In this work, we provide a careful, comprehensive atomistic study of the Ruddlesden–Popper phases of a physical model of an antiferrodistortive perovskite, considering a wide range of n (specifically, $n = 1 \ldots 30$), properly accounting for the full lattice relaxation of the RP phases, and exploring all combinatorial possibilities of different orientations of oxygen octahedra on opposite sides of the AO/AO stacking faults. In Section 4.2, we introduce the class of materials which we consider, those antiferrodistortive perovskites which form intrinsic RP phases and belong to the Glazer system of the greatest symmetry commonly found in nature: $a^-a^-a^-$[72]. Section 4.3 then presents an exhaustive catalogue of the different possible structures for RP phases in perovskites within this system. In generating this catalogue, we introduce a convenient symmetry algebra which allows one to quickly enumerate the structures, and we use it to find a total of five symmetry-

distinct possibilities (consistent with distorted phases Nos. 18–22 which Hatch et al.[71] found for the $n = 1$ RP phase after extensive searching with a computer program). Section 4.4 then introduces the shell-potential model and the numerical techniques which we use.

Section 4.5.1 explores the aforementioned five distinct configurations for all RP phases for $n = 1 \ldots 30$. We find that the energies of RP phases are indeed quite sensitive to octahedral rotations, sufficiently sensitive that unfavorable configurations become unstable relative to phase separation into bulk perovskite and bulk A-oxide. In fact, the effect is sufficiently strong to suggest some intriguing possibilities. For low densities of stacking faults (high n), the rotational states of the octahedra neighboring the faults might be constrained, even at temperatures where the octahedra in the bulk librate freely, so that different degrees of order are observed in the bulk and at the interfaces. For high densities of stacking faults (low n), this effect may increase the transition temperatures associated with the octahedral rotations.

Section 4.5.2 considers interactions between the stacking faults present in the RP phases. For each configuration, we examine the energy of the $A_{n+1}B_nO_{3n+1}$ RP phases as a function of n, which directly measures the separation between stacking faults. We demonstrate that the interaction is quite sensitive to the octahedral rotations, differing in strength by as much as a factor of two depending on the rotations. Next, Section 4.5.3 examines the issue of the asymptotic form of this interaction for $n \to \infty$. We find that the interaction between stacking faults varies as the inverse of the distance between them, and we extract both the binding energies of stacking faults and the formation energies of isolated faults. Again, we find that the interaction energy between faults is highly sensitive to the

different possible rotational states of the oxygen octahedra and may even lead to ordering at the stacking faults at temperatures where the bulk regions have lost their orientational order. This section then concludes with a proposal for a simple physical mechanism to explain the strong dependence of the interfacial energy on the rotational state of the octahedra: some configurations result in movement of like-charged neighboring oxygen ions directly toward each other and thus are high in energy, whereas others result in movement of oxygen ions past each other and thus are low in energy.

Finally, in Section 4.5.4, exerting care in tracking the chemical potentials of the various reference systems, we verify that the formation of isolated planar stacking faults is favored over the formation of point defects in our model material, regardless of the rotational state of the oxygen octahedra.

4.2 Background

In this work, we embark on a study of the generic effects of octahedral rotations on RP phases. For this first such study, we shall focus on the most highly symmetric of the twenty-three possible Glazer systems[72]. There are two such systems, denoted in Glazer notation as $a^+a^+a^+$ and $a^-a^-a^-$, only the latter of which is commonly found in nature. Examples of $a^-a^-a^-$ perovskites include $LaAlO_3$[72], $NdAlO_3$[73, 74], $CeAlO_3$[74], $BiFeO_3$[75], $LiNbO_3$[75], $LiTaO_3$[75], $PbZr_{0.9}Ti_{0.1}O_3$ (PZT)[76], and many others catalogued by Glazer[72] and Megaw and Darlington[77].

The Glazer notation refers to the relative state of rotation of neighboring oxygen octahedra in antiferrodistortive reconstructions of the perovskite structure. In actual fact, the motion of the octahedra within such reconstructions is only ap-

proximately a rotation as the oxygen atoms are confined to the faces of each cube; regardless, we shall refer to their motion as rotational throughout. Glazer exhaustively catalogued all twenty-three possible patterns of these octahedral rotations ("tilts" in his terminology)[72, 76], with each category assigned an appropriate nomenclature to denote the axis of rotation and the relative sign of successive rotations along that axis. In brief, in the $a^-a^-a^-$ system, all oxygen octahedra rotate either clockwise or counterclockwise about a fixed trigonal axis in an alternating checkerboard pattern in all three dimensions, resulting in a cell-doubling reconstruction with a $2 \times 2 \times 2$ supercell. (Greater details appear in Section 4.3.)

The antiferrodistortive phase transition, associated with these rotations, occurs due to the softening of the Γ_{25} optical phonons at the R corner ([111] zone boundary) of the Brillouin zone, as famously studied experimentally[78–80] and theoretically[81, 82] and reviewed extensively[83]. The transition is therefore also sometimes known as a Zone Boundary Transition (ZBT) and was recognized even earlier as a means by which crystals could double the size of their primitive cells[84]. The rotation of the oxygen octahedra accompany the softening of these phonons, with their rotation angles serving as the order parameters[85]. The degeneracy of this phonon mode in the higher-temperature cubic phase enables the rotation of octahedra about different axes — $\langle 100 \rangle$, $\langle 110 \rangle$, and $\langle 111 \rangle$ — to break the crystal's symmetry below its critical temperature. While the $a^-a^-a^-$ system results from rotations about the $\langle 111 \rangle$ axis, all three systems emerge from the same underlying instability[83, 86], with anharmonic interactions determining the resulting low-temperature lattice symmetry[87]. As the underlying physics is so similar, we thus expect that perovskites in Glazer systems other than $a^-a^-a^-$ will exhibit similar generic behaviors to the results expounded below.

In seeking a model potential for our study, we searched the literature for shell-potential parameters among the $a^-a^-a^-$ perovskites. Unfortunately, we discovered that the ground states of the available models generally do not correctly match their corresponding Glazer systems.[88] We were only able to identify a single material, lanthanum aluminate ($La^{3+}Al^{3+}O_3^{2-}$), with a ground state in the correct Glazer system.[88] Unfortunately, lanthanum aluminate does not form *intrinsic* RP phases, since its composition as $A_{n+1}B_nO_{3n+1}$ would violate basic charge balance; intrinsic RP formation requires perovskites with an $A^{2+}B^{4+}O_3^{2-}$ chemical formula for the additional $A^{2+}O^{2-}$ layer to be neutral. Lanthanum aluminate, however, can form *extrinsic* RP phases by incorporation of additional neutral layers of another perovskite, strontium oxide: $SrO \cdot La_nAl_nO_{3n}$.

For simplicity of this initial theoretical study, we focus on perovskites that form intrinsic RP phases, examples of which from the $a^-a^-a^-$ system do indeed exist in nature (e.g., $BaTbO_3$[72]). However, we are not aware of shell potentials for any of these materials. On the other hand, we discovered that the shell-potential model commonly used for strontium titanate ($Sr^{2+}Ti^{4+}O_3^{2-}$), which forms intrinsic RP phases, does possess a ground state of the $a^-a^-a^-$ type.

Indeed, on a microscopic level, strontium titanate is very similar to lanthanum aluminate. In fact, early x-ray experiments[89, 90] erroneously predicted a low-temperature ($T \lesssim 35$ K) phase transition in strontium titanate to a rhombohedral lattice (generally associated with $a^-a^-a^-$ microscopic ordering), only to be corrected by subsequent spectroscopic studies[78, 91]. Strontium titanate assumes its actual tetragonal ground-state structure through a famous cell-doubling antiferrodistortive phase transition near 105 K[92], whose "physical origin is the same"[85] as that of lanthanum aluminate. Indeed, this transition is "strikingly

analogous in all respects"[93, 94] to that of lanthanum aluminate, although the energy scales are quite different. (The structural phase transition temperature for lanthanum aluminate is 800 K[85, 95].) Further connections between these two perovskites are enabled by the classical concept of the Goldschmidt tolerance factor[96], $t = \frac{1}{\sqrt{2}} \frac{r_A + r_O}{r_B + r_O}$, a normalized ratio of the radii of ABO_3 ions historically used to categorize perovskites and predict their ground states[97]. In fact, lanthanum aluminate has a tolerance factor within 1% of that of strontium titanate (data compiled by Shannon[98]).

In sum, the parameters for the shell potential commonly used for strontium titanate describe a perovskite which intrinsically forms RP phases within the desired $a^-a^-a^-$ Glazer system. It is not surprising, then, to discover empirical evidence for perovskites, such as lanthanum aluminate, which closely resemble strontium titanate but with $a^-a^-a^-$ octahedral rotations. The standard shell potential for strontium titanate can thus reasonably be utilized as a parameterization for generic $a^-a^-a^-$ perovskites which form RP phases. Therefore, in interpreting our results, one should be mindful that details, such as the values which we find for the various quantities, may not apply to any specific perovskite. However, the general phenomena that we uncover, such as the enumeration of possible octahedral configurations and the general form and scale of the various interactions, may be taken as representative of the class of $a^-a^-a^-$ perovskites in RP phases. Moreover, since the underlying physical mechanism is the same for other Glazer systems, many of the phenomena which we uncover should be considered for the RP phases of all AFD perovskites.

4.3 Classification of octahedral rotations in RP phases

We return now to a careful examination of the specifics of the $a^-a^-a^-$ Glazer reconstruction, as visualized in Figure 4.2. The oxygen octahedra each rotate around one of the eight possible $\langle 111 \rangle$ axes (expressed in the coordinates of the closely related cubic structure), with neighboring octahedra rotating in opposite directions in a cell-doubling, alternating three-dimensional $2 \times 2 \times 2$ checkerboard pattern. As shown in Figure 4.3, the crystal itself responds to the presence of these trigonal rotations about a common axis by stretching or compressing along that axis, forming a rhombohedral Bravais lattice. Selection of a specific oxygen octahedron as reference then permits eight possible distinct bulk configurations, each characterized and enumerated by the particular choice of one of the eight possible trigonal rotation axes for that specific octahedron. These eight reconstructions can be characterized either as $\pm[\pm 1, \pm 1, 1\,]$, namely a selection of an overall $\pm$ sign and a choice of one of the four *unsigned* $[\pm 1, \pm 1, 1\,]$ rotation axes, or, alternatively, simply as one of eight *signed* $[\pm 1, \pm 1, \pm 1]$ axes.

The former perspective of the eight reconstructions is visualized in Figure 4.4. The four (unsigned) $[\pm 1, \pm 1, 1\,]$ rotation axes designate the reconstruction at an arbitrary origin of the crystal, where a final choice of sign determines whether the rotation at the origin is either clockwise ("positive") or counterclockwise ("negative"), thereby fully specifying the microscopic state of the crystal. Note that a change in this sign choice corresponds precisely to a rigid translation of the crystal by a [111] primitive translation vector (to a position in the crystal with opposite sign of rotation, due to the checkerboard pattern of the reconstruction). Such a translation would not be observable on a macroscopic level.

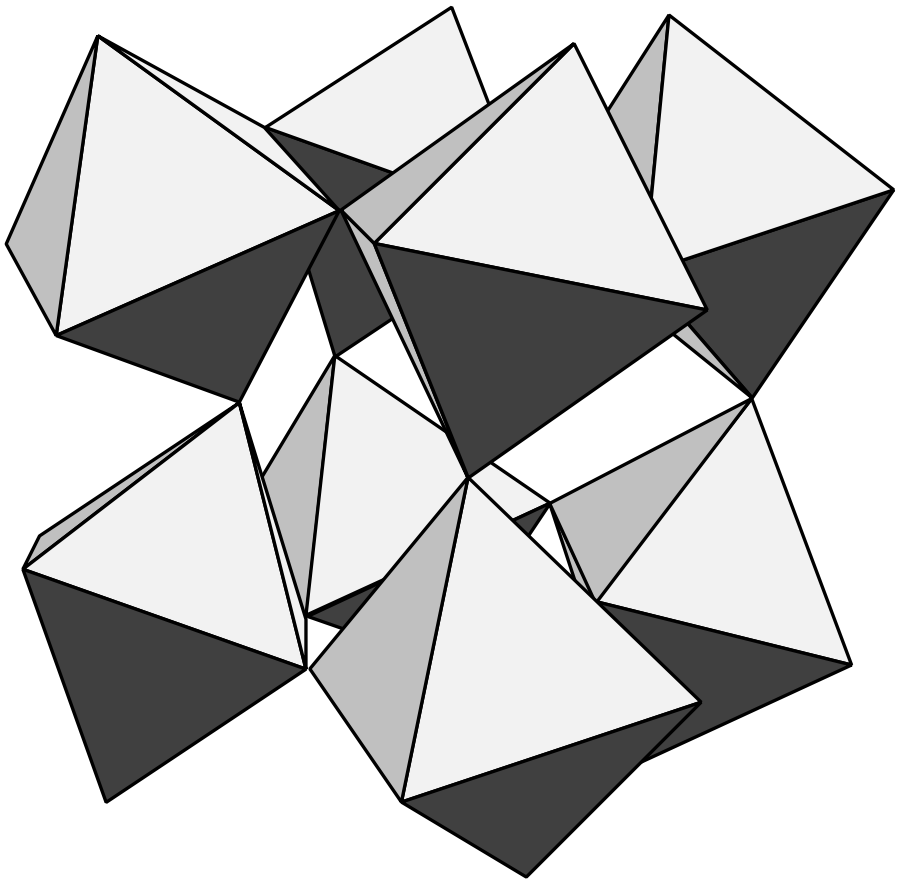

Figure 4.2: Perovskite reconstruction in $a^-a^-a^-$ Glazer notation, showing rotations of oxygen octahedra in opposite directions in a cell-doubling, alternating three-dimensional $2 \times 2 \times 2$ checkerboard pattern. (Degree of rotation exaggerated for illustrative purposes.)

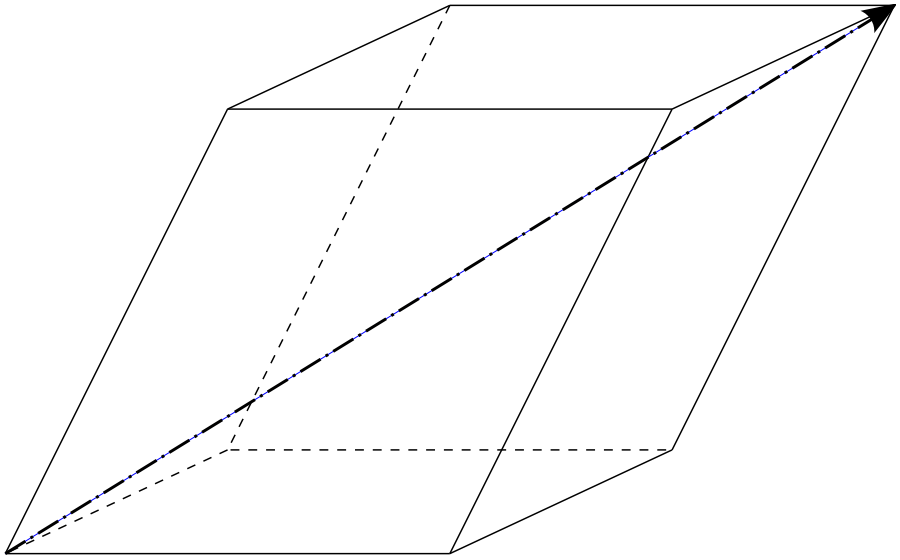

Figure 4.3: Rhombohedral lattice as ground state of cell-doubling $2 \times 2 \times 2$ reconstruction of bulk strontium titanate, showing broken symmetry due to [111] trigonal octahedral rotation axis (dash-dotted line). (Rhombohedral distortion exaggerated for illustrative purposes.)

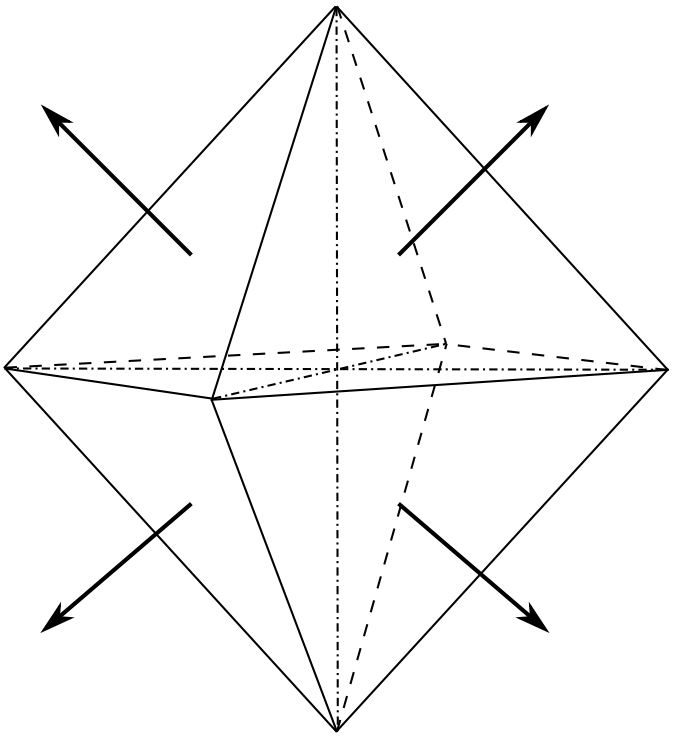

Figure 4.4: "Positive" senses of the four (unsigned) $[\pm 1, \pm 1, 1\,]$ rotation axes for oxygen octahedra ($\hat{e}_3$ axis out of the page).

4.3.1 Isolated stacking faults

The RP phases observed in experiments[49, 52, 99] consist of superlattices of bulk perovskite slabs separated by the insertion of excess (001) AO planes to create stacking faults of the form .../AO/BO_2/AO/AO/BO_2/AO/... in the normal .../AO/BO_2/AO/BO_2/AO/... stacking sequence. Across each such stacking fault, the bulk perovskite slabs are alternately displaced by in-plane vectors of the form $\frac{a_0}{2}[\pm 1, \pm 1, 0]$. To our knowledge, however, no one has yet explored the effects of different combinations of possible symmetry-related bulk reconstructions on opposite sides of the repeated AO planes.

To enumerate the distinct possible configurations for such stacking faults, we restrict our consideration to cases where the material on either side of the stacking fault possesses a specific bulk reconstruction throughout. We first focus on the reconstruction of the bulk material on the side "below" (at lower values for $\hat{e}_3$) the AO/AO stacking fault, which we shall denote as side $\mathfrak{A}$. As discussed above, the microscopic configuration of bulk material on side $\mathfrak{A}$ can be fully specified by noting the rotation axis of the octahedron at an arbitrary, but from then onward fixed, origin $O_{\mathfrak{A}}$. The rotation axis of this particular reference oxygen octahedron can then assume any of eight choices among the $\langle 111 \rangle$ axes, which we can regard as a selection of an overall $\pm$ sign ("positive" or "negative") and a choice of one of the four (unsigned) $[\pm 1, \pm 1, 1]$ rotation axes. This specification then determines the entire microscopic structure of the bulk material in side $\mathfrak{A}$, according to the $2\times2\times2$ three-dimensional checkerboard pattern of alternating signs for the rotation axes. For the present purpose, we choose always to select the reference octahedron $O_{\mathfrak{A}}$ from among those octahedra immediately neighboring the stacking fault which have a positive rotation in the above sense of the choice of overall $\pm$ sign.

Next, as noted above, the bulk perovskite on the other side, $\mathfrak{B}$, of the stacking fault is displaced, in general, by a vector $\frac{a_0}{2}[\pm 1, \pm 1, 0\,]$ relative to side $\mathfrak{A}$. Temporarily disregarding the rotational state of all octahedra, we note that all four of these displacements are equivalent, since the octahedra on $\mathfrak{B}$ are positioned at the centers of squares formed by the octahedra on $\mathfrak{A}$. (See Figure 4.5.) This equivalence (apart from rotational states of the octahedra) allows us to choose a standardized displacement $\mathbf{D} \equiv \frac{a_0}{2}[+1, +1, 0\,]$ from $O_{\mathfrak{A}}$ to select the origin $O_{\mathfrak{B}}$. (More specifically, $O_{\mathfrak{B}} = O_{\mathfrak{A}} + \mathbf{D} + \zeta a_0 \hat{e}_3$, where $\zeta \approx 3/2$ represents the vertical displacement between octahedra on opposite sides of the stacking fault, and $\hat{e}_3$ is a unit vector in the [001] direction.)

The rotation state of $O_{\mathfrak{B}}$ then completely specifies the entire microscopic structure of the bulk material in side $\mathfrak{B}$. This rotation state can be specified as a selection of an overall $\pm$ sign ("positive" or "negative") and a choice of one of the four (unsigned) $[\pm 1, \pm 1, 1\,]$ rotation axes. Figure 4.5 illustrates exactly these two possible choices of sign, where the reference octahedron on side $\mathfrak{B}$ is either positive (Figure 4.5(a)) or negative (Figure 4.5(b)). Generically below, we shall refer to these two possible sign patterns in the stacking-fault configuration as "+" and "−", respectively, reflecting the overall sign of the rotation of $O_{\mathfrak{B}}$. The combination of these two sign patterns and the four possible unsigned rotation axes (not indicated in Figure 4.5) for each origin, $O_{\mathfrak{A}}$ and $O_{\mathfrak{B}}$, leads to a total of $2 \times (4 \times 4) = 32$ distinct possible configurations for this stacking fault.

Next, we consider equivalence of stacking faults under application of C_{4z} symmetry. As discussed above, the rotation axis of $O_{\mathfrak{A}}$ can always be selected to be among the four (unsigned) $[\pm 1, \pm 1, 1\,]$ axes. Because C_{4z} symmetries interconvert all four of these axes ($C_{4z} \circ [111] = [\bar{1}11]$, $C_{4z}^2 \circ [111] = [\bar{1}\bar{1}1]$, $C_{4z}^3 \circ [111] = [1\bar{1}1]$),

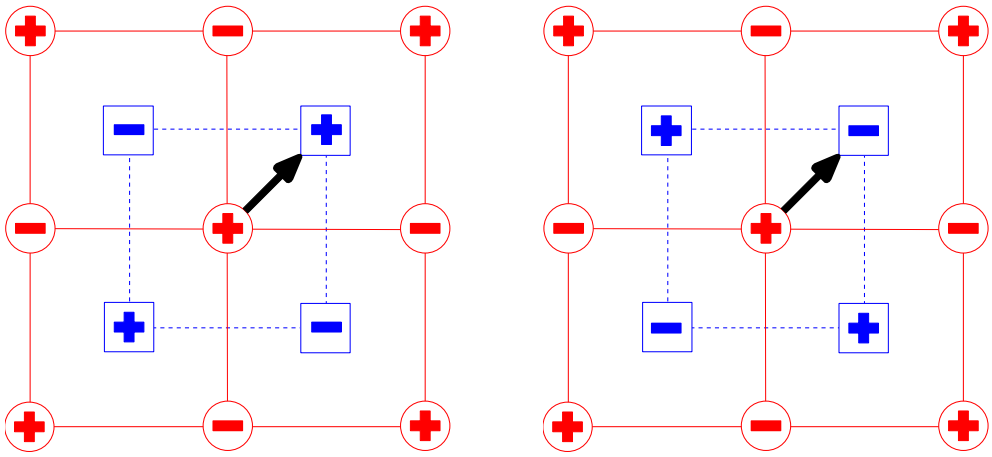

(a) $+O_{\mathfrak{B}}$ (b) $-O_{\mathfrak{B}}$

Figure 4.5: Sign pattern of octahedral rotations on opposite sides of stacking fault: octahedra in lower layer $\mathfrak{A}$ (○) and upper layer $\mathfrak{B}$ (□) and standardized displacement $\mathbf{D}$ (⟶). Panels (a) and (b) depict the two distinct choices for sign of rotation (+ and −, respectively) of $O_{\mathfrak{B}}$.

an overall rotation of the coordinate system can be found to make the $O_{\mathfrak{A}}$ rotation about the [111] axis. We may thus define the rotation axis of $O_{\mathfrak{A}}$ to always be the (unsigned) $[+1, +1, 1]$ axis. This then narrows the phase space of thirty-two configurations listed above to now only $2 \times (1 \times 4) = 8$ distinct configurations.

These eight distinct configurations can be enumerated using two related nomenclatures (seen in Table 4.1), one which is algebraically explicit and suitable for symmetry arguments and the other which is more compact and convenient for communication. In the former case of the *algebraic specifier*, we enumerate each configuration by specification of the rotation states of each reference octahedron, $O_{\mathfrak{A}}$ and $O_{\mathfrak{B}}$, expressing the rotation states in terms of (signed) $[\pm 1, \pm 1, \pm 1]$ vectors. For example, if $O_{\mathfrak{A}}$ is in rotation state [111] and $O_{\mathfrak{B}}$ is in rotation state $[11\bar{1}]$, we write $(111 \Longrightarrow 11\bar{1})$. For a more compact notation, we can take, without loss of generality as shown above, the rotation state of $O_{\mathfrak{A}}$ to always be [111]. The unsigned rotation axis of $O_{\mathfrak{B}}$ is then related to that of $O_{\mathfrak{A}}$ by one of the four C_{4z} rotations of angles $\{0, \frac{\pi}{2}, \pi, \frac{3\pi}{2}\}$. To denote the configuration of the stacking fault, we then append the remaining choice of $\pm$ sign for $O_{\mathfrak{B}}$ to its rotation angle to produce a compound *rotation-sign specifier*. For example, the $(111 \Longrightarrow 11\bar{1})$ configuration from the preceding example may be more compactly written as $[\pi^-]$ (since $-C_{4z}^2 \circ [111] = -[\bar{1}\bar{1}1] = [11\bar{1}]$). Finally, Table 4.1 enumerates all eight configurations according to both their rotation-sign and algebraic specifiers.

The above enumerated eight stacking-fault configurations can be reduced yet further by considering the effects of additional, more subtle, symmetry operations — specifically, the C_{2x}, C_{2y}, and C_{4z} rotations and inversion I. To demonstrate the effects of such symmetry operations, we first consider two of the above eight stacking-fault configurations, $[\frac{\pi}{2}^+]$ in Figure 4.6(a) and $[\frac{\pi}{2}^-]$ in Figure 4.6(b). From

Table 4.1: Enumeration of interfacial stacking faults remaining after application of C_{4z} and translational symmetry, labeled by either relative rotation and sign of the bulk regions on opposite sides of the stacking fault (*rotation-sign specifier*) or rotation state of the two reference octahedra (*algebraic specifier*).

Rotation-sign Specifier	Algebraic Specifier
$[0^+]$	$(111 \Longrightarrow 111)$
$[0^-]$	$(111 \Longrightarrow \bar{1}\bar{1}\bar{1})$
$[\frac{\pi}{2}^+]$	$(111 \Longrightarrow \bar{1}11)$
$[\frac{\pi}{2}^-]$	$(111 \Longrightarrow 1\bar{1}\bar{1})$
$[\pi^+]$	$(111 \Longrightarrow \bar{1}\bar{1}1)$
$[\pi^-]$	$(111 \Longrightarrow 11\bar{1})$
$[\frac{3\pi}{2}^+]$	$(111 \Longrightarrow 1\bar{1}1)$
$[\frac{3\pi}{2}^-]$	$(111 \Longrightarrow \bar{1}1\bar{1})$

the figure, these two configurations clearly differ only in the overall choice of sign pattern for the upper layer $\mathfrak{B}$ (□'s). We now use symmetry arguments to demonstrate that these two stacking-fault configurations are actually equivalent, related simply by a C_{2x} rotation.

The general strategy which we shall employ is to exploit the fact that the algebraic specifier not only determines the rotation state of all of the octahedra in the crystal but also transforms in relatively simple ways under the application of symmetry operations to the overall crystal. Figure 4.6(c) illustrates the state of the crystal in Figure 4.6(a) after the application of a C_{2x} symmetry about a *specific* axis. To ensure that the basic crystalline structure maps back onto itself, this axis is chosen to pass at equal distances to the two neighboring AO layers in the stacking fault and through the point immediately above the $O_{\mathfrak{A}}$ reference octahedron (base of the standardized displacement $\mathbf{D}$ in Figure 4.6(a)). The application of C_{2x} effects the following changes to the configuration in Figure 4.6(a):

1. the position of $O_{\mathfrak{A}}$ maps from the bottom layer $\mathfrak{A}$ to the top layer $\mathfrak{B}$ (this changes the central ○ in Figure 4.6(a) into the central □ in Figure 4.6(c));
2. the rotation state of $O_{\mathfrak{A}}$ maps from [111] to $[1\bar{1}\bar{1}]$;
3. the position of the $\mathfrak{B}$-side octahedron (□) in the lower-right quadrant of Figure 4.6(a) maps to the $\mathfrak{A}$-side octahedron (○) in the upper-right quadrant of Figure 4.6(c);
4. the rotation state of this latter octahedron maps from $[1\bar{1}\bar{1}]$ to [111].

To determine the algebraic specifier for the final configuration in Figure 4.6(c), we now identify an octahedron on the lower side of the stacking fault which has

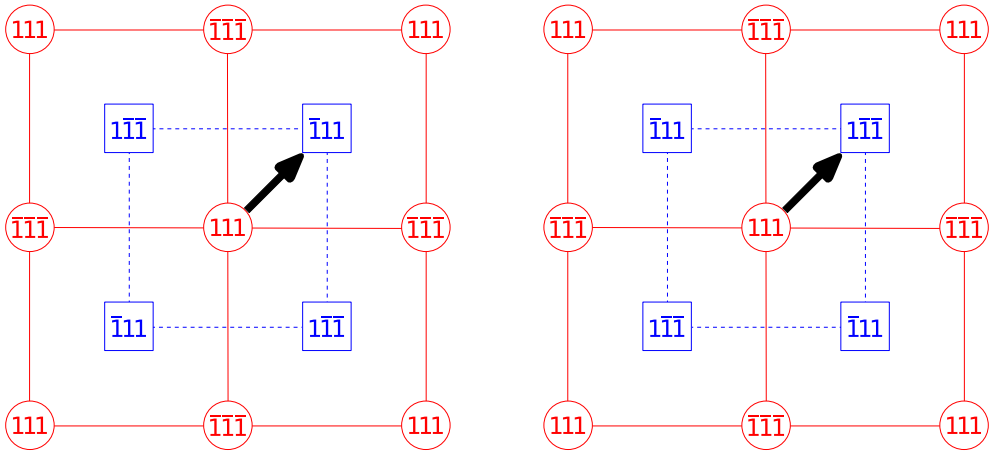

(a) $[\frac{\pi}{2}^{+}]$ (b) $[\frac{\pi}{2}^{-}]$

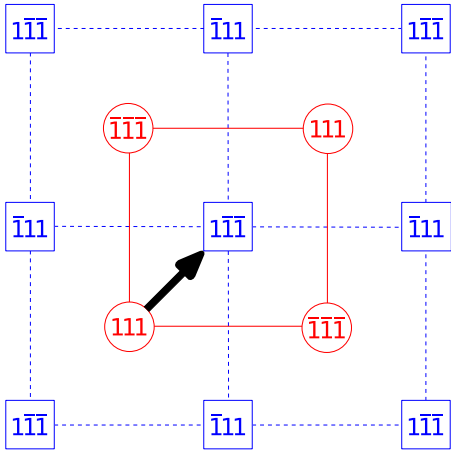

(c) $C_{2x} \circ [\frac{\pi}{2}^{+}]$

Figure 4.6: Full specification of octahedral rotations on opposite sides of stacking fault: octahedra in lower layer $\mathfrak{A}$ (○) and upper layer $\mathfrak{B}$ (□) and standardized displacement $\mathbf{D}$ (⟶), with explicit (signed) $[\pm 1, \pm 1, \pm 1]$ rotation axes to specify full configuration. Panels (a) and (b) depict different configurations, with Panel (c) showing the application of C_{2x} rotation to (a) to produce a configuration equivalent to (b).

a positive rotation from among the (unsigned) $[\pm 1, \pm 1, 1]$ axes (base of the standardized displacement **D** in Figure 4.6(c)). The rotation state of this octahedron, combined with that of the corresponding reference octahedron on the upper side, defines the algebraic specifier for the resulting stacking fault. For this particular case, it is evident from the figure that $C_{2x} \circ [\frac{\pi}{2}^+] = (111 \Longrightarrow 1\bar{1}\bar{1})$. Reference to Table 4.1 then identifies $(111 \Longrightarrow 1\bar{1}\bar{1}) = [\frac{\pi}{2}^-]$, so that $C_{2x} \circ [\frac{\pi}{2}^+] = [\frac{\pi}{2}^-]$, as direct comparison of Figures 4.6(b) and (c) confirms. Thus, we conclude that $[\frac{\pi}{2}^+]$ and $[\frac{\pi}{2}^-]$ are identical and related by the C_{2x} rotation.

To develop an algebra for the action of symmetry operations on arbitrary stacking-fault configurations, we consider the effects of such operations on general stacking-fault configurations, $(abc \Longrightarrow \alpha\beta\gamma)$. For the case of C_{2x}, we note in preparation that the action of C_{2x} on any vector (xyz) is $C_{2x} \circ (xyz) = (x\bar{y}\bar{z})$. Then, as above, the operation of C_{2x} transforms the generic algebraic specifier $(abc \Longrightarrow \alpha\beta\gamma)$ as follows:

1. it swaps abc and $\alpha\beta\gamma$;
2. it maps abc to $a\bar{b}\bar{c}$;
3. it changes the sign of $\alpha\beta\gamma$;
4. it maps $\alpha\beta\gamma$ to $\alpha\bar{\beta}\bar{\gamma}$

In short,

$$C_{2x} \circ (abc \Longrightarrow \alpha\beta\gamma) = (\bar{\alpha}\beta\gamma \Longrightarrow a\bar{b}\bar{c}).$$

Table 4.2 summarizes the effects, similarly determined, on stacking-fault configurations of a number of useful symmetry operations: rotations C_{2x}, C_{2y}, C_{2z}, and C_{4z} and inversion I. (Note that inversion, through the midpoint of the vector connecting the two reference octahedra $O_{\mathfrak{A}}$ and $O_{\mathfrak{B}}$, requires special care: it does not

Table 4.2: Rotation (C) and inversion (I) symmetry operations applied to general stacking-fault configuration.

Symmetry	Algebraic Specifier	
	Original	Final
C_{2x}	$(abc \Longrightarrow \alpha\beta\gamma)$	$(\alpha\bar{\beta}\bar{\gamma} \Longrightarrow \bar{a}bc\,)$
C_{2y}	$(abc \Longrightarrow \alpha\beta\gamma)$	$(\bar{\alpha}\beta\bar{\gamma} \Longrightarrow a\bar{b}c\,)$
C_{2z}	$(abc \Longrightarrow \alpha\beta\gamma)$	$(\,\bar{a}\bar{b}c \Longrightarrow \bar{\alpha}\bar{\beta}\gamma)$
C_{4z}	$(abc \Longrightarrow \alpha\beta\gamma)$	$(\,\bar{b}ac \Longrightarrow \beta\bar{\alpha}\bar{\gamma})$
I	$(abc \Longrightarrow \alpha\beta\gamma)$	$(\alpha\beta\gamma \Longrightarrow abc\,)$

change the direction of pseudo-vectors such as the rotation axes of the different octahedra but simply interchanges the two sides, $\mathfrak{A}$ and $\mathfrak{B}$.)

We are now able to demonstrate further symmetry reduction of the stacking-fault configurations. Table 4.1 lists all eight possible stacking fault configurations, providing both rotation-sign and algebraic specifiers for each. Application of the symmetry operations from Table 4.2 to these configurations, and subsequent translation T by $a_0[100]$ if necessary to make $O_{\mathfrak{A}}$ of rotation state [111], generates the following relationships,

$$T \circ C_{2y} \circ [\tfrac{3\pi}{2}^+] = [\tfrac{3\pi}{2}^-] \tag{4.1a}$$

$$T \circ C_{2x} \circ [\tfrac{\pi}{2}^+] = [\tfrac{\pi}{2}^-] \tag{4.1b}$$

$$C_{4z} \circ I \circ [\tfrac{3\pi}{2}^+] = [\tfrac{\pi}{2}^-]. \tag{4.1c}$$

The above symmetry operations, which each involve interchange of the $\mathfrak{A}$ and $\mathfrak{B}$ sides of the interface, demonstrate equivalence among the set of four stacking faults, $\{[\frac{\pi}{2}^+],\ [\frac{\pi}{2}^-],\ [\frac{3\pi}{2}^+],\ [\frac{3\pi}{2}^-]\}$. Thus, only five unique stacking-fault configurations remain, $[0^+]$, $[0^-]$, $[\frac{\pi}{2}^+]$, $[\pi^+]$, and $[\pi^-]$. Comparison of the algebraic specifiers of these five configurations, from Table 4.1 above, with the computer-generated distorted phases listed as Nos. 18–22, in Table III of Hatch et al.[71], confirms that our result is consistent with theirs, though theirs is limited to the $n = 1$ RP phase. We confine ourselves to discussion of these five unique configurations for remainder of this work.

4.3.2 RP phases

The RP phases, which we study in this work, consist of periodic arrays of the above configurations of stacking faults. While constructing such arrays from in-

dividual stacking faults, the array periodicity may be maintained either through simple alternating patterns of bulk regions ($\mathfrak{A}/\mathfrak{B}/\mathfrak{A}/\mathfrak{B}$ sequencing) or through more complex, and possibly lower-energy, patterns (for example, $\mathfrak{A}/\mathfrak{B}/\mathfrak{C}/\mathfrak{A}/\mathfrak{B}/\mathfrak{C}$ sequencing).

Immediately below, we demonstrate that, in fact, an $\mathfrak{A}/\mathfrak{B}/\mathfrak{A}/\mathfrak{B}$ sequence of bulk regions always corresponds to repetition of the same type of stacking-fault configuration. Three very compelling reasons then follow for studying RP phases with this type of periodicity. First, one should expect the preferred RP phase to consist of a sequence of stacking faults, which are *all* of the lowest-energy configuration; this would then naturally correspond to an $\mathfrak{A}/\mathfrak{B}/\mathfrak{A}/\mathfrak{B}$ sequence. Second, actual experiments find superlattice sizes consistent with small, simple repeat units[49, 52, 99]. Finally, isolated stacking faults are also observed under certain conditions[49], and the study of RP phases of $\mathfrak{A}/\mathfrak{B}/\mathfrak{A}/\mathfrak{B}$ periodicity, containing two identical faults in each primitive unit cell, then allows for the extraction of the behavior of individual isolated faults.

To establish that an $\mathfrak{A}/\mathfrak{B}/\mathfrak{A}/\mathfrak{B}$ sequence of bulk regions corresponds to repetition of the same configuration of stacking fault, we must prove the equivalence of the two stacking faults, $(\mathfrak{A}/\mathfrak{B})$ and $(\mathfrak{B}/\mathfrak{A})'$, in such an RP phase. As in Section 4.3.1, we take the algebraic specifier for this first stacking fault $(\mathfrak{A}/\mathfrak{B})$ to be the generic $(abc \Longrightarrow \alpha\beta\gamma)$ where abc and $\alpha\beta\gamma$ refer to the rotation states of the two reference octahedra for this fault, $O_{\mathfrak{A}}$ and $O_{\mathfrak{B}}$ respectively. We must then choose two corresponding reference octahedra $O'_{\mathfrak{A}}$ and $O'_{\mathfrak{B}}$ for the second stacking fault $(\mathfrak{B}/\mathfrak{A})'$. Since $\mathbf{D} \equiv -\mathbf{D}$, we can set $O'_{\mathfrak{A}} = O_{\mathfrak{A}} + (n-1)\zeta a_0 \hat{e}_3$ and $O'_{\mathfrak{B}} = O_{\mathfrak{B}} + (n-1)\zeta a_0 \hat{e}_3$, where n is the number of the RP phase ($\mathrm{A}_{n+1}\mathrm{B}_n\mathrm{O}_{3n+1}$) so that $n-1$ layers of material separate $O_{\mathfrak{A}}$ from $O'_{\mathfrak{A}}$ and similarly separate $O_{\mathfrak{B}}$ from $O'_{\mathfrak{B}}$. (Consideration of

the $n = 1$ case should make this apparent.) The alternating octahedral rotations of this $a^-a^-a^-$ Glazer system thereby define the algebraic specifier for the $(\mathfrak{B}/\mathfrak{A})'$ stacking fault as $(\,(-1)^{n-1}(\alpha\beta\gamma) \Longrightarrow (-1)^{n-1}(abc)\,)$. However, displacement of the arbitrary origin (reference octahedra) by $a_0[100]$, for cases when n is even, generates an equivalent algebraic specifier for this $(\mathfrak{B}/\mathfrak{A})'$ interface which is now insensitive to n, $(\alpha\beta\gamma \Longrightarrow abc)$. Finally, we apply inversion symmetry, as introduced in Table 4.2, to this $(\mathfrak{B}/\mathfrak{A})'$ stacking fault, $I \circ (\alpha\beta\gamma \Longrightarrow abc) = (abc \Longrightarrow \alpha\beta\gamma)$, and thus prove that the $(\mathfrak{A}/\mathfrak{B})$ stacking fault is equivalent to the $(\mathfrak{B}/\mathfrak{A})'$ fault.

Lastly, since all stacking faults in an $\mathfrak{A}/\mathfrak{B}/\mathfrak{A}/\mathfrak{B}$ RP phase always possess equivalent configurations, we can uniquely label these RP phases using the same rotation-sign specifiers established above for the five symmetry-distinct stacking faults: $[0^+]$, $[0^-]$, $[\frac{\pi}{2}^+]$, $[\pi^+]$, and $[\pi^-]$.

4.4 Model and computational methods

4.4.1 Shell potential

As discussed in Section 4.2 above, to study the generic behavior of $a^-a^-a^-$ perovskites which form RP phases, we employ a shell-potential model[100] parameterized for strontium titanate[101]. Shell-potential models are formulated as an extension to ionic pair potentials and employed to capture the polarizability of the atomic constituents. The shell model separates each ion into two parts, a core and an outer shell, which possess individual charges that sum to the nominal charge of the ion. The total model potential U consists of three terms,

$$U \equiv U_P + U_C + U_B, \tag{4.2}$$

representing, respectively, the polarizability of the ions, and the Coulomb and short-range interactions among the ions. The polarizability is captured by harmonic springs connecting the core and shell of each ion, so that U_P has the form,

$$U_P = \tfrac{1}{2} \sum_i k_i \left|\Delta r_i\right|^2, \tag{4.3}$$

where $|\Delta r_i|$ is the core-shell separation for ion i and the k_i are a set of ion-specific spring constants. The Coulomb contributions take the form,

$$U_C = \tfrac{1}{2} \sum_{i,j}{}' \frac{k_c q_i q_j}{r_{ij}}, \tag{4.4}$$

where i and j range over all cores and shells (excluding terms where i and j refer to the same ion), q_i and q_j are the corresponding charges, r_{ij} is the distance between the charge centers, and k_c is Coulomb's constant. Finally, the short-range interactions are included through a sum of Buckingham[102] pair potentials (which can be viewed as combinations of Born-Mayer[103] and Lennard-Jones[104] potentials) of the form,

$$U_B = \tfrac{1}{2} \sum_{i,j} \left(A_{ij} e^{-r_{ij}/\rho_{ij}} - C_{ij} r_{ij}^{-6} \right), \tag{4.5}$$

where i and j range over *all shells* and A_{ij}, ρ_{ij}, and C_{ij} are pair-specific adjustable parameters. Here, the first term (Born-Mayer) serves as a repulsive short-range interaction to respect the Pauli exclusion principle, and the second term (Lennard-Jones) models the dispersion or van der Waals interactions[105]. The specific electrostatic and short-range shell-model parameters used in this study were fit to strontium titanate by Akhtar et al.[101], with values as listed in Tables 4.3 and 4.4. Finally, we wish to emphasize again, as it is rarely mentioned explicitly in the shell-potential literature, that the pair-potential terms in U_B apply to the *shells only*, and *not* to the cores.

Shell models have been extensively used for decades as the primary empirical potential for modeling perovskites and other oxides[106, 107]. We tested the

Table 4.3: Electrostatic shell-model potential parameters used in this study (from Akhtar et al.[101]).

Ion	Shell Charge [e]	Core Charge [e]	Spring Constant [$\mathrm{eV \cdot Å^{-2}}$]
Sr^{2+}	1.526	0.474	11.406
Ti^{4+}	−35.863	39.863	65974.0
O^{2-}	−2.389	0.389	18.41

Table 4.4: Short-range shell-model potential parameters used in this study (from Akhtar et al.[101]).

Interaction	A [eV]	ρ [Å]	C [eV $\cdot$ Å^6]
$Sr^{2+} \Leftrightarrow O^{2-}$	776.84	0.35867	0.0
$Ti^{4+} \Leftrightarrow O^{2-}$	877.20	0.38096	9.0
$O^{2-} \Leftrightarrow O^{2-}$	22764.3	0.1490	43.0

correctness of our coded implementation of this potential through comparisons of lattice constants and elastic moduli without the AFD reconstruction and find excellent agreement. For instance, using the same shell potential and the same non-reconstructed ground state, we predict a volume per $SrTiO_3$ chemical unit of 59.18 Å^3, which is within 0.4% of the value calculated by Akhtar et al.[101] For the elastic moduli, we find $C_{11} = 306.9$ GPa, $C_{12} = 138.7$ GPa, and $C_{44} = 138.8$ GPa, which are within 1.8%, 1.0%, and 0.7%, respectively, of the values from Akhtar et al.[101] From this, we conclude that our implementation of the potential is correct. We also would like to note that, when the $a^-a^-a^-$ reconstruction is considered, significant changes occur, and we find, instead, a volume per $SrTiO_3$ chemical unit of 58.49 Å^3 and elastic moduli of $C_{11} = 275.6$ GPa, $C_{12} = 144.3$ GPa, and $C_{44} = 133.5$ GPa. This underscores the importance of considering AFD reconstructions when constructing such potentials.

4.4.2 Numerical methods

In this work, we compute the Coulombic interaction[108] from (4.4) using a Particle Mesh Ewald algorithm[109–111] with all real-space pair-potential terms computed out to a fixed cutoff distance using neighbor tables. Analytic derivatives are used to determine the forces on the cores and shells within the supercell, and finite differences are used to compute the generalized forces on the superlattice vectors. While such finite-difference methods occasionally introduce issues with numerical precision into the resulting calculations, we are able to mitigate such effects with care in selection of the finite-difference step, scaling it proportionally to the sizes of the lattice vectors involved.

With the gradients determined as above, we relax each system using the tech-

nique of preconditioned conjugate gradient minimization[112] (specifically, the Polak-Ribière[113] method), fully optimizing the ionic coordinates in an inner loop of the routine and then optimizing the lattice vectors in an outer loop. The preconditioner applies only to the ionic relaxation of this procedure and scales the generalized force on the geometric center of each ion (mean position of the core and shell) separately from the generalized force on the core-shell displacement, with the latter scaled in inverse proportion to the spring constant of the corresponding ion. This process ensures that all supercell energies are relaxed with respect to both ionic and lattice coordinates to a precision of $\sim$0.3 μeV per supercell.

4.4.3 Ground state

To establish the ground state of the model potential used in our calculations, we have carried out what we regard as a thorough, but not exhaustive, search for a *probable* ground-state structure. Indeed, we have found no alternative structure which relaxes to an energy less than our candidate ground-state structure within our potential. We performed quenches on hundreds of random displacements from the idealized positions of the $1\times1\times1$ primitive unit cell to explore various potential reconstructions for supercells up to $6\times6\times6$. We also considered a number of highly ordered configurations commensurate with antiferrodistortive disordering.

Among those minima which we explored, we selected the lowest-energy configuration to serve as the bulk crystalline state throughout this study. This configuration possesses a fairly regular pattern as depicted in Figure 4.2, namely each oxygen octahedron rotates slightly along trigonal directions in a cell-doubling, alternating three-dimensional $2 \times 2 \times 2$ checkerboard pattern, which is precisely the desired $a^-a^-a^-$ Glazer system from Section 4.2. We also find that the lattice vectors as-

sume the rhombohedral symmetry (illustrated in Figure 4.3)commonly found in $a^-a^-a^-$ perovskites, with the cubic lattice stretching along the same trigonal axes about which the octahedra rotate.

The specific lattice vectors which we find for the $2\times2\times2$ reconstructed supercell of our model are the columns of the following matrix,

$$\mathbf{R} = \begin{pmatrix} 7.764 & 0.028 & 0.028 \\ 0.028 & 7.764 & 0.028 \\ 0.028 & 0.028 & 7.764 \end{pmatrix} \text{Å}.$$

4.4.4 Construction of RP supercells

Our construction of initial ionic configurations for the $A_{n+1}B_nO_{3n+1}$ RP phases proceeds through a detailed process defined in Section 4.3. As discussed there, we carefully consider a large number of combinatorial possibilities resulting from the different geometries due to the aforementioned $2 \times 2 \times 2$ cell-doubling, $a^-a^-a^-$ bulk reconstruction. We construct each configuration of the RP phase by stacking $2n$ layers of bulk perovskite along the [001] direction, with the two stacking faults (excess AO (001) planes) so situated as to equally divide the supercell into two bulk slabs, each with n layers and potentially different $a^-a^-a^-$ reconstructions. Relative to each other, these bulk slabs are also laterally displaced by one of the four (equivalent) $\frac{a_0}{2}[\pm1, \pm1, 0\,]$ vectors at each stacking fault. We perform this procedure to create all eight ($111 \Longrightarrow \alpha\beta\gamma$) configurations from Section 4.3.1, through combinations of reconstructions in the two bulk slabs, for RP phases from $n = 1 \ldots 30$, containing from 56 to 1216 ions, respectively. Each RP superlattice system is then fully relaxed, as described above, both in terms of internal ionic coordinates and lattice vectors, until the energy is minimized to within a precision

of ∼0.3 μeV. In all cases, we find that the material on either side of the stacking fault maintains a uniform bulk reconstruction throughout, so that the enumeration of Section 4.3.1 is suitably complete. Finally, we test for meta-stability by creating ensembles of 20–250 samples for each configuration of octahedra rotations for all RP phases up to $n = 10$, introducing root-mean-square displacements of 0.001 Å for each coordinate axis of every core and shell, and quenching each of these randomized systems.

4.5 Results

As described in Section 4.2 above, the results obtained below have been computed with the standard shell-potential model for strontium titanate[101, 106, 107], but are interpreted to represent the generic behavior of an antiferrodistortive perovskite (ABO_3) from among the class of perovskites within the $a^-a^-a^-$ Glazer system which form RP phases.

4.5.1 Formation of RP phases

After constructing the various possible RP phases according to the prescription in Section 4.4.4, the ideal procedure for determining the energetics of the RP phases is to fully relax each system, in terms of *both* internal atomic coordinates *and* superlattice vectors, without any externally imposed symmetries. The energies of the reference bulk materials, perovskite (ABO_3) and A-oxide (AO), should also be fully relaxed in the same sense.

Without full relaxation of lattice vectors for both the RP phases and bulk

reference cells, any attempts to extract energies will introduce significant errors that scale in proportion to the amount of bulk material between stacking faults. (Such failures to fully relax the lattice vectors might arise due to expediency in *ab initio* studies or through attempts to simulate higher-temperature phases by imposing a higher-temperature lattice structure while relaxing ionic coordinates.)

Figure 4.7(a) shows actual results obtained from such a methodologically flawed procedure, where the energy needed to form the RP phase from the bulk perovskite ABO_3 and bulk A-oxide AO, $E_{A_{n+1}B_nO_{3n+1}} - n \cdot E_{ABO_3} - E_{AO}$, is computed without full relaxation of the lattice vectors of the RP phase, but instead with the enforcement of tetragonal lattice vectors associated with a higher-temperature symmetry not possessed by the ground state of our model. Under these constraints, the energy exhibits a clear linear *increase* with n, the amount of bulk material between stacking faults, due to an inflated RP-phase energy associated with artificial strain in the bulk regions. (Note that the results in the figure are visually indistinguishable whether or not one allows the perovskite or A-oxide bulk reference cells to fully relax.) Figure 4.7(b) shows results obtained where the lattice vectors of the RP phases are allowed to relax fully but the lattice vectors of the bulk reference cells are not. In this case, excess bulk energy is not included in the RP cell but instead in the bulk reference cells, and the energy of formation now *decreases* linearly with n. Either type of error will confound the extraction of meaningful information on the RP phases. The calculation of such phases is herein seen to be quite delicate, a fact which only becomes obvious for calculations with large values of n.

Figure 4.8 presents the results, properly calculated with full relaxation of all lattice vectors, for the energies of all eight ($111 \Longrightarrow \alpha\beta\gamma$) stacking-fault configurations of our model potential, relative to the corresponding amounts of the fully

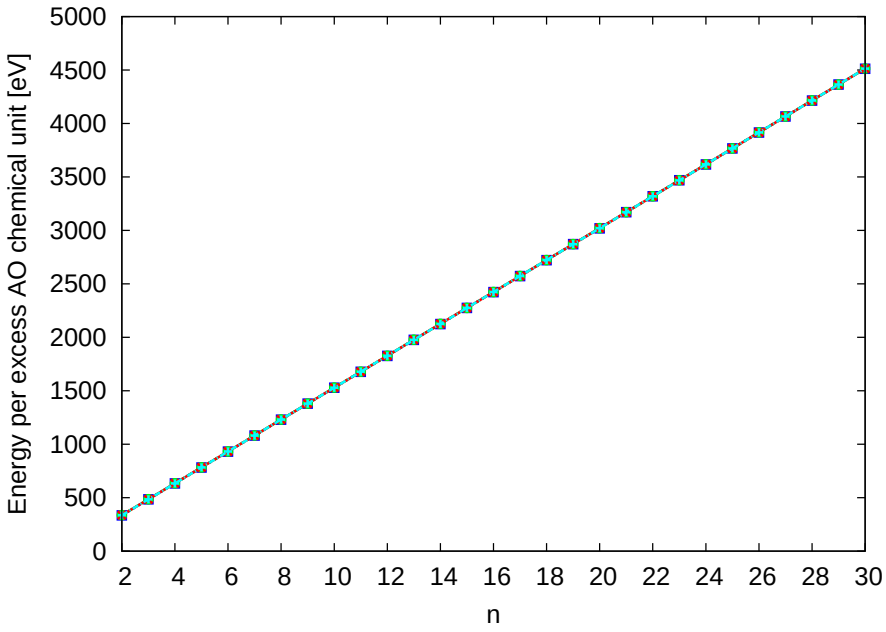

(a)

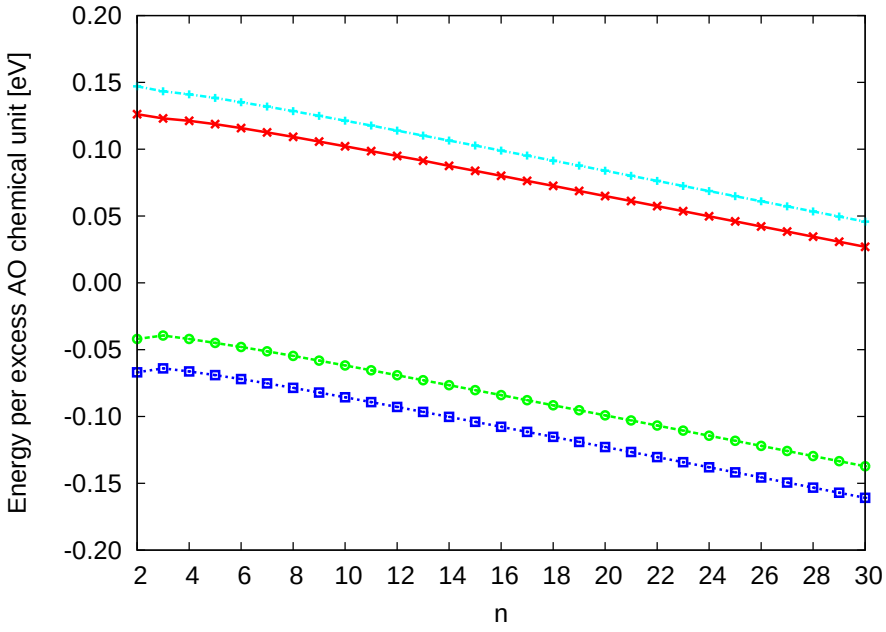

(b)

Figure 4.7: Formation energies of RP phases per excess AO chemical unit as a function of n for various members of homologous series $A_{n+1}B_nO_{3n+1}$: methodological error of employing (a) tetragonal supercells for RP phases or (b) fully relaxed supercells for RP phases but unrelaxed lattice vectors for bulk reference cells. Each panel shows results for the distinct stacking-fault configurations corresponding to different arrangements of octahedral rotations, as enumerated in the text (Section 4.3.1).

relaxed, reconstructed perovskite and the fully relaxed A-oxide material. As in the examples above, the energies are expressed per excess AO chemical unit, $2 \times 2 = 4$ of which appear in each reconstructed RP superlattice unit cell (and $2 \times (2 \times 2) = 8$ of which appear in each supercell with two stacking faults and thus two RP superlattice unit cells). The final relaxed RP configurations indeed are not distinct, as expected from the symmetry arguments in Section 4.3.1, which showed that $[\frac{\pi}{2}^+] \equiv [\frac{\pi}{2}^-] \equiv [\frac{3\pi}{2}^+] \equiv [\frac{3\pi}{2}^-]$, so that there should be at most five different configurations. Somewhat unexpectedly, rather than displaying five separate curves for the five symmetry-distinct configurations ($[0^+]$, $[0^-]$, $[\frac{\pi}{2}^+]$, $[\pi^+]$, $[\pi^-]$), Figure 4.8 instead shows only four curves: we find that the $[\frac{\pi}{2}^+]$ configuration is unstable and relaxes directly to the $[\pi^-]$ configuration, as determined by energy calculations and observations of transitions in lattice symmetries for each configuration during full relaxation. Additionally, the $[0^-]$ configuration appears meta-stable, often transitioning, upon small perturbations described in Section 4.4.4, to the $[0^+]$ configuration. The remainder of this discussion thus only reports on the behavior of the final three distinct, stable configurations ($[0^+]$, $[\pi^+]$, $[\pi^-]$) as well as the one additional distinct, meta-stable configuration ($[0^-]$).

From Figure 4.8, we note immediately that, depending upon the relative rotational orientation of oxygen octahedra on either side of the stacking faults, the configurations separate into two groupings, one with positive energy and one with negative energy relative to phase separation into bulk perovskite and bulk A-oxide. The energy scales associated with the different configurations may thus be sufficient to either stabilize or destabilize the formation of an RP phase.

Moreover, for our model potential, the two more stable stacking-fault configurations ($[0^+]$ and $[\pi^-]$) possess negative energies for all n, providing the first

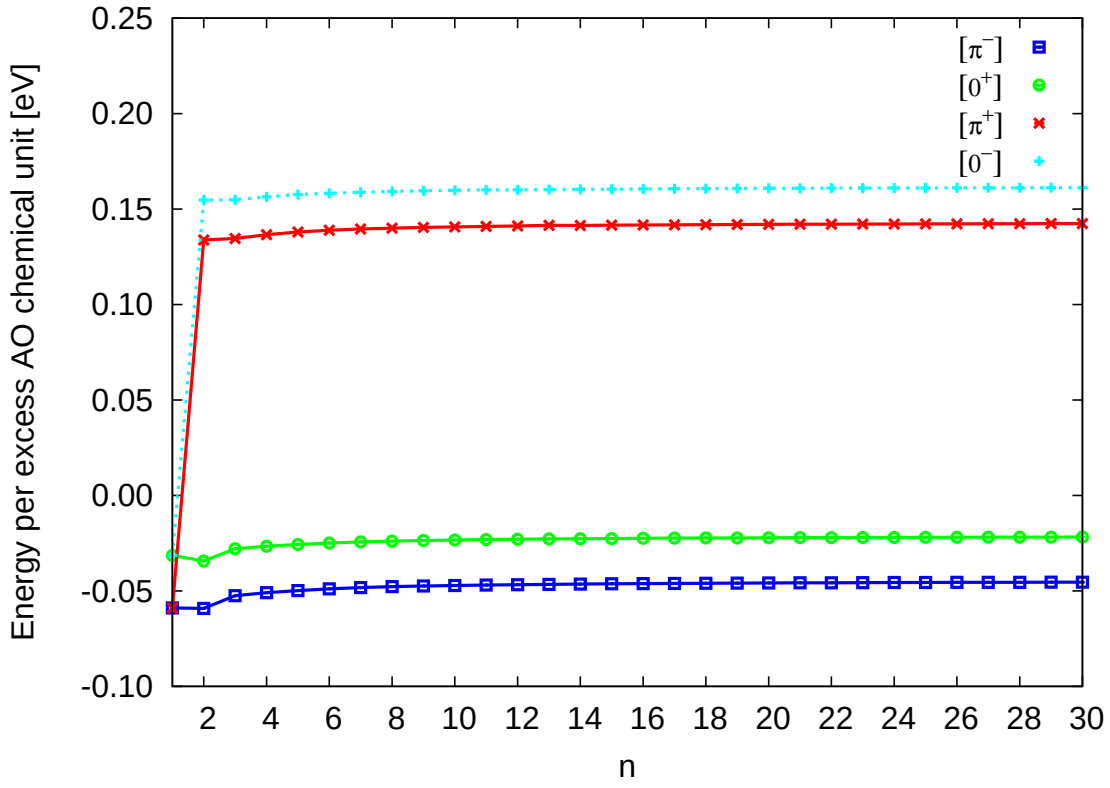

Figure 4.8: Formation energies of RP phases per excess AO chemical unit as a function of n for various members of homologous series $A_{n+1}B_nO_{3n+1}$: labeled curves represent each of the stable stacking-fault configurations corresponding to different arrangements of octahedral rotations, as enumerated in the text (Section 4.3.1). Results calculated using fully relaxed ionic *and* lattice coordinates for both RP phases and bulk references.

demonstration that RP phases can be favored over formation of bulk perovskite and A-oxide for *all* values of n. Also, we find the $[\pi^-]$ configuration to be favored over all other possible configurations in our model, regardless of the value of n.

It is also immediately apparent that the RP phases for $n = 1$ deserve special consideration for our model potential. The $n = 1$ phases for the two configurations with positive energy collapse to related $n = 1$ configurations with negative energy, with $[\pi^+]$ becoming $[\pi^-]$ and $[0^-]$ becoming $[0^+]$. This might be related to the realization that the full $2 \times 2 \times 2$ reconstruction cannot be expressed on either side of the stacking fault for an $n = 1$ RP phase, and thus these higher-energy configurations forfeit some stability for the $n = 1$ RP phase.

The magnitude of the energy differences between configurations is not only sufficient to affect the stability of the phases, but is also significant compared to thermal energy scales. For instance, we find the separation between the stable and unstable groupings to be ∼200 meV per excess AO chemical unit (or ∼800 meV per RP superlattice unit cell, $(2 \times 2) \cdot A_{n+1}B_nO_{3n+1}$). To place this energy in context, we can also consider the energy per interfacial oxygen octahedron (one on the top and bottom of the stacking fault for each excess AO chemical unit), ∼100 meV, which is about ∼30 meV per configurational (rotational) degree of freedom. This is larger than, but comparable to, the thermal energy at room temperature, 26 meV, so that at significant temperatures we still can expect a small, but statistically noticeable, tendency for the stacking fault to preferentially select the minimal energy configuration over other disfavored configurations.

This energy scale is also significantly larger than the energy scales we might expect for excitations in the bulk of the material. For instance, the structural phase transition in strontium titanate (the material to which the original model actually

had been fit[101]) occurs near 105 K[92], which corresponds to an energy scale of 9 meV. To further place the above ∼30 meV interfacial energy scale in context, we consider the energies within our model of two alternate rotational $2 \times 2 \times 2$ bulk reconstructions, those with rotations about $\langle 110 \rangle$ axes (orthorhombic) and $\langle 100 \rangle$ axes (tetragonal), finding rotational energy scales of 4 meV and 16 meV, respectively, relative to the ground-state reconstruction. These comparisons lead to the intriguing conjecture that, for some perovskites with low densities of stacking faults (high n), there exist a range of temperatures above the bulk structural phase transitions, in which the bulk rotational energy scale is insufficient to constrain the rotations of the octahedra, while the interfacial energy scale is suitable to constrain the octahedral rotations to specific preferred orientations. This corresponds to a picture of "fuzzy" octahedra in the bulk regions with noticeable orientational preferences remaining for the octahedra at the stacking faults. Alternatively, for perovskites in RP phases with low values of n and higher densities of stacking faults, one might expect this increased energy scale to raise the transition temperature associated with octahedral rotations.

4.5.2 Stacking fault interactions and intergrowth formation

While Section 4.5.1 discussed the relationship among energies of formation of different configurations, it is further instructive to examine the energy and behavior of each configuration independently, as a function of separation between stacking faults. Figure 4.9 plots the interaction energies per excess AO chemical unit for each configuration, which, for a given configuration, are the formation energies of each phase *relative* to the energy of its $n = 2$ phase. (For the two stable, low-energy configurations within our model, the $n = 2$ phase is, in fact, lowest in energy,

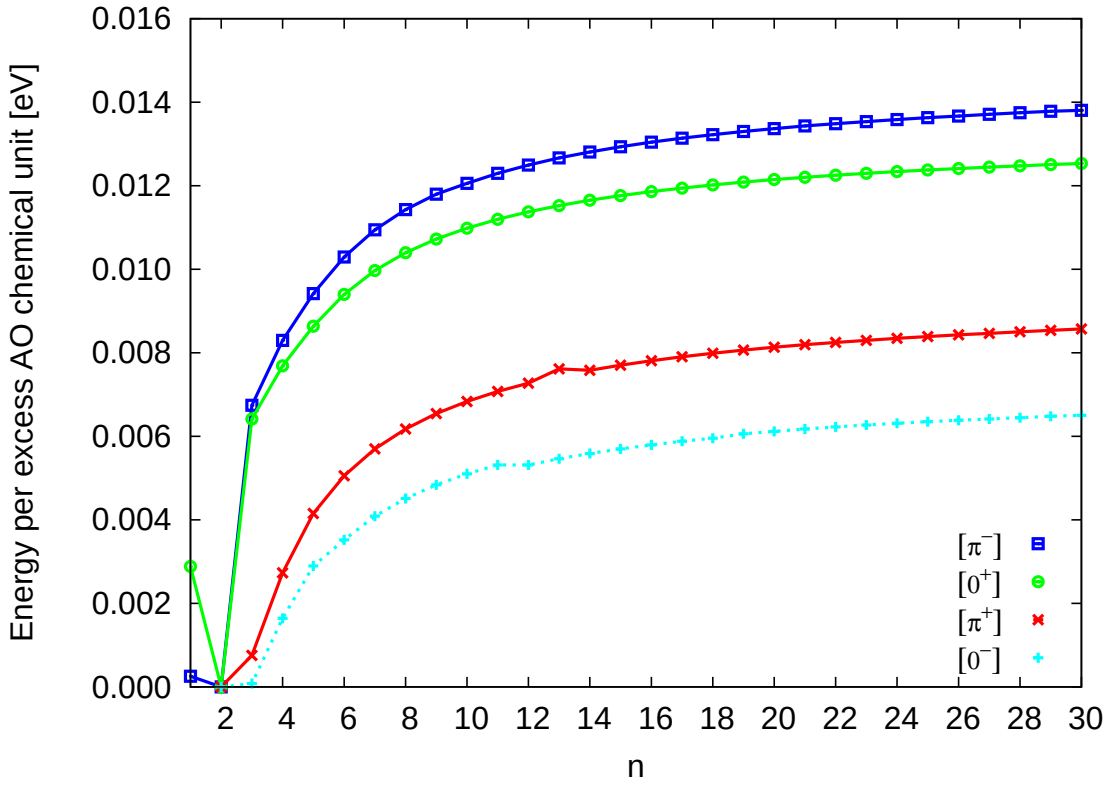

Figure 4.9: Interaction energies among stacking faults (formation energies relative to $n = 2$ RP phase) per excess AO chemical unit as a function of n for the homologous series $A_{n+1}B_nO_{3n+1}$ (same notations as in Figure 4.8). Data depict relatively weak, but consistently attractive, interactions in all cases.

so that this plot represents the binding energies of the stacking faults for these configurations. For the two high-energy configurations, unstable to dissociation into separate regimes of bulk perovskite and A-oxide, the $n = 1$ phase is actually lowest in energy, so that this plot approximately represents the binding energies of the stacking faults.) For our model, in all cases, there is a relatively weak, but consistently attractive, interaction (apart from special cases for $n = 1$), varying by over a factor of two from ∼7–14 meV per excess AO chemical unit, depending upon the stacking-fault configuration. The strengths of the interaction occur in precisely the same sequence as the stability of the configurations, with the more attractive interactions occurring in the more stable configurations.

Within the current model, the universally attractive and eventually asymptotic nature of the interaction for $n \geq 2$ leads to a set of interaction energies with *downward* curvature. The standard secant construction for mixed phases then indicates that, for $n > 2$, the energy of a system can always be lowered by forming a so-called "intergrowth" phase, mixing regions of lower- and higher-n phases (i.e., non-uniformly changing the separation between stacking faults that define the phases) while maintaining a consistent average stoichiometry. To understand how this arises from the particular form of these interactions, note that changing the location of a particular fault (in a uniform $n > 2$ phase) decreases the distance to one of its neighboring faults but increases the distance to the other neighboring fault. The downward curvature of the interaction energy, however, ensures that the energy gain from the decreased distance more than compensates for the cost from the increased distance, so that the overall energy is lowered by varying the distances between faults.

Finally, we consider the possibility of intergrowth phenomena. The two higher-

energy configurations within our model are unstable with respect to dissociation into intergrowths of bulk perovskite and bulk A-oxide, and thus need not be considered further here. To examine the possibility of intergrowths in the two lower-energy configurations, we consider environments both with a relatively low density (high n) of stacking faults and those with a higher density (lower n) of stacking faults. In the former case, the stacking faults attract to form dense phases at the value of n for which the energy is minimized, namely $n = 2$ within our model, alternating with regions of bulk perovskite. In the latter case, the additional A-oxide exceeds the concentration required for creation of a consistent phase at the preferred minimum energy $n = 2$ value. For the stoichiometry such that $1 < n < 2$ on *average* throughout our model system, the excess A-oxide could either form intergrowths consisting of the $n = 2$ phase and bulk A-oxide or intergrowths consisting of $n = 2$ and $n = 1$ phases. The creation of $n = 1$ phases, by insertion of excess AO planes, corresponds to the transformation of a given unit of the $n = 2$ phase into two units of the $n = 1$ phase. Since twice the formation energy of the $n = 1$ phase is always lower than the formation energy of the $n = 2$ phase within our model, we recognize that, for stoichiometries with $1 < n < 2$ on average, the two stable configurations ($[0^+]$ and $[\pi^-]$) will always form intergrowths of $n = 1$ and $n = 2$ phases, rather than of bulk A-oxide and $n = 2$ phase. For RP phases with yet higher concentrations of species A ($n < 1$), a similar argument shows that, within our model, intergrowths form between the $n = 1$ RP phase and bulk A-oxide.

4.5.3 Isolated stacking faults

Although the stacking faults are attractive in our particular model, crucial early growth experiments on RP phases often observed these stacking faults in isolation[49], perhaps due to kinematic constraints. Here, we consider the physical properties of such isolated faults.

To extract the behavior of isolated stacking faults at infinite separation, we first determine the functional dependence of the interaction on the separation between stacking faults. Figure 4.10 shows the interaction energies of the stacking faults from Figure 4.9, now plotting these energies as a function of $1/n$, where n measures the separation between stacking faults in terms of the number of intervening bulk layers. The data in this figure exhibit clear linear behavior, indicating that the interaction is inversely proportional to fault separation. The ordinate intercepts ($1/n \to 0$, or $n \to \infty$) denote the energy released per excess AO chemical unit when stacking faults bind together into RP phases at their most energetically favored value of n (for the two stable configurations within our model, $[0^+]$ and $[\pi^-]$, with energy minima at $n = 2$).

Table 4.5 summarizes the values of these binding energies per excess AO chemical unit, as determined by linear least-square fits to the energies for RP phases in Figure 4.10, ignoring in each case the three smallest separations ($n \leq 3$) which clearly involve significant higher-order interactions. Even for the most attractive configuration ($[\pi^-]$), our model shows a $\sim$7 meV binding energy per octahedron neighboring the stacking fault (recall that there are two interfacial octahedra for each excess AO chemical unit, one on either side of the stacking fault), which is relatively low compared to room temperature, a fact which may be related to the observation of isolated faults in some materials.

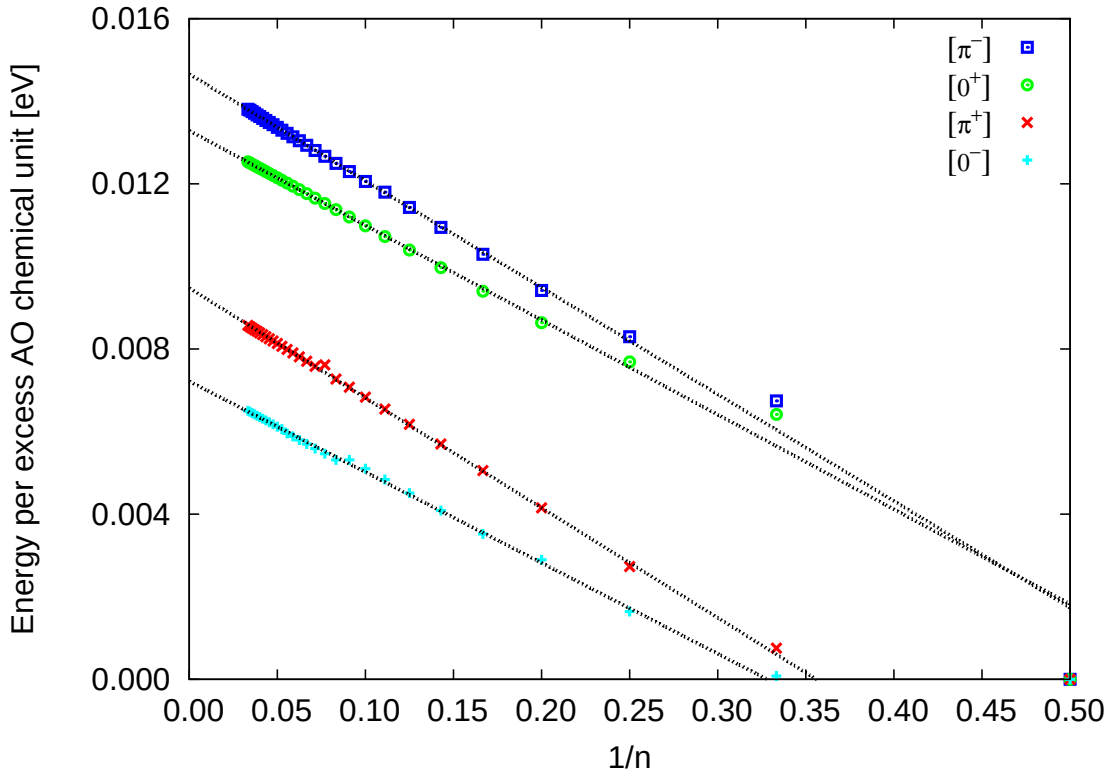

Figure 4.10: Interaction energies among stacking faults (formation energies relative to $n = 2$ RP phase) per excess AO chemical unit as a function of $1/n$ for the homologous series $A_{n+1}B_nO_{3n+1}$: extraction of energies to infinite superlattice size (dotted lines) to determine binding energies of stacking faults. Linear behavior indicates an inverse-distance interaction between stacking faults.

Table 4.5: Binding energies of stacking faults per excess AO chemical unit for different configurations.

Configuration	Binding Energy [meV]
$[0^-]^\dagger$	7.218
$[\pi^+]$	9.476
$[0^+]$	13.288
$[\pi^-]$	14.658

† Meta-stable

With the form of the interaction now determined, we turn to the formation energies of isolated stacking faults in their various configurations. We can now finally determine whether these different configurations have a large effect on formation energies of RP phases, as Section 4.5.1 suggests. Figure 4.11 shows the formation energy per excess AO chemical unit as a function of $1/n$.

Here, the ordinate intercepts give the energy to incorporate an AO chemical unit into an isolated, excess AO plane in perovskite relative to that chemical unit appearing in bulk A-oxide. Table 4.6 summarizes the formation energies of isolated stacking faults as determined by the same type of linear least-square fit used to extract the binding energies above. Within our model, we again find significant differences in formation energies between the two groupings of configurations (those with positive and negative energies), of up to $\sim$200 meV per excess AO chemical unit or $\sim$100 meV per oxygen octahedron neighboring the stacking fault. We also identify a much smaller energy difference between the two lowest-energy configurations (those with negative energies) of 23.5 meV per excess AO chemical unit, or 11.8 meV per octahedron. Following a similar argument as in Section 4.5.1, for a range of temperatures above the bulk phase transitions, we may still find that octahedra near isolated stacking faults are constrained to a subset of low-energy rotational orientations, while those in the bulk fluctuate among all possible rotations.

Finally, comparing the results in Table 4.6 with those in Table 4.5, we come to the commonsensical, though not logically necessary, result that the sequence of stacking faults from the most stable (i.e., lowest formation energy) to the least stable, directly corresponds to the sequence of binding strengths, from the strongest attraction to the weakest. We also propose a simple physical mechanism for dif-

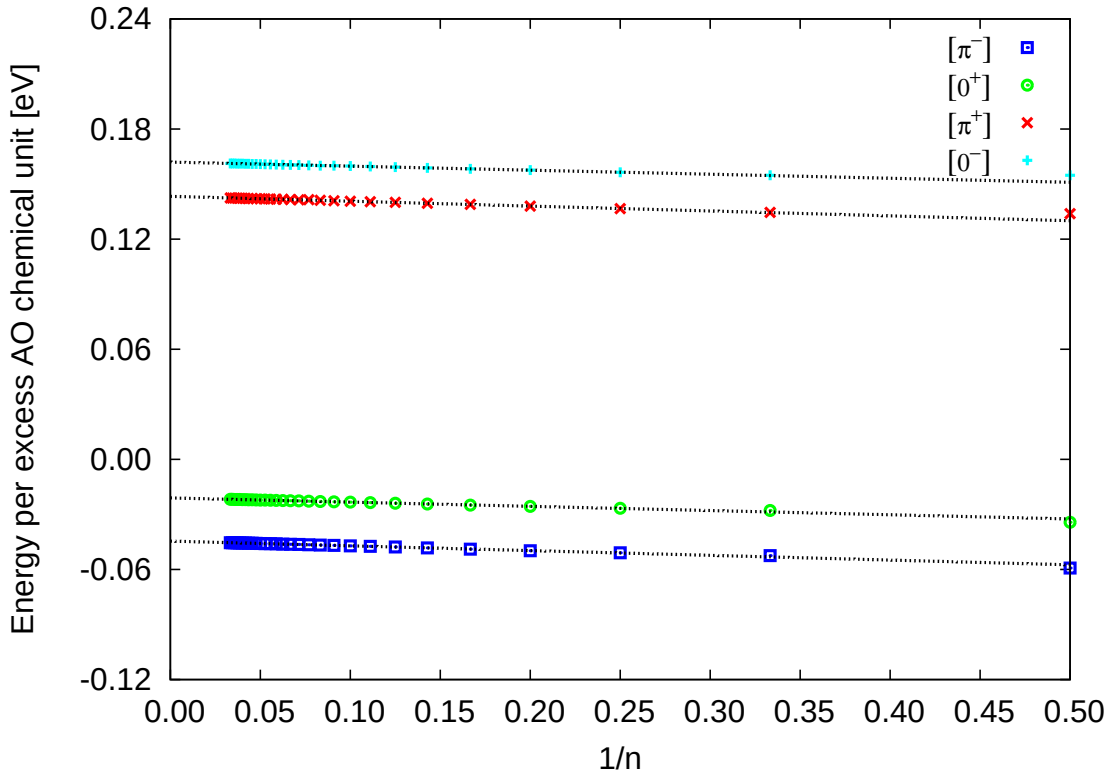

Figure 4.11: Formation energies of RP phases per excess AO chemical unit as a function of $1/n$ for the homologous series $A_{n+1}B_nO_{3n+1}$: extraction of energies to infinite superlattice size (dotted lines) to determine formation energies of isolated stacking faults.

Table 4.6: Formation energies of isolated stacking faults per excess AO chemical unit for different configurations.

Configuration	Formation Energy [meV]
$[0^-]^{\ddagger}$	162.0
$[\pi^+]$	143.3
$[0^+]$	−21.0
$[\pi^-]$	−44.5

‡ Meta-stable

ferentiating between higher and lower energies of formation for the configurations, potentially reflecting their stability relative to phase separation into bulk perovskite and bulk A-oxide. Figure 4.12 depicts the planar movement of oxygens in the AO layers on opposite sides of the stacking fault. The sense of rotation of the interfacial octahedra drives constituent oxygen ions to move in specific patterns within their respective AO layers along the stacking fault. For the high-energy configurations, $[0^-]$ or $[\pi^+]$, the interfacial oxygen ions from opposite AO layers are displaced toward each other, despite their natural Coulombic repulsion, as in Figure 4.12(a). For the low-energy configurations in Figure 4.12(b), $[0^+]$ or $[\pi^-]$, the same oxygen ions move past each other along the interface, tending to lessen the approach of like-charged ions toward one another and thus minimizing the energy. Thus, we find that the stability of different stacking-fault configurations can be readily understood in terms of simple Coulombic effects.

4.5.4 Point defects

With the energies of the various RP phases now determined, we are finally in a position to substantiate the claim that, in A-rich stoichiometries of ABO_3, the RP phases are preferred over the formation of point defects.

Interstitials in perovskites are known to be energetically very unfavorable[30]. On the other hand, A-rich stoichiometries can be understood by noting that the addition of an AO chemical unit is identical to the incorporation of a bulk ABO_3 chemical unit followed by the *removal* of a BO_2 chemical unit, the latter step forming a BO_2 vacancy complex. To decide whether this formation of vacancies is more or less favorable than the incorporation of excess AO chemical units into planar stacking faults of the type in RP phases, great care must be taken to

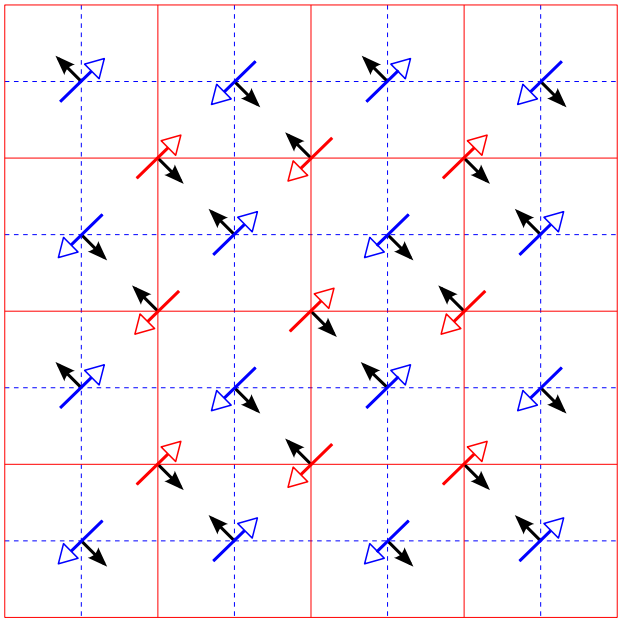

(a) High-energy configurations: $[0^-]$ or $[\pi^+]$

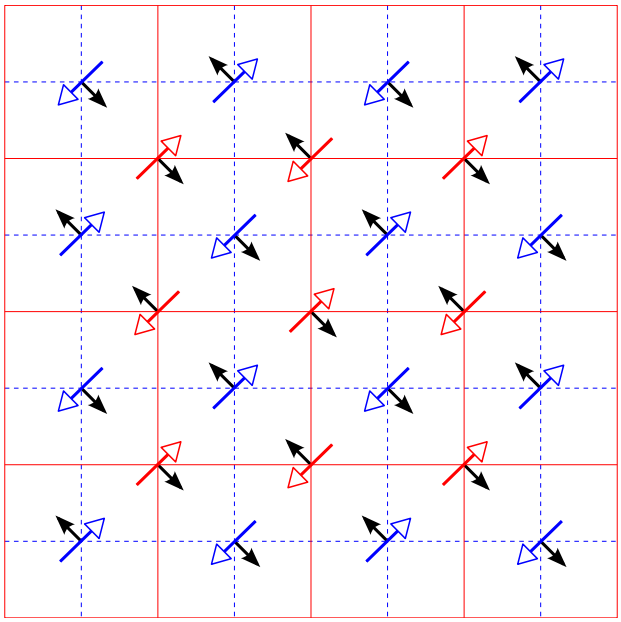

(b) Low-energy configurations: $[0^+]$ or $[\pi^-]$

Figure 4.12: Planar movement of oxygen ions on opposite sides of AO/AO stacking faults: rotation of octahedra in lower layer $\mathfrak{A}$ (↗↙, outlined arrowheads on solid grid) and upper layer $\mathfrak{B}$ (↗↙, outlined arrowheads on dashed grid) projected onto interfacial plane and resulting movement of oxygens (↖↘, filled arrowheads) within such plane. Panels depict (a) high-energy configuration with movement of neighboring oxygen atoms directly toward each other and (b) low-energy configuration with oxygen atoms moving past each other.

accurately balance stoichiometries.

In the current context, we have been considering the excess AO chemical units originating from an external reservoir of A-oxide. To maintain a consistent chemical potential, the formation energy of an isolated BO_2 vacancy in bulk perovskite must be computed as the energy first to remove an extra AO chemical unit from bulk A-oxide, and then to insert it into a large supercell containing n chemical units of ABO_3. Expressed mathematically, the energy of formation of this vacancy is

$$\begin{aligned} E_V &\equiv -E_{\mathrm{AO}} + E_{\mathrm{A}_{n+1}\mathrm{B}_n\mathrm{O}_{3n+1}} - E_{\mathrm{A}_n\mathrm{B}_n\mathrm{O}_{3n}} \\ &= -E_{\mathrm{AO}} + E_{\mathrm{A}_m\mathrm{B}_{m-1}\mathrm{O}_{3m-2}} - E_{\mathrm{A}_{m-1}\mathrm{B}_{m-1}\mathrm{O}_{3(m-1)}} \\ &= \quad E_{\mathrm{A}_m\mathrm{B}_{m-1}\mathrm{O}_{3m-2}} - \left[(m-1)E_{\mathrm{ABO}_3} + E_{\mathrm{AO}}\right], \end{aligned} \tag{4.6}$$

where $m \equiv n+1$. As the final equality in (4.6) indicates, the energy of formation of an isolated BO_2 vacancy in bulk perovskite is equivalent to the energy of a BO_2 vacancy in an initial bulk cell containing m chemical units of ABO_3 *relative* to the energy of $m-1$ chemical units of ABO_3 and one chemical unit of AO.

Figure 4.13 presents E_V computed as described above, for $m = \eta^3$ (corresponding to a series of supercells of size $\eta = 4, 6, \ldots, 14$ primitive unit cells on a side, with between 317 and 13 717 atoms each), plotted as a function of $1/\eta^2$. Following a least-squares fit, the unambiguous linear behavior in the plot indicates that the net interaction decays as $1/\eta^2$, with the ordinate intercept ($1/\eta^2 \to 0$, or $\eta \to \infty$) providing the extracted value of E_V for the incorporation of excess AO as *fully isolated* BO_2 vacancy complexes. The result within our model is $E_V = 3.61$ eV per excess AO unit, far exceeding the energy of formation for even the least favorable RP phase configuration (162 meV per excess AO chemical unit for $n \to \infty$ in the $[0^-]$ configuration). The positive sign and large magnitude of this energy indicate

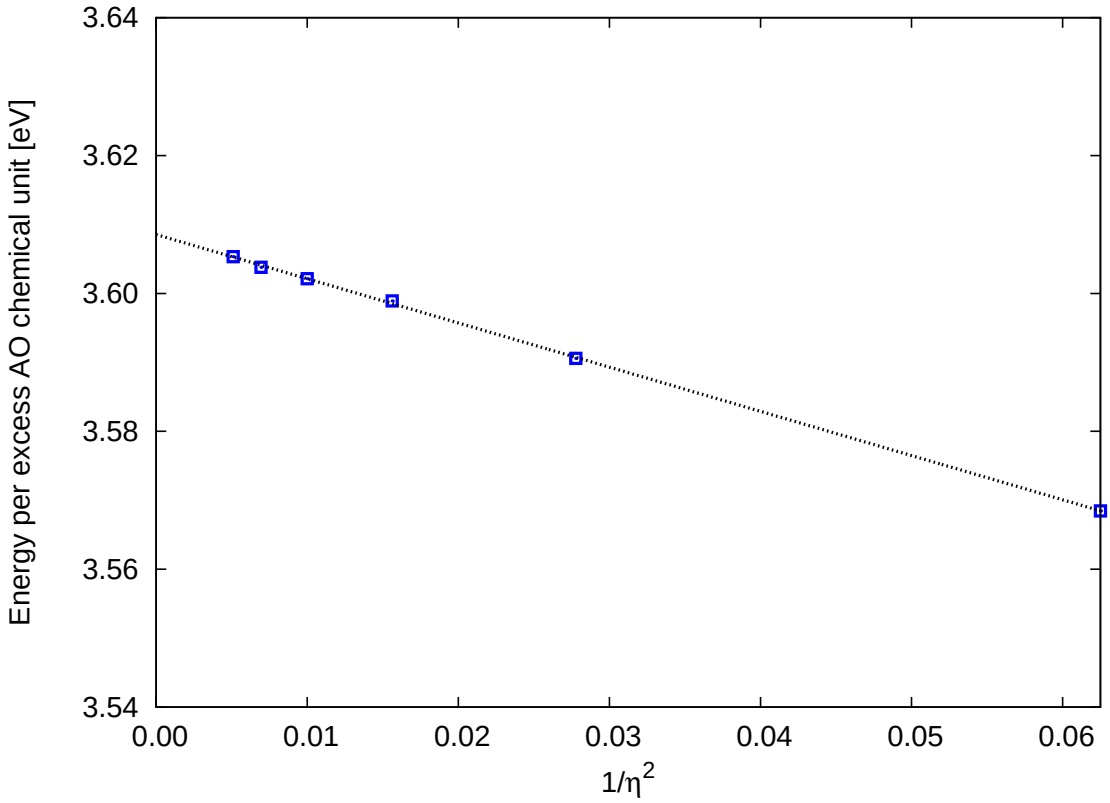

Figure 4.13: Formation energies of BO_2 vacancies as a function of inverse-square supercell dimension $1/\eta^2$: extraction of energies to infinite supercell (dotted line) to determine energy of isolated vacancy. (See text for definition of η.)

that A-rich ABO_3 will preferentially form planar AO stacking faults rather than isolated BO_2 vacancy complexes. This result supports the present work's focus on such stacking faults and RP phases.

4.6 Summary and conclusion

This work presents a detailed and exhaustive study of the zero-temperature structures of the homologous $A_{n+1}B_nO_{3n+1}$ series of Ruddlesden–Popper (RP) phases in a model antiferrodistortive perovskite for the greatest range of n considered to date. We also consider, for a specific Glazer system, *all possible* octahedral orientations within RP phases of the material. Our work introduces and follows a general program which may be replicated for RP phases of perovskites within any Glazer system and applied in both *ab initio* and empirical potential studies.

We begin our particular considerations with a careful enumeration and symmetry analysis for all thirty-two combinatorially possible configurations of octahedral rotations within RP phases of an $a^-a^-a^-$ Glazer system. Symmetry arguments reduce these thirty-two possibilities to five distinct configurations, which we denote as $[0^+]$, $[0^-]$, $[\frac{\pi}{2}^+]$, $[\pi^+]$, and $[\pi^-]$.

We then proceed to determine, within a shell-potential model, the ground-state structures of these five symmetry-distinct configurations for all values of $n = 1 \ldots 30$. We find that, for our specific model, only four configurations are actually distinct, as one of the configurations ($[\frac{\pi}{2}^+]$) is unstable to immediate relaxation to another configuration ($[\pi^-]$). After additional perturbation and quenching tests, we identify three of these remaining configurations as stable ($[\pi^-]$, $[0^+]$, $[\pi^+]$), and one as meta-stable ($[0^-]$). In agreement with experimental observation across a

range of perovskites, we find that, for all values of n, all of the configurations of RP phases provide a much more stable option for the incorporation of excess A-oxide than the formation of point defects, such as BO_2 vacancy complexes. We also find that, within our model, the two most stable configurations ($[\pi^-]$ and $[0^+]$) lead to stacking faults which are energetically preferred over phase separation into the bulk perovskite and bulk A-oxide. Both of these findings are consistent with the experimental observation of RP phases in a wide variety of antiferrodistortive perovskites, including titanates, ruthenates, manganites, and niobates.

In terms of the interactions between stacking faults, we find that the interaction varies inversely with the distance between excess AO planes, a result which we believe to be generic, at least for the $a^-a^-a^-$ system. For our particular model perovskite, the form of the interaction between stacking faults is attractive. In perovskites with such an attractive interaction, we find that ABO_3 with relatively low stoichiometric excess of species A manifests intergrowths between the $n = 2$ RP phase and bulk perovskite. When such intergrowths are observed experimentally, the interaction is likely attractive in correspondence with our model material.

Additionally, we observe that the five symmetry-distinct configurations have significant differences in energies of formation: $\sim$30 meV per rotational degree of freedom for our model perovskite, appreciably greater than the energy scales associated with orientational disorder in our model perovskite, 4–16 meV. This leads to an intriguing conjecture. For low densities of stacking faults within some perovskites, for a range of temperatures above their orientational phase transitions, the octahedra in bulk regions would exhibit randomized behavior about a high-symmetry mean configuration while octahedra near stacking faults would exhibit more ordered behavior about a lower-symmetry mean. Alternatively, for higher

densities of such faults, this increase in energy scale would correlate to an increase of the transition temperatures associated with octahedral rotations. These effects may be particularly noticeable in materials with higher orientational energy scales than our model perovskite, such as lanthanum aluminate with its transition temperature of 800 K.

Finally, we propose a simple physical mechanism to explain the strong dependence of the interfacial energy on the rotational state of the octahedra: some configurations result in movement of neighboring like-charged oxygen ions directly toward each other and thus are high in energy, whereas others result in movement of oxygen ions past each other and thus are low in energy.

BIBLIOGRAPHY

[1] John H. Barrett. Dielectric Constant in Perovskite Type Crystals. *Phys. Rev.*, 86(1):118–120, 1952. 100

[2] E. Hegenbarth. Die Feldstärkeabhängigkeit der Dielektrizitätskonstanten von $SrTiO_3$-Einkristallen im Temperaturbereich von 15 bis 80° K. *Phys. Status Solidi*, 6(2):333–337, 1964.

[3] G. A. Samara. Low-temperature dielectric properties of candidate substrates for high-temperature superconductors: $LaAlO_3$ and ZrO_2: 9.5 mol % Y_2O_3. *J. Appl. Phys.*, 68(8):4214–4219, 1990.

[4] Stephen A. Shevlin, Alessandro Curioni, and Wanda Andreoni. *Ab Initio* Design of High-k Dielectrics: $La_xY_{1-x}AlO_3$. *Phys. Rev. Lett.*, 94(14):146401, 2005. 100

[5] J. G. Bednorz and K. A. Müller. $Sr_{1-x}Ca_xTiO_3$: An XY Quantum Ferroelectric with Transition to Randomness. *Phys. Rev. Lett.*, 52(25):2289–2292, 1984. 100

[6] Ronald E. Cohen. Origin of ferroelectricity in perovskite oxides. *Nature*, 358 (6382):136–138, 1992.

[7] Gene H. Haertling. Ferroelectric Ceramics: History and Technology. *J. Am. Ceram. Soc.*, 82(4):797–818, 1999. 100

[8] N.-H. Chan, R. K. Sharma, and D. M. Smyth. Nonstoichiometry in $SrTiO_3$. *J. Electrochem. Soc.*, 128(8):1762–1769, 1981. 100

[9] N. G. Eror and U. Balachandran. High-Temperature Defect Structure of Acceptor-Doped Strontium Titanate. *J. Am. Ceram. Soc.*, 65(9):426–431, 1982.

[10] H. P. R. Frederikse, W. R. Thurber, and W. R. Hosler. Electronic Transport in Strontium Titanate. *Phys. Rev.*, 134(2A):A442–A445, 1964.

[11] Tetsurō Nakamura, Saburo Kose, and Toshiyuki Sata. Paramagnetism and Semiconductivity in a Triclinic Perovskite $BaBiO_3$. *J. Phys. Soc. Jpn.*, 31 (4):1284, 1971. 100

[12] J. F. Schooley, W. R. Hosler, and Marvin L. Cohen. Superconductivity in Semiconducting $SrTiO_3$. *Phys. Rev. Lett.*, 12(17):474–475, 1964. 100

[13] J. F. Schooley, W. R. Hosler, E. Ambler, J. H. Becker, Marvin L. Cohen, and C. S. Koonce. Dependence of the Superconducting Transition Temperature on Carrier Concentration in Semiconducting $SrTiO_3$. *Phys. Rev. Lett.*, 14 (9):305–307, 1965.

[14] C. S. Koonce, Marvin L. Cohen, J. F. Schooley, W. R. Hosler, and E. R. Pfeiffer. Superconducting Transition Temperatures of Semiconducting $SrTiO_3$. *Phys. Rev.*, 163(2):380–390, 1967. 100

[15] H. Arai, T. Yamada, K. Eguchi, and T. Seiyama. Catalytic Combustion of Methane Over Various Perovskite-Type Oxides. *Appl. Catal.*, 26(1–2): 265–276, 1986. 100

[16] Yasutake Teraoka, Hisashi Fukuda, and Shuichi Kagawa. Catalytic Activity of Perovskite-Type Oxides for the Direct Decomposition of Nitrogen Monoxide. *Chem. Lett.*, 19(1):1–4, 1990.

[17] M. A. Peña and J. L. G. Fierro. Chemical Structures and Performance of Perovskite Oxides. *Chem. Rev.*, 101(7):1981–2017, 2001. 100

[18] A. P. Ramirez. Colossal magnetoresistance. *J. Phys.: Condens. Matter*, 9 (39):8171–8199, 1997. 100

[19] Takeshi Obata, Takashi Manako, Yuichi Shimakawa, and Yoshimi Kubo. Tunneling magnetoresistance at up to 270 K in $La_{0.8}Sr_{0.2}MnO_3/SrTiO_3/La_{0.8}Sr_{0.2}MnO_3$ junctions with 1.6-nm-thick barriers. *Appl. Phys. Lett.*, 74(2):290–292, 1999. 100

[20] Jose Maria De Teresa, Agnès Barthélémy, Albert Fert, Jean Pierre Contour, François Montaigne, and Pierre Seneor. Role of Metal-Oxide Interface in Determining the Spin Polarization of Magnetic Tunnel Junctions. *Science*, 286(5439):507–509, 1999.

[21] M. Ziese. Extrinsic magnetotransport phenomena in ferromagnetic oxides. *Rep. Prog. Phys.*, 65(2):143–249, 2002. 100

[22] P. C. Joshi and S. B. Krupanidhi. Structural and electrical characteristics of $SrTiO_3$ thin films for dynamic random access memory applications. *J. Appl. Phys.*, 73(11):7627–7634, 1993. 100

[23] Cheol Seong Hwang, Soon Oh Park, Chang Seok Kang, Hag-Ju Cho, Ho-Kyu Kang, Sung Tae Ahn, and Moon Yong Lee. Deposition and Electrical Characterization of Very Thin $SrTiO_3$ Films for Ultra Large Scale Integrated Dynamic Random Access Memory Application. *Jpn. J. Appl. Phys.*, 34(9B): 5178–5183, 1995. 100

[24] Joseph V. Mantese, Norman W. Schubring, Adolph L. Micheli, and Anto-

nio B. Catalan. Ferroelectric thin films with polarization gradients normal to the growth surface. *Appl. Phys. Lett.*, 67(5):721–723, 1995. 100

[25] F. W. Van Keuls, R. R. Romanofsky, D. Y. Bohman, M. D. Winters, F. A. Miranda, C. H. Mueller, R. E. Treece, T. V. Rivkin, and D. Galt. ($YBa_2Cu_3O_{7-\delta}$,Au)/$SrTiO_3$/$LaAlO_3$ thin film conductor/ferroelectric coupled microstripline phase shifters for phased array applications. *Appl. Phys. Lett.*, 71(21):3075–3077, 1997. 100

[26] R. A. McKee, F. J. Walker, and M. F. Chisholm. Crystalline Oxides on Silicon: The First Five Monolayers. *Phys. Rev. Lett.*, 81(14):3014–3017, 1998. 100

[27] L. F. Edge, D. G. Schlom, S. A. Chambers, E. Cicerrella, J. L. Freeouf, B. Holländer, and J. Schubert. Measurement of the band offsets between amorphous $LaAlO_3$ and silicon. *Appl. Phys. Lett.*, 84(5):726–728, 2004. 100

[28] Shintaro Yamamichi, Hisato Yabuta, Toshiyuki Sakuma, and Yoichi Miyasaka. (Ba+Sr)/Ti ratio dependence of the dielectric properties for $(Ba_{0.5}Sr_{0.5})TiO_3$ thin films prepared by ion beam sputtering. *Appl. Phys. Lett.*, 64(13):1644–1646, 1994. 100

[29] T. R. Taylor, P. J. Hansen, N. Pervez, B. Acikel, R. A. York, and J. S. Speck. Influence of stoichiometry on the dielectric properties of sputtered strontium titanate thin films. *J. Appl. Phys.*, 94(5):3390–3396, 2003. 100, 101

[30] U. Balachandran and N. G. Eror. On the defect structure of strontium titanate with excess SrO. *J. Mater. Sci.*, 17(7):2133–2140, 1982. 100, 148

[31] D. M. Smyth. Defects and Order in Perovskite-Related Oxides. *Annu. Rev. Mater. Sci.*, 15(1):329–357, 1985.

[32] S. Witek, D. M. Smyth, and H. Pickup. Variability of the Sr/Ti Ratio in $SrTiO_3$. *J. Am. Ceram. Soc.*, 67(5):372–375, 1984. 100

[33] S. N. Ruddlesden and P. Popper. New compounds of the K_2NiF_4 type. *Acta Crystallogr.*, 10(8):538–539, 1957. 100

[34] S. N. Ruddlesden and P. Popper. The compound $Sr_3Ti_2O_7$ and its structure. *Acta Crystallogr.*, 11(1):54–55, 1958. 100

[35] W. Kwestroo and H. A. M. Paping. The Systems BaO–SrO–TiO_2, BaO–CaO–TiO_2, and SrO–CaO–TiO_2. *J. Am. Ceram. Soc.*, 42(6):292–299, 1959. 101

[36] J. H. Haeni, C. D. Theis, D. G. Schlom, W. Tian, X. Q. Pan, H. Chang, I. Takeuchi, and X.-D. Xiang. Epitaxial growth of the first five members of the $Sr_{n+1}Ti_nO_{3n+1}$ Ruddlesden–Popper homologous series. *Appl. Phys. Lett.*, 78(21):3292–3294, 2001. 101

[37] Kyu Hyoung Lee, Yi Feng Wang, Sung Wng Kim, Hiromichi Ohta, and Kunihito Koumoto. Thermoelectric Properties of Ruddlesden–Popper Phase n-Type Semiconducting Oxides: La-, Nd-, and Nb-Doped $Sr_3Ti_2O_7$. *Int. J. Appl. Ceram. Technol.*, 4(4):326–331, 2007. 101

[38] Zhenhua Liang, Kaibin Tang, Qian Shao, Guocan Li, Suyuan Zeng, and Huagui Zheng. Synthesis, crystal structure, and photocatalytic activity of a new two-layer Ruddlesden–Popper phase, $Li_2CaTa_2O_7$. *J. Solid State Chem.*, 181(4):964–970, 2008. 101

[39] Y. Maeno, H. Hashimoto, K. Yoshida, S. Nishizaki, T. Fujita, J. G. Bednorz, and F. Lichtenberg. Superconductivity in a layered perovskite without copper. *Nature*, 372(6506):532–534, 1994. 101

[40] S. A. Grigera, R. S. Perry, A. J. Schofield, M. Chiao, S. R. Julian, G. G. Lonzarich, S. I. Ikeda, Y. Maeno, A. J. Millis, and A. P. Mackenzie. Magnetic Field-Tuned Quantum Criticality in the Metallic Ruthenate $Sr_3Ru_2O_7$. *Science*, 294(5541):329–332, 2001. 101

[41] R. S. Perry, L. M. Galvin, S. A. Grigera, L. Capogna, A. J. Schofield, A. P. Mackenzie, M. Chiao, S. R. Julian, S. I. Ikeda, S. Nakatsuji, Y. Maeno, and C. Pfleiderer. Metamagnetism and Critical Fluctuations in High Quality Single Crystals of the Bilayer Ruthenate $Sr_3Ru_2O_7$. *Phys. Rev. Lett.*, 86(12): 2661–2664, 2001. 101

[42] G. Cao, S. K. McCall, J. E. Crow, and R. P. Guertin. Ferromagnetism in $Sr_4Ru_3O_10$: Relationship to other layered metallic oxides. *Phys. Rev. B*, 56 (10):R5740–R5743, 1997. 101

[43] Y. Moritomo, A. Asamitsu, H. Kuwahara, and Y. Tokura. Giant magnetoresistance of manganese oxides with a layered perovskite structure. *Nature*, 380(6570):141–144, 1996. 101

[44] D. C. Meyer, A. A. Levin, T. Leisegang, E. Gutmann, P. Paufler, M. Reibold, and W. Pompe. Reversible tuning of a series of intergrowth phases of the Ruddlesden–Popper type $SrO(SrTiO_3)_n$ in an (001) $SrTiO_3$ single-crystalline plate by an external electric field and its potential use for adaptive X-ray optics. *Appl. Phys. A*, 84(1–2):31–35, 2006. 101

[45] D. G. Schlom, J. N. Eckstein, I. Bozovic, Z. J. Chen, A. F. Marshall, K. E. von Dessonneck, and J. S. Harris, Jr. Molecular beam epitaxy—a path to novel high T_c superconductors? In Anupam Madhukar, editor, *Growth of Semiconductor Structures and High-T_c Thin Films on Semiconductors*, volume 1285, pages 234–247. SPIE, 1990. 101

[46] M. E. Klausmeier-Brown, G. F. Virshup, I. Bozovic, J. N. Eckstein, and K. S. Ralls. Engineering of ultrathin barriers in high T_C, trilayer Josephson junctions. *Appl. Phys. Lett.*, 60(22):2806–2808, 1992.

[47] O. Peña, F. LeBerre, M. Sergent, R. Horyń, and A. Wojakowski. Superconductivity and magnetism in Chevrel-phase rare-earth molybdenum selenides single crystals $REMo_6Se_8$ (RE=Gd, Dy). *Physica C*, 235–240(2):771–772, 1994.

[48] S. D. Bader, R. M. Osgood III, D. J. Miller, J. F. Mitchell, and J. S. Jiang. Role of intergrowths in the properties of naturally layered manganite single crystals (invited). *J. Appl. Phys.*, 83(11):6385–6389, 1998. 101

[49] R. J. D. Tilley. An Electron Microscope Study of Perovskite-Related Oxides in the Sr–Ti–O System. *J. Solid State Chem.*, 21(4):293–301, 1977. 101, 114, 124, 142

[50] R. Ramesh, S. Jin, and P. Marsh. Superconductor defect structure. *Nature*, 346(6283):420, 1990.

[51] A. Schilling, M. Cantoni, J. D. Guo, and H. R. Ott. Superconductivity above 130 K in the Hg–Ba–Ca–Cu–O system. *Nature*, 363(6424):56–58, 1993. 101

[52] Gregory J. McCarthy, William B. White, and Rustum Roy. Phase Equilibria in the 1375°C Isotherm of the System Sr–Ti–O. *J. Am. Ceram. Soc.*, 52(9): 463–467, 1969. 101, 114, 124

[53] Yoshiki Iwazaki, Toshimasa Suzuki, Shoichi Sekiguchi, and Masayuki Fujimoto. Artificial $SrTiO_3$/SrO Superlattices by Pulsed Laser Deposition. *Jpn. J. Appl. Phys.*, 38(12A):L1443–L1446, 1999. 101

[54] Yoshiki Iwazaki, Toshimasa Suzuki, Shoichi Sekiguchi, and Masayuki Fujimoto. Thermal Stability of Artificial $SrTiO_3$/SrO Superlattice Epitaxially Grown on $SrTiO_3$ Single Crystal. *Jpn. J. Appl. Phys.*, 39(4A):L303–L305, 2000.

[55] Keisuke Shibuya, Shaobo Mi, Chun-Lin Jia, Paul Meuffels, and Regina Dittmann. Sr_2TiO_4 layered perovskite thin films grown by pulsed laser deposition. *Appl. Phys. Lett.*, 92(24):241918, 2008. 101

[56] Hidekazu Tanaka and Tomoji Kawai. Artificial construction of SrO/(La,Sr)MnO_3 layered perovskite superlattice by laser molecular-beam epitaxy. *Appl. Phys. Lett.*, 76(24):3618–3620, 2000. 101

[57] W. Tian, X. Q. Pan, J. H. Haeni, and D. G. Schlom. Transmission electron microscopy study of $n = 1$–5 $Sr_{n+1}Ti_nO_{3n+1}$ epitaxial thin films. *J. Mater. Res.*, 16(7):2013–2026, 2001. 101

[58] P. Fisher, S. Wang, M. Skowronski, P. A. Salvador, M. Snyder, and O. Maksimov. A series of layered intergrowth phases grown by molecular beam epitaxy: Sr_mTiO_{2+m} ($m = 1$–5). *Appl. Phys. Lett.*, 91(25):252901, 2007. 101

[59] Toshimasa Suzuki, Yuji Nishi, and Masayuki Fujimoto. Defect structure in homoepitaxial non-stoichiometric strontium titanate thin films. *Philos. Mag. A*, 80(3):621–637, 2000. 101

[60] K. R. Udayakumar and Alastair N. Cormack. Structural Aspects of Phase Equilibria in the Strontium–Titanium–Oxygen System. *J. Am. Ceram. Soc.*, 71(11):C469–C471, 1988. 103

[61] Michael A. McCoy, Robin W. Grimes, and William E. Lee. Phase stability

and interfacial structures in the SrO–$SrTiO_3$ system. *Philos. Mag. A*, 75(3): 833–846, 1997. 103

[62] Craig J. Fennie and Karin M. Rabe. Structural and dielectric properties of Sr_2TiO_4 from first principles. *Phys. Rev. B*, 68(18):184111, 2003. 103

[63] Toshimasa Suzuki and Masayuki Fujimoto. First-principles structural stability study of nonstoichiometry-related planar defects in $SrTiO_3$ and $BaTiO_3$. *J. Appl. Phys.*, 89(10):5622–5629, 2001.

[64] O. Le Bacq, E. Salinas, A. Pisch, C. Bernard, and A. Pasturel. First-principles structural stability in the strontium–titanium–oxygen system. *Philos. Mag.*, 86(15):2283–2292, 2006.

[65] Claudine Noguera. Theoretical investigation of the Ruddlesden–Popper compounds $Sr_{n+1}Ti_nO_{3n+1}$ ($n = 1$–3). *Philos. Mag. Lett.*, 80(3):173–180, 2000.

[66] Hongming Weng, Y. Kawazoe, Xiangang Wan, and Jinming Dong. Electronic structure and optical properties of layered perovskites Sr_2MO_4 (M=Ti, V, Cr, and Mn): An *ab initio* study. *Phys. Rev. B*, 74(20):205112, 2006. 103

[67] Ali Hussain Reshak, Sushil Auluck, and Ivan Kityk. Electronic Band Structure and Optical Properties of $Sr_{n+1}Ti_nO_{3n+1}$ Ruddlesden–Popper Homologous Series. *Jpn. J. Appl. Phys.*, 47(7):5516–5520, 2008.

[68] Denis Music and Jochen M. Schneider. Elastic properties of $Sr_{n+1}Ti_nO_{3n+1}$ phases ($n = 1$–3, ∞). *J. Phys.: Condens. Matter*, 20(5):055224, 2008. 103

[69] M. M. Elcombe, E. H. Kisi, K. D. Hawkins, T. J. White, P. Goodman, and S. Matheson. Structure Determinations for $Ca_3Ti_2O_7$, $Ca_4Ti_3O_{10}$, $Ca_{3.6}Sr_{0.4}Ti_3O_{10}$ and a Refinement of $Sr_3Ti_2O_7$. *Acta Crystallogr.*, B47(3): 305–314, 1991. 104

[70] K. S. Aleksandrov and J. Bartolome. Octahedral tilt phases in perovskite-like crystals with slabs containing an even number of octahedral layers. *J. Phys.: Condens. Matter*, 6(40):8219–8235, 1994. 104

[71] Dorian M. Hatch, Harold T. Stokes, K. S. Aleksandrov, and S. V. Misyul. Phase transitions in the perovskitelike A_2BX_4 structure. *Phys. Rev. B*, 39 (13):9282–9288, 1989. 104, 105, 123

[72] A. M. Glazer. The Classification of Tilted Octahedra in Perovskites. *Acta Crystallogr.*, B28(11):3384–3392, 1972. 104, 106, 107, 108

[73] S. Geller and V. B. Bala. Crystallographic Studies of Perovskite-like Compounds. II. Rare Earth Aluminates. *Acta Crystallogr.*, 9(12):1019–1025, 1956. 106

[74] R. T. Harley, W. Hayes, A. M. Perry, and S. R. P. Smith. The phase transitions of $PrAlO_3$. *J. Phys. C*, 6(14):2382–2400, 1973. 106

[75] Jean-Michel Moreau, Christian Michel, R. Gerson, and W. J. James. Atomic Displacement Relationship to Rhombohedral Deformation in Some Perovskite-Type Compounds. *Acta Crystallogr.*, B26(10):1425–1428, 1970. 106

[76] A. M. Glazer. Simple Ways of Determining Perovskite Structures. *Acta Crystallogr.*, A31(6):756–762, 1975. 106, 107

[77] Helen D. Megaw and C. N. W. Darlington. Geometrical and Structural Relations in the Rhombohedral Perovskites. *Acta Crystallogr.*, A31(2):161–173, 1975. 106

[78] Hiromi Unoki and Tunetaro Sakudo. Electron Spin Resonance of Fe^{3+} in $SrTiO_3$ with Special Reference to the 110°K Phase Transition. *J. Phys. Soc. Jpn.*, 23(3):546–552, 1967. 107, 108

[79] P. A. Fleury, J. F. Scott, and J. M. Worlock. Soft Phonon Modes and the 110° K Phase Transition in $SrTiO_3$. *Phys. Rev. Lett.*, 21(1):16–19, 1968.

[80] G. Shirane and Y. Yamada. Lattice-Dynamical Study of the 110°K Phase Transition in $SrTiO_3$. *Phys. Rev.*, 177(2):858–863, 1969. 107

[81] E. Pytte and J. Feder. Theory of a Structural Phase Transition in Perovskite-Type Crystals. *Phys. Rev.*, 187(3):1077–1088, 1969. 107

[82] J. Feder and E. Pytte. Theory of a Structural Phase Transition in Perovskite-Type Crystals. II. Interaction with Elastic Strain. *Phys. Rev. B*, 1(12):4803–4810, 1970. 107

[83] J. F. Scott. Soft-mode spectroscopy: Experimental studies of structural phase transitions. *Rev. Mod. Phys.*, 46(1):83–128, 1974. 107

[84] W. Cochran. Crystal Stability and the Theory of Ferroelectricity Part II. Piezoelectric Crystals. *Adv. Phys.*, 10(40):401–420, 1961. 107

[85] K. A. Müller, W. Berlinger, and F. Waldner. Characteristic Structural Phase Transition in Perovskite-Type Compounds. *Phys. Rev. Lett.*, 21(12):814–817, 1968. 107, 108, 109

[86] J. D. Axe, G. Shirane, and K. A. Müller. Zone-Boundary Phonon Instability in Cubic $LaAlO_3$. *Phys. Rev.*, 183(3):820–823, 1969. 107

[87] H. Thomas and K. A. Müller. Structural Phase Transitions in Perovskite-Type Crystals. *Phys. Rev. Lett.*, 21(17):1256–1259, 1968. 107

[88] JeeHye Lee. private communication, 2008. 108

[89] Farrel W. Lytle. X-Ray Diffractometric Examination of Low-Temperature Phase Transformations in Single-Crystal Strontium Titanate. In William M.

Mueller, Gavin Mallett, and Marie Fay, editors, *Advances in X-Ray Analysis*, volume 7, pages 136–145. Plenum Press, 1964. 108

[90] Farrel W. Lytle. X-Ray Diffractometry of Low-Temperature Phase Transformations in Strontium Titanate. *J. Appl. Phys.*, 35(7):2212–2215, 1964. 108

[91] Berthold Alefeld. Die Messung der Gitterparameteränderung von Strontiumtitanat am Phasenübergang bei 108 °K. *Z. Phys.*, 222(2):155–164, 1969. 108

[92] Th. von Waldkirch, K. A. Müller, and W. Berlinger. Fluctuations in $SrTi_3$ near the 105-K Phase Transition. *Phys. Rev. B*, 7(3):1052–1066, 1973. 108, 138

[93] J. F. Scott. Raman study of Trigonal-Cubic Phase Transitions in Rare-Earth Aluminates. *Phys. Rev.*, 183(3):823–825, 1969. 109

[94] J. F. Scott. *Errata*: Raman study of Trigonal-Cubic Phase Transitions in Rare-Earth Aluminates. *Phys. Rev. B*, 1(2):942, 1970. 109

[95] Christopher J. Howard, Brendan J. Kennedy, and Bryan C. Chakoumakos. Neutron powder diffraction study of rhombohedral rare-earth aluminates and the rhombohedral to cubic phase transition. *J. Phys.: Condens. Matter*, 12 (4):349–365, 2000. 109

[96] V. M. Goldschmidt. Untersuchungen Über bau und Eigenschaften von Krystallen. *Skrifter Norske Videnskaps-Akad. i Oslo, I. Mat. Natur. Kl.*, 8:1–156, 1926. 109

[97] Francis S. Galasso. *Structure, Properties and Preparation of Perovskite-Type Compounds*, pages 3–11. Pergamon Press, Oxford, UK, 1969. 109

[98] R. D. Shannon. Revised Effective Ionic Radii and Systematic Studies of Interatomic Distances in Halides and Chalcogenides. *Acta Crystallogr.*, A32 (5):751–767, 1976. 109

[99] G. J. McCarthy, W. B. White, and R. Roy. The System Eu–Ti–O: Phase Relations in a Portion of the 1400°C Isotherm. *J. Inorg. Nucl. Chem.*, 31(2): 329–339, 1969. 114, 124

[100] B. G. Dick, Jr. and A. W. Overhauser. Theory of the Dielectric Constants of Alkali Halide Crystals. *Phys. Rev.*, 112(1):90–103, 1958. 125

[101] M. Javed Akhtar, Zeb-Un-Nisa Akhtar, Robert A. Jackson, and C. Richard A. Catlow. Computer Simulation Studies of Strontium Titanate. *J. Am. Ceram. Soc.*, 78(2):421–428, 1995. 125, 126, 127, 128, 129, 132, 138

[102] R. A. Buckingham. The Repulsive Interaction of Atoms in S States. *Trans. Faraday Soc.*, 54(4):453–459, 1958. 126

[103] Max Born and Joseph E. Mayer. Zur Gittertheorie der Ionenkristalle. *Z. Phys.*, 75(1–2):1–18, 1932. 126

[104] J. E. Lennard-Jones. Cohesion. *Proc. Phys. Soc.*, 43(5):461–482, 1931. 126

[105] Johannes Diderik van der Waals. *Over de Continuiteit van den Gas- en Vloeistoftoestand*. PhD thesis, University of Leiden, 1873. 126

[106] G. V. Lewis and C. R. A. Catlow. Potential models for ionic oxides. *J. Phys. C*, 18(6):1149–1161, 1985. 126, 132

[107] C. R. A. Catlow and A. M. Stoneham. Ionicity in solids. *J. Phys. C*, 16(22): 4321–4338, 1983. 126, 132

[108] P. P. Ewald. Die Berechnung optischer und elektrostatischer Gitterpotentiale. *Ann. Phys.*, 369(3):253–287, 1921. 129

[109] Tom Darden, Darrin York, and Lee Pedersen. Particle mesh Ewald: An $N \cdot \log(N)$ method for Ewald sums in large systems. *J. Chem. Phys.*, 98 (12):10089–10092, 1993. 129

[110] Ulrich Essmann, Lalith Perera, Max. L Berkowitz, Tom Darden, Hsing Lee, and Lee G. Pedersen. A smooth particle mesh Ewald method. *J. Chem. Phys.*, 103(19):8577–8593, 1995.

[111] Markus Deserno and Christian Holm. How to mesh up Ewald sums. I. A theoretical and numerical comparison of various particle mesh routines. *J. Chem. Phys.*, 109(18):7678–7693, 1998. 129

[112] Magnus R. Hestenes and Eduard Stiefel. Methods of Conjugate Gradients for Solving Linear Systems. *J. Res. Natl. Bur. Stand.*, 49(6):409–436, 1952. 130

[113] E. Polak and G. Ribière. Note sur la Convergence de Méthodes de Directions Conjuguées. *Rev. Fr. Inform. Rech. O.*, 3(16):35–43, 1969. 130